Development of a Novel Boron Free Filler Metal for Transient Liquid Phase Bonding of Ni base superalloys

by

Margaret Clare MacIsaac

Submitted in partial fulfillment of the requirements
for the degree of Master of Applied Science

at

Dalhousie University
Halifax, Nova Scotia
December 2019

Dedication

I wish to dedicate this work and degree to my parents, Donnie and Lucia MacIsaac, for their unwavering support and introduction to engineering. You have instilled in me the importance of education and dedication to your work which carried me through this journey. Thanks to my siblings Donald, Maureen, and Neil for their love and encouragement always.

Thank you and enjoy the read.

Table of Contents

List of Figures

List of Tables

Abstract

Joining of Ni base superalloys by transient liquid phase bonding (TLPB) has found limited application in aerospace due to the formation of brittle borides adjacent to the joint. Filler metals containing ~3 wt% B as a melting point depressant (MPD) are the industry standard due to fast isothermal solidification (IS) kinetics, low brazing temperature (1050 °C) and relatively low cost. In the current work, a boron-free filler metal using Cu and Mn as an alternative MPD is proposed as a novel filler metal (FM) for IN625 base metal (BM). A commercially available FM powder, NiCuMn37 was combined with pure Ni powder to create the novel Ni30 alloy, containing 30 wt% Ni. The Ni30 FM and prepared joints were analysed by in-situ thermal analysis using a differential scanning calorimeter (DSC). Using DSC analysis, the liquid fraction present in the joint was tracked and isothermal solidification (IS) kinetics was quantified against hold time at 1050 °C. Elemental analysis of Ni30/IN625 joints coupled with calculations of melting range using Thermo-Calc software confirmed the progress of IS at relevant hold times.

Resulting braze joints had a solid solution microstructure with a diffusionally affected zone (DAZ) in the BM. IS of a ~110 µm braze joint completed after 80 minutes, and a ~380 µm braze joint completed IS after 1320 minutes. The kinetics of the Ni30/IN625 system was determined to be like that of boron containing FM BNi-2. Experimental diffusivity calculations determined that the IS kinetics are governed by the slower diffusing element Cu into IN625. An investigation of mechanical properties using single lap shear testing samples showed that Ni30/IN625 joints failed in the DAZ, and BNi-2/IN625 joints failed in the BM precipitated by brittle borides. Strength at failure showed that both joints had decreased strength compared to wrought IN625, but Ni30 joints had higher strength than BNi-2 joints.

The comparable IS kinetics and increased strength of Ni30 are a promising combination indicating high potential for the novel Ni30 FM to replace boron containing FM alloys.

List of Abbreviations and Symbols Used

A	overlap distance of single lap joint specimens (mm)
ASZ	Athermally solidified zone
AWS	American Welding Society
BM	Base metal
BTF	buy-to-fly
CALPHAD	Calculation of phase diagram
CES	Cambridge Engineering Selector
C_0	initial solute concentration in filler metal
C_m	solute composition in base metal
C_s	solute concentration of solid phase
D	Diffusion coefficient
d_{50}	median diameter of particle (μm)
$\widetilde{D_{ex}}_{Cu\ Mn}^{Ni}$	experimental interdiffusion coefficient of Ni, Cu, Mn
$\widetilde{D}_{Cu\ Mn}^{Ni}$	theoretical interdiffusion coefficient of Ni, Cu, and Mn
DAZ	Diffusionally affected zone
DICTRA	Diffusion Controlled Transformation
DS	Diffusional solidification
DSC	Differential scanning calorimetry
EDM	Electrical discharge machining
EDS	Energy dispersive spectroscopy
FBJ	Full braze joint
FCC	Face centred cubic
FEA	finite element analysis
FM	Filler metal
fps	frames per second
GE	General Electric
ΔH_t	enthalpy of melting at time, t
ΔH_0	enthalpy of complete FM melting without BM interaction
HBJ	Half braze joint

HT	High temperature remelt (1200 °C) thermal profile
IN625	Inconel 625
IS	Isothermal solidification
ISZ	Isothermally solidified zone
k	slope of MBC plot also rate of isothermal solidification (μm $min^{-1/2}$)
kpm	kelvin per minute, equivalent to °C per minute
ΔL	displacement measured by extensometer (mm)
L_f	Liquid fraction
LT	low temperature remelt (1050 °C) thermal profile
M region	Primary matrix of Ni30 braze joints
MA	Master alloy
MBC	Maximum brazing clearance
MD	Matrix of diffusionally affected zone
MPD	Melting point depressant
γ-Ni	Primary gamma phase in nickel
NNS	Near net shape
OTS ®	Oxygen trap system
P	load (N)
ppt	Precipitate phase
S region	Segregated region of matrix in Ni30 braze joint
S/L	Solid liquid interface
SEM	Scanning electron microscope
T	plate thickness (mm)
T_B	brazing temperature (1050 °C)
T_H	high temperature remelt temperature (1200 °C)
T_{liq}	liquidus temperature
T_R	remelt temperature (900 °C)
T_{sol}	solidus temperature
t_f	time of full isothermal solidification (min)
TCNi	Thermo-Calc software Ni database
TLPB	Transient liquid phase bonding

UTC	United Technologies Corporation
wt%	weight percent
w	width of the brazed region in a half braze joint
2w	width of the brazed region in a full braze joint
w_0	measured width of the braze region in a half braze joint
w_i	width of braze region in HBJ determined by linear regression at t=0
$2w_{isz}$	width of ISZ in a full braze joint, equal to MBC_t at t
X_A	molar fraction of element A in alloy
φ	bending angle (°)
σ	stress (MPa)
τ	shear stress (MPa)
ε	strain (mm/mm)

Acknowledgements

First of all, I would first like to thank my supervisor Dr. Stephen Corbin for his support and guidance throughout my undergraduate and graduate work. His curiosity and passion for metallurgy has kept me motivated to learn and increased my own love for materials and experimentation. Thanks also to my supervisory committee members Dr. Paul Bishop, and Dr. Suzanne Budge.

I would like to acknowledge the financial support of National Science and Engineering Research Council of Canada (NSERC) and Pratt and Whitney Canada as contributors to Industrial Research Chair in Structural Brazing and Processing of Powder Metallurgy Superalloys.

Special acknowledgement and much thanks to Cathy Whitman and Liv MacLellan for their important help and expertise with preliminary characterisation of alloy mixtures.

I would like to thank Randy Cooke and Patricia Scallion for lending technical expertise to this work. Final thanks to the lovely members of the High Temperature Thermal Analysis Lab group for their daily support and conversations: Joel Chapman, Addison Rayner, Julian O'Flynn, Colin Tadgell, Eric Moreau, Dan Cluff, and co-op student Hannah Kauffman.

Chapter 1 Introduction

1.1 Aircraft Engines

As air travel has become more accessible, its environmental impact has become more evident. A focus on environmental sustainability has sparked technological advancements in many sectors of aircraft engine manufacturing and design. A notable contribution is the development of gas turbine engines. Gas turbine engines claim to reduce fuel consumption by 16%, and particulate emissions by 50% when compared to turboprop engines [1]. This significant decrease in fuel consumption and redesign of the aircraft's engine has increased both temperature and pressure operating conditions in the engine which require heat resistant materials able to retain strength during extensive operations at elevated temperatures. As shown in Figure 1.1, the turbine (hot) section of the Trent 800 engine (produced by Rolls Royce) is composed exclusively of nickel-base superalloys.

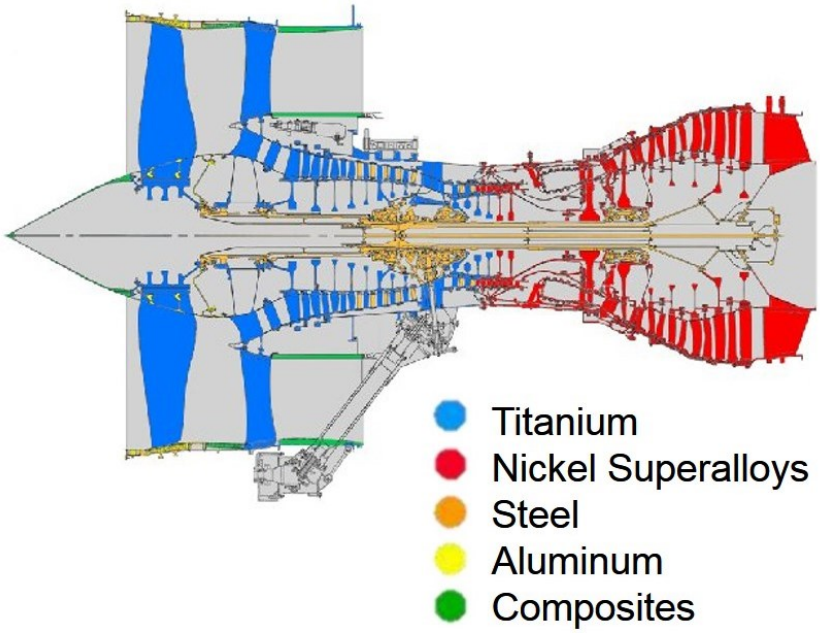

Figure 1.1 – Schematic of Rolls Royce Trent 800 engine. [2]

1.2 Nickel-base Superalloys

Nickel is used as an alloying element in stainless steels to increase the corrosion resistance and operating temperature of the alloy. The development of superalloys followed the need for a stainless steel alloy with increased strength and high temperature capabilities. Iron-nickel alloys were developed with increasing amounts of nickel to fill this need in the 1940s. As the gas turbine engine was developed, superalloys diversified to include nickel-iron, nickel, and cobalt-base alloys with an extensive amount of further alloying elements [3]. The aerospace industry and industrial gas turbines continue to be the main application for superalloys. Other common applications of nickel base superalloys are: chemical plant, and petrochemical plant equipment, steam turbine power plants, rocket engine parts for space vehicles, nuclear power systems, and metal processing hot work tools, and casting dies [3].

From a strength, high temperature, oxidation and corrosion resistance perspective no other metal alloy system can perform like nickel-base superalloys. Specifically comparing the maximum service temperature of alloys, as in Figure 1.2, it is clear that nickel is the superior metal alloy system.

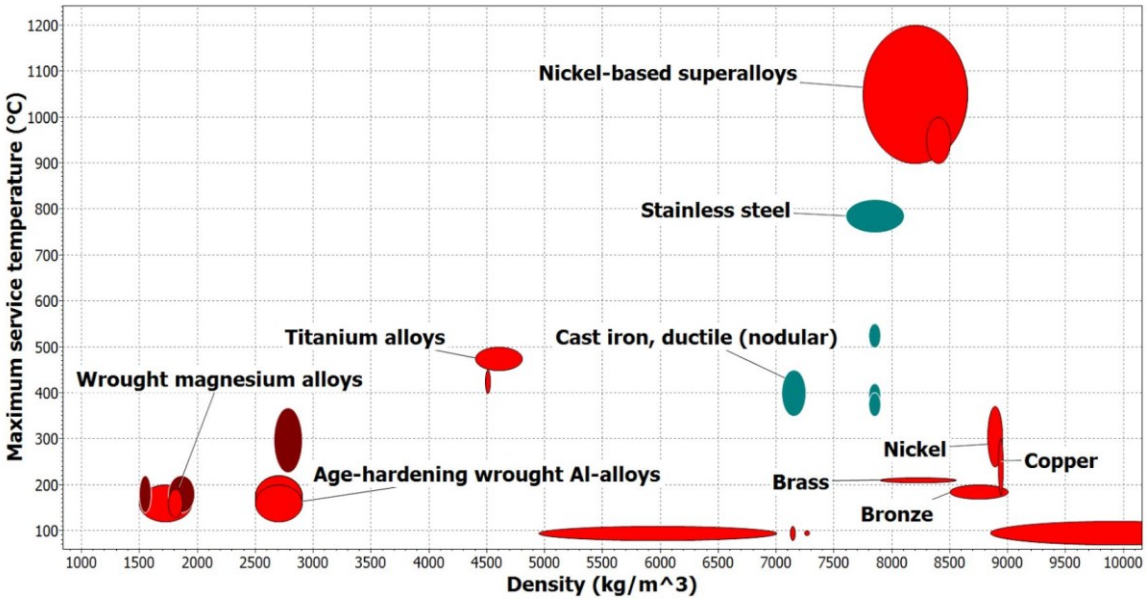

Figure 1.2 – Maximum service temperature vs density of common metallic alloys (produced using CES Edupack [4])

It is important to note that nickel base superalloys have a high density, slightly higher than stainless steels. This is a drawback to using nickel base superalloys in aircraft as heavier materials increase the fuel consumption of the aircraft. Despite this, nickel and cobalt base superalloys dominate the market of high temperature materials.

1.2.1 Inconel 625 (IN625)

The focus of this work is bonding of nickel-base superalloy Inconel 625 (IN625), composition detailed in Table 1.1. As a modern nickel base alloy, the primary matrix is a continuous FCC phase (γNi-phase) which is stable at all temperatures. IN625 is a solid solution alloy primarily strengthened with the addition of chromium (Cr), molybdenum (Mo), and niobium (Nb) [5]. In addition to the elements listed in Table 1.1, IN625 contains ~0.05 wt% carbon. The most common carbides formed in superalloys are MC, $M_{23}C_6$, and M_6C, where M is titanium/niobium, chromium/iron, and molybdenum respectively. The brittle carbides generally grow along grain boundaries and can become

detrimental to high temperature properties of the alloy. A discontinuous chain of carbides along the grain boundaries which has been shown to be the optimal case [5].

Table 1.1 – Nominal elemental composition of IN625 nickel-base superalloy [3]

	Ni	Cr	Mo	Nb	Fe	Al	Ti
IN625	61.0	21.5	9.0	3.6	2.5	0.2	0.2

The addition of Nb to nickel-base superalloys allows for weldability of the alloy. Generally, when heated to high temperatures needed for welding, chromium carbides ($M_{23}C_6$) will precipitate at the grain boundaries which makes the alloy susceptible to intergranular corrosion. Nb-carbides (MC) precipitate both throughout the grain and at the grain boundaries which allows for a discontinuous chain of carbides which will not cause intergranular corrosion or cracking [3].With Nb added to the alloy, Nb-carbides (MC) will precipitate before Cr-carbides allowing welding of the alloy [5].

1.3 Inefficiencies in Manufacturing Processes

The manufacturing process for all aircraft parts is described in industry by the buy-to-fly (BTF) ratio. This is a mass based ratio of material purchased to material used in the final aircraft, hence buy to fly. Many engine components are machined to very specific dimensions from a forged billet. Forging to a shape similar to the final component geometry is generally not possible or expensive due to high machinery and energy costs. High precision machining a complex shape causes a significant amount of material waste. A BTF of 5 is typical and 10-20 has been reported when manufacturing certain engine components [6], which amounts to 80-95 wt% of the original billet wasted.

To reduce this waste during the manufacturing process, many of the world leading aviation companies (UTC, GE) are looking towards near net shape manufacturing. Near

net shape (NNS) manufacturing is a broad term which describes different technologies including additive manufacturing (deposition by laser, and electron beam) and powder metallurgy. Additive manufacturing is an emerging and promising field. Unfortunately, it currently is significantly more expensive to implement in both time and manufacturing cost. An alternative NNS solution is to produce several small components which can then be joined together to create the final component. This process is used in many industries to create complex shapes [6].

Ni base superalloys can be joined by solid state welding, fusion welding, and brazing [7], [3]. The feasibility of each of these joining methods depends on the alloy class. Solid solution Ni-base alloys can generally be welded without issue, though in repair and high precision applications, brazing is a more suitable joining method. Brazing of Ni base superalloys, and the current limitations will be discussed in the following sections.

1.4 Brazing of Ni base Superalloys

Ni base superalloys are widely joined by brazing for many moderate and high temperature applications where welding is not possible. Producing a high quality joint capable of withstanding the service requirements of Ni base superalloys involves designing a complete brazing process. The American Welding Society (AWS) defines five important elements of brazing [7]:

1. Joint design – brazing clearance (also termed width or thickness), joint type, and fixture.
2. Base metal (BM) – alloy system, heat treatment, microstructure, compatibility with filler metal.

3. Filler metal (FM) – alloy system, melting temperature, compatibility with base metal.
4. Source of heat – electrical (furnace), torch, exothermic
5. Protective cover – acceptable atmosphere or necessary flux

With each element of brazing is a long list of variables, a few are included above, which usually are connected to multiple elements. For example, the chosen brazing temperature is dependent on the melting range of the filler metal, base metal heat treatment, brazement design, gap clearance, service conditions, and of course cost of materials and processing. The connectivity of these conditions makes brazing a complex process which must be extensively studied to ensure that the resulting product will be successful.

Many brazing processes produce a braze joint weaker than that of the base metal. This restricts the use of the brazed component in service. The low temperature properties of the brazing FM generally cause the low strength of the braze joint. Diffusion brazing is a type of brazing (a subset of diffusion bonding) which can often produce a higher strength joint. In this process, a preplaced FM interlayer is placed between base metal components and clamped at a high pressure (MPa). At the brazing temperature, the FM will melt creating a liquid phase allowing for extensive diffusion of FM elements in to the base metal [8]. The extent of diffusion, a function of brazing temperature and time at brazing temperature, to be achieved is usually determined by the necessary mechanical properties for the application at hand.

Duvall, Owczarski, and Paulonis (of Pratt and Whitney) [9], developed a novel brazing process based on the diffusion brazing process, which created a diffused,

homogeneous joint with the mechanical abilities equivalent to that of the base metal. The process is called transient liquid phase (TLP) bonding and will be described in detail in Section 2.1.

Chapter 2 Background

2.1 Transient Liquid Phase Bonding (TLPB)

Several review papers published in the past 30 years have described the TLP bonding process in detail [10]–[12]. TLP bonding was first described (for industrial and academic purposes), by Pratt and Whitney a subset of United Technologies Corporation (UTC) of Connecticut, USA in 1974 by Duvall et al. [13]. This work pertained specifically to joining of nickel base superalloys and implement these brazed components in high temperature applications [13]. When published, the TLP bonding process was currently in use in production by Pratt and Whitney to join Ni-base superalloys protected under the 1972 patent owned by UTC [9]. A production run of 18 000 turbine vane clusters were produced with 99.8% successfully bonded parts. This initial paper outlines the use of TLP bonding for eight high temperature superalloys: solid solution strengthened cobalt-base cast alloys (MAR-M302, Stellite 31), solid solution strengthened nickel base superalloy (Hastelloy X), and precipitation strengthened nickel base superalloys (Inconel 713C, Udimet 700, IN100, B1900, Mar-M200 + Hf). Filler metal compositions were not explicitly stated (with a few exceptions) but Duvall noted that Ni-Cr and Ni-Cr-Co filler metals were used with the addition of boron (B) as the melting point depressant (MPD) [13]. The TLP bonding patent notes that filler metals containing combinations of boron, silicon, manganese, niobium, and titanium have been evaluated but boron was identified as the only MPD which did not produce an unwanted phase [9].

It is interesting to note that boride formation is observed, in the first paper published by UTC and Pratt and Whitney but the authors were able to achieve sufficient

mechanical properties for their applications [13]. In other applications of TLP bonding with boron filler metals, many researchers have found that borides do have a detrimental effect on the braze joint properties and tend to limit the application of the brazed component [14]. The controversial issue of borides in TLP bonding will be discussed in more detail in Section 2.1.3.

TLPB consists of a base metal (in this case nickel base superalloys) and an interlayer (filler metal) which generally has a composition similar to that of the base metal. The composition of the filler metal is pivotal to ensuring a successful braze and is the subject of significant research in TLPB development. As with conventional brazing, the filler metal must have a melting point significantly lower than that of the base metal to ensure minimal microstructural effect on the base metal and to minimize energy costs. The metallurgical system of the filler metal generally has a binary or ternary eutectic which can be utilised to reduce the melting point significantly though this is not a necessity [12]. Many systems utilize one or several melting point depressants (MPD) which can be manipulated to a composition which allows for timely TLP bonding without using a eutectic composition. The BM and FM alloys must also have good mutual solubility to allow for extensive diffusion of FM elements in to the BM [8].

TLP bonding is a mass transfer process based on diffusion of MPD elements. Melting of the filler metal at the brazing temperature causes rapid diffusion of MPD elements across the solid liquid interface into the base metal. To conserve mass, the liquid phase contracts increasing the volume fraction of the solid phase and inducing solidification at the brazing temperature [10]. This solidification is termed isothermal solidification (IS) as it occurs during holding at bonding temperature (isothermal) and not

on cooling. IS can be partial, in which a portion of the region is isothermally solidified and a portion solidifies on cooling (athermally), or complete in which the thermal process is long enough for the entire bonding region to have solidified at the bonding temperature. IS at the brazing temperature means that the braze joint will have a melting temperature above the brazing temperature

After isothermal solidification of the joint, there is generally still a difference in composition between the solidified joint and base metal. A long heat treatment, called homogenization, can be performed to normalize the composition and create a joint with no variation in elemental composition. This is the proposed final stage of TLP bonding, though even Duvall et al. original TLPB paper noted that, in some cases, the mechanical properties of the joint (tested through tensile testing of a butt joint) prior to homogenization were deemed satisfactory [13].

The process steps of TLP bonding are well defined and will be described in the following section.

2.1.1 TLP bonding process

The process of TLP bonding is dependant on diffusion of MPDs from the filler metal into the base metal. Within TLP bonding there exists some disagreement on naming of the process. For clarity, the process of TLP bonding will be described. The main defining feature that separates TLP bonding from diffusion bonding or brazing is the transient nature of the liquid phase at the brazing temperature.

The TLP bond is described in three (or four) major stages: base metal dissolution, diffusion of MPD elements, and isothermal solidification. The fourth and optional stage is homogenization. As stated previously, the homogenization stage is not a necessary

stage. In many modern day studies of TLP bonding (this work included) homogenization is not a research objective.

It is helpful to examine a typical phase diagram while explaining the TLP bonding process. The system described herein uses a eutectic containing system, but this is not necessary in TLPB. Figure 2.1 adapted from Gale and Butts [11] shows the three major stages present in typical TLP bonding. Initially, a base metal substrate (material 'A') and filler metal (containing material 'A' and MPD 'B') are in contact and heated to brazing temperature T_B. The filler metal can be a preplaced interlayer or placed outside the joint. An interlayer (filler metal foil) is placed in the joint in contact with the substrate, commonly held together with low amounts of pressure. Placing the filler metal outside the joint relies on capillary action to draw the molten filler metal in to the joint. Both filler metal placements require the filler metal to wet the base metal [7].

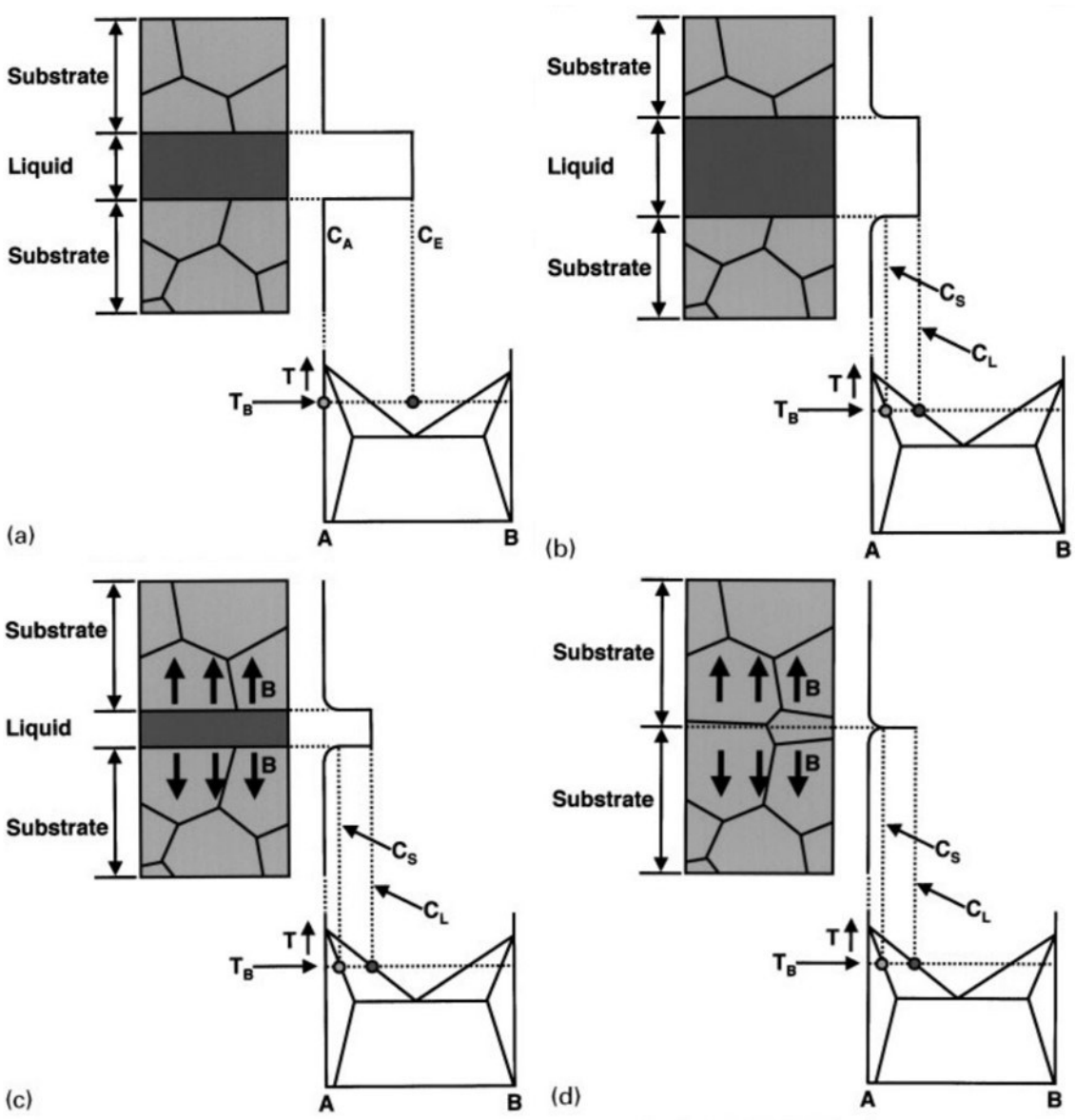

Figure 2.1 – Schematic of TLP bonding stages at bonding temperature (T_B). a) initial condition, b) dissolution of substrate (base metal), c) diffusion of MPD elements and isothermal solidification, d) completion of isothermal solidification. [11]

The component is heated to a bonding temperature carefully chosen to produce a sufficient amount of liquid in the bond region. The "sufficient amount of liquid" is largely dependant on the system and application. Some TLPB processes fully liquify the filler metal to allow for enhanced movement of the metal by capillary action and others create limited liquid in the case that diffusion is sufficiently quick and full densification can occur [10].

At the bonding temperature, T_B, in Figure 2.1a) the 'A-B' filler metal of composition C_E is fully liquid and the base metal substrate is of composition C_A [11]. At the bonding temperature, the liquid FM will partially dissolve or melt back the substrate essentially moving the solid liquid interface. This melt back process occurs rapidly and is dependant on the temperature difference between FM solidus/liquidus and brazing temperature. A larger difference in temperature would promote dissolution of the base metal. The extent of base metal dissolution varies based on composition of the FM and BM, and brazing temperature and is ideally minimized to reduce the possibility of joint erosion. Dissolution can be minimized if there is solid state diffusion between the FM and BM prior to reaching T_B [10].

Once the liquid has reached maximum width, as in Figure 2.1b), the composition of the phases at the solid liquid interface have changed. The liquid has decreased in B content to C_L and the substrate, at the interface only, has increased in B content to C_S. During holding at temperature, the MPD 'B' diffuses into the base metal, as shown in Figure 2.1c). Assuming that the solid liquid interface remains at equilibrium, i.e. compositions C_S and C_L are retained, conservation of mass will cause the liquid phase to contract thus moving the interface toward the centre of the joint [10]. Applying a mass balance to the solid liquid interface, the interface velocity $\left(\frac{dy}{dt}\right)$ is a function of diffusivity (D_S and D_L) and time (t) as described by MacDonald and Eager [12] in Equation 1:

$$\frac{dy}{dt} = K\left(\frac{R_S\sqrt{D_S} - R_L\sqrt{D_L}}{\sqrt{t}}\right) \quad (1)$$

Where R_s and R_L are system specific functions of time and temperature.

The component is held at the brazing temperature until the liquid has completely isothermally solidified by diffusion of 'B' MPD into the base metal as shown in Figure 2.1d). Hold times at bonding temperature vary significantly by system and range from a few minutes to 72 hours [10]. This, of course, is also greatly dependant on the gap clearance to be joined. The joint illustrated in Figure 2.1d), has a solidus temperature just above the brazing temperature, elevated from the initial melting point of the filler metal [10]. If the braze joint is free of detrimental phases and is of sufficient strength at service temperature for the application the process can be stopped at this point.

A "sufficient time" at brazing temperature can be defined as the time necessary for diffusion of MPD elements from the FM to the BM in order to eliminate the liquid phase in the braze joint. This time is dependant on many factors and will be discussed in more detail in Section 2.1.2 and 2.1.4. If the braze joint component is not held at T_B for a "sufficient time" there will be some volume of liquid phase left prior to cooling. This liquid phase will solidify athermally at some temperature below T_B (dependant on the extent of diffusion and initial composition of the filler metal). This distinction in method of solidification, isothermal versus athermal, is important because the athermally solidified phase or region cannot have the same high temperature properties as the isothermally solidified region. In some systems the athermally solidified phase can have a detrimental effect on the properties of the component in addition to the negative effect of the lower melting point.

2.1.2 Microstructure of TLP bonded joints

TLP bonding produces a complex joint microstructure which varies depending on the metallurgical (BM and FM) system and the brazing process used. In Ni base

superalloys there are three distinct regions or zones of the braze joint formed during the thermal process which can help define the success of the brazing process. As expected, the microstructure of the TLP bond is largely influenced by the brazing temperature, time, and BM/FM alloys. A published micrograph by Pouranvari et al. [15] is shown in Figure 2.2 to help illustrate these three zones as found in a TLP bonded nickel base superalloy, GTD-111, brazed with a boron and silicon containing FM, MBF-30. The three zones are:

1. Athermally solidified zone (ASZ) – the region solidified on cooling from T_B with a solidus temperature below T_B. Formed when MPD elements do not sufficiently diffuse out of the joint resulting in liquid present on cooling. In the case of boron containing FM alloys, the ASZ is a network of brittle secondary boride phases [13]. If present, the ASZ will be located along the centreline of the braze joint, but in a properly processed TLP bond the ASZ will not exist.
2. Isothermally solidified zone (ISZ) – a single phase region that solidified at the brazing temperature through diffusion of MPD elements from the liquid FM to the BM. Diffusion and therefore solidification is driven by compositional gradient at the solid/liquid interface. In Ni base superalloy brazing this will be γ-Ni solid solution existing between the S/L interfaces.
3. Diffusionally affected zone (DAZ) – a region of the BM that is enriched in MPD elements which have diffused out of the liquid FM. This zone can be solid solution with composition gradient or have precipitated secondary

phases. The microstructure and width of the DAZ is highly dependant on the BM and FM composition, and the brazing temperature and time.

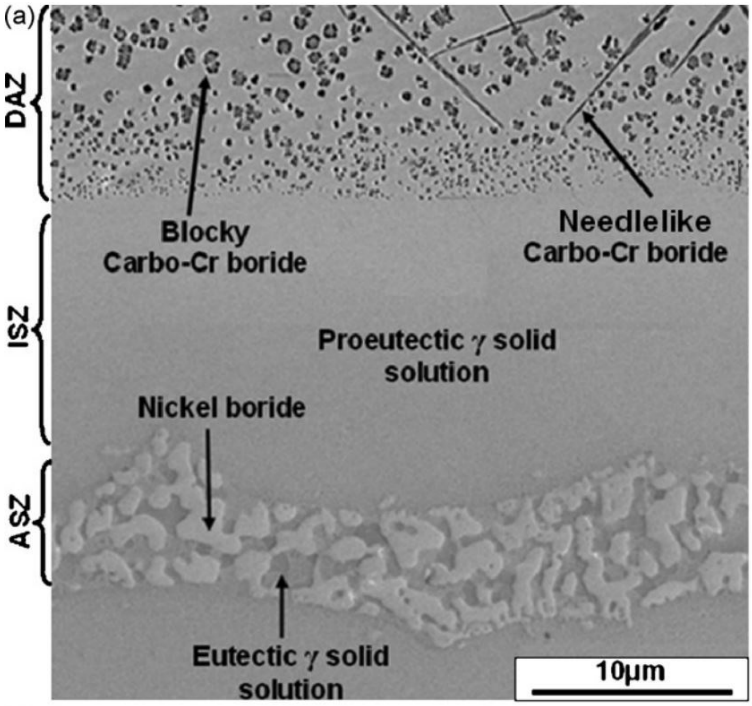

Figure 2.2 – Micrograph TLP brazed joint of GTD-111/MBF30 at 1100 °C for 30 min [15].

The effectiveness of the brazing process will determine the microstructure of the braze joint. If complete IS has occurred, there will be no ASZ present, and the braze joint will be fully ISZ. The DAZ, will be present even if complete IS has occurred (and no homogenization stage has occurred). The phases present in the ISZ, ASZ, and DAZ, will depend on the chemistry of the system. The microstructure shown in Figure 2.2 is a Ni base superalloy (GTD-111) BM and Ni-Si-B FM (MBF30). Ni-Si-B is a typical FM alloy system used extensively in TLP bonding.

2.1.3 Common filler metals in TLPB of Ni base superalloys

Many filler metals are applicable for TLPB of Ni base superalloys. The AWS brazing handbook [7] notes that filler metal classifications with principal elements Ni,

Co, Au, Ag, and Cu are suitable for brazing Ni alloys. Within each of these classifications many filler metals exist with various alloying elements designed to meet certain applications. Ni base FM alloys (classified by AWS as BNi) are the most common utilizing silicon, boron, and phosphorous as MPD. Cr and Fe are often present in BNi FM alloys to more closely match the composition of Ni base superalloys and increase the corrosion resistance of the braze joint [13].

Boron containing FM alloys utilize the eutectic point of the Ni-B system (3.6 wt% B) and Si (4-5 wt%) to decrease the solidus temperature to 971-980 °C and liquidus temperature to 999-1077 °C (depending on other alloying element composition) [7]. The brazing temperature range, recommended by AWS, is 1010-1204 °C (depending on BM, brazement design, and operating conditions) [7]. Boron containing alloys have had a high rate of success in TLP bonding of Ni base superalloys due to the relative low cost, good flow properties, and melting point [16]. The low cost is not only based on material cost of the FM alloy but also on the processing cost. The small atomic radius of boron (0.080 nm) compared to Si (0.111 nm) and Ni (0.125 nm) allows for interstitial diffusion of B into Ni, and substitutional diffusion of Si in Ni. Interstitial diffusion, by it's very nature, will be significantly more rapid than substitutional [17] which allows for relatively short hold times at brazing temperature. The short hold times translate to low energy costs; an attractive attribute.

There are well documented drawbacks to the use of boron as an MPD. Because boron has such a high diffusivity rate compared to silicon and a low solubility in Ni, boron diffusing in to the base metal reacts with nickel, and chromium to precipitate brittle borides [18]. In small concentrations, borides can be a minor strengthening precipitate but

the increased amount of borides present around a braze joint is detrimental to the strength and ductility of the joint [3]. These borides, characterized by high hardness and brittleness, are found to be the most significant factor in the reduced strength and operating temperature of brazed Ni base superalloys.

Boron affects the microstructure of the bonded joint in two ways. The first, through athermal solidification and segregation of boron in the centreline eutectic phase of the joint. This results in large eutectic borides which are largely avoided when IS is complete. Borides also precipitate in the grain boundaries of the DAZ, adjacent to the joint. Henhoeffer et al. [19] showed that a cobalt based superalloy X-40 brazed with Ni-Cr-B FM (BNi-9) had a reduced fatigue life compared to the base metal. The reduction was attributed to brittle borides in the braze joint. Extensive fracture analysis in another work by Henhoeffer et al. [20] showed that borocarbides in the DAZ initiated fracture in tensile specimens. Reduced ductility was also found in both studies. Chen et al. corroborated this decrease in strength [21] and fatigue properties [22] in work examining the mechanical properties of IN625 BM bonded with Palnicro36M (Ni-P-Cr-B-Si) FM.

The presence of brittle borides was mentioned in the first paper by Duvall et al. in 1974 [13] but were able to be avoided by manipulating a combination of filler metal composition, and thermal brazing profile. Using Udimet 700 (precipitation hardened alloy) as an example, the authors found that a joint vacuum brazed at 1141 °C (2140 °F) for 24 hrs using a FM alloy of composition Ni-15Cr-15Co-5Mo-2.5B resulted in a fully homogeneous joint with no indication of borides [13]. Another example by Duvall et al. examined IN713C (FM composition not given) brazed at 2140 °F (1141 °C) for 24 hrs and 2000 °F (1093 °C) for 4 hrs. The shorter/cooler process resulted in an isothermally

solidified joint with sufficient mechanical properties but a composition gradient across the joint width. The longer/hotter process resulted in a fully homogeneous joint with mechanical properties identical to that of the base metal [13]. Both of these FM alloys contained boron, but the detrimental effect of borides was not noted by the authors.

Because of these well documented detrimental phases, significant research into using alternative MPD elements has been undertaken by many groups though industrial application has been limited. The research into alternative MPD used in Ni base superalloy TLPB is outlined in Section 2.3.1.

2.1.4 Determination of TLPB processing parameters

An important step in ensuring the braze joint completes IS is determining the correct process parameters by examining the kinetics of the process. While it is not possible to consider all parameters in this work, the most important and basic parameters will be examined. As explained in Section 2.1.1, achieving "sufficient time" at brazing temperature is imperative to the success of the brazed component but determining this parameter is complex.

The elements of brazing affecting the time needed to complete TLP bonding in the braze joint are: gap clearance (also termed joint width or thickness), brazing temperature, filler metal and base metal compositions, interdiffusion rate of MPD and BM elements, and expectation of joint composition (i.e. isothermal solidification only, or full homogenization). The gap clearance, brazing temperature, and brazing time have a well established relationship for a given metallurgical system. At a certain temperature, the isothermal solidification time decreases with decreasing gap clearance. As the gap clearance decreases, the initial volume of liquid is decreased with a constant diffusion

coefficient (m^2 s^{-1}), it will take less time to diffusion the MPD elements out of the braze joint. Conversely, at a certain gap clearance, the isothermal solidification time decreases with increasing brazing temperature [7]. Exceptions to this rule could exist if dissolution of the base metal is significantly increased at higher temperatures.

An accepted experimental technique used to determine the kinetics of TLP involves metallographic analysis to measure the width of the ASZ after a series of hold times at the brazing temperature. In systems utilizing a eutectic phase, the ASZ can be easily identified by optical microscopy, as shown in Figure 2.2 and confirmed by elemental analysis. The measured width of the ASZ is then compared to the total braze clearance (or width) to determine the extent of IS. This procedure is repeated at multiple brazing temperatures and/or brazing hold times depending on the intent of the research. Measuring the width of the ASZ at one cross section location in the sample can lead to a significant source of error in the work. Additionally, the solid-liquid interface is generally not planar which leads to a large variance in ASZ width measurements [23].

This metallographic technique has been coupled with a wedge type sample, in which the full gap width or (brazing clearance) increases from 0 to 100 μm in a single sample. Lugscheider and Partz [24] used this method to determine the maximum brazing clearance (MBC) of several high temperature brazing systems. Maximum brazing clearance is the clearance (gap width) that achieves full IS for certain brazing parameters. Above the MBC, an ASZ will be present [7].

An alternative method to measure the kinetics of the TLP bonding system is to use thermal analysis. This will be described in Section 2.2.1.

2.2 Use of DSC in TLPB

Thermal analysis is a branch of materials engineering and science which aims to analyse the change in material properties during a changing temperature profile [25]. A common instrument used in thermal analysis is the differential scanning calorimeter (DSC). A DSC measures the temperature difference between a reference and sample during exposure to a heating or cooling thermal profile. The instrument used in this work is a heat flux DSC which consists of sample and reference crucibles with thermocouples in a small cylindrical furnace with one heating element. The sample carrier connects the sample and reference by a thin platinum strip which measures the difference in signal (in terms of voltage) between the sample and reference [26] as shown in Figure 2.3. The actual temperature difference is measured by the voltage difference between the B legs [26].

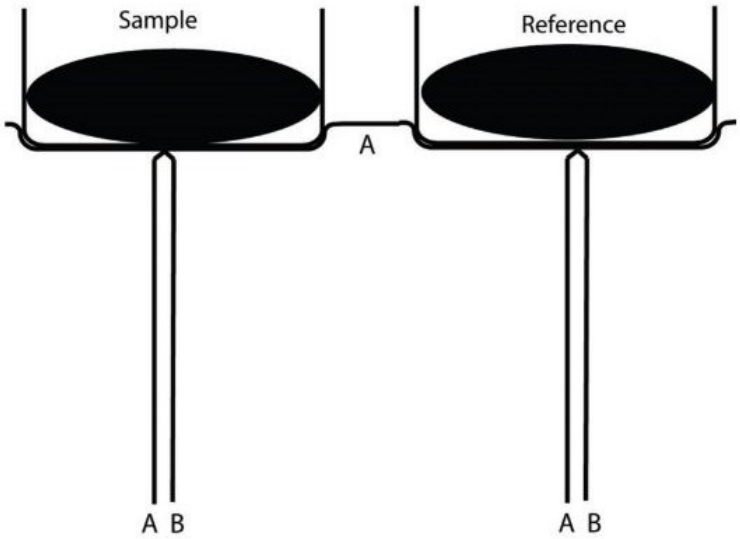

Figure 2.3 – Crucible and thermocouple set up in a typical HF-DSC [26].

The proposed research will use Dalhousie's Netzsch Pegasus 404 pictured in Figure 2.4. The raw data obtained by the DSC, in mV, can be converted to heat flux by a calibration factor. The measured voltage difference between the sample and reference is

converted to power and can be plotted versus time or temperature. The calibration involves melting pure metals, with well defined melting points, and measuring both the area of melting event, and the onset temperature of melting. The pure metals chosen for calibration should have melting points which cover the temperature range at which thermal events will take place.

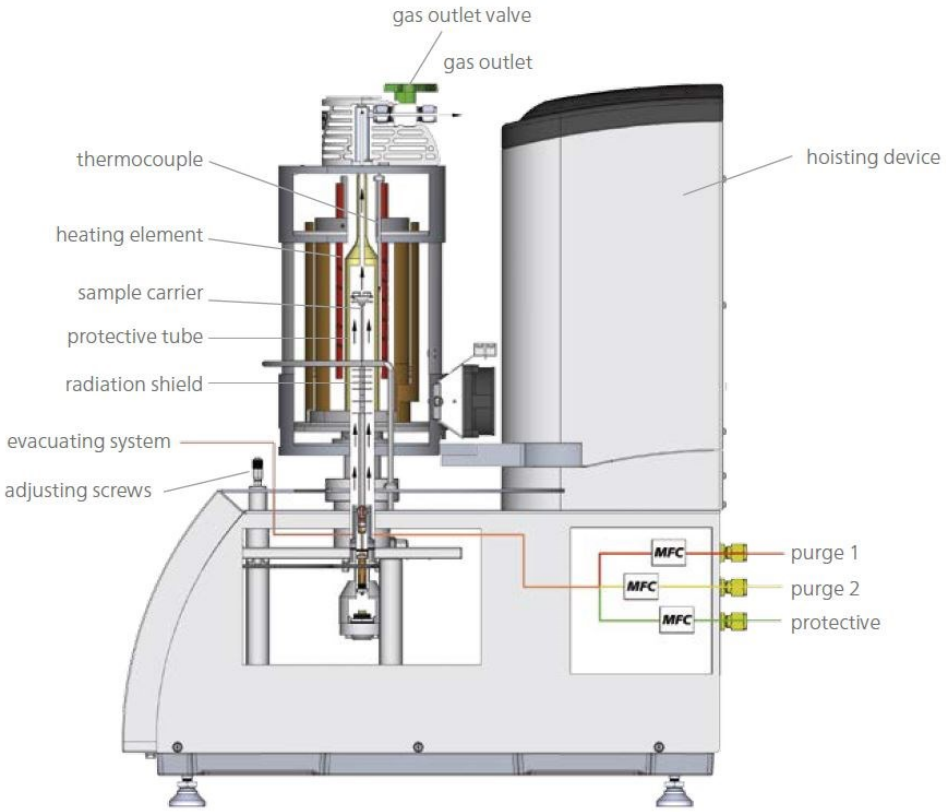

Figure 2.4 – Schematic of Dalhousie's Netzsch DSC 404 F1 Pegasus [27].

An example of a simple DSC trace of the melting and solidifying of a pure metal, Au (m=22.46 mg), is shown in Figure 2.5. Alumina sample and reference crucibles with lids were used. A ramp rate of 20 °C/min was used on heating and cooling, and Ar flow rate of 50 mL/min. In this work, exothermic is considered negative or "down" meaning that a peak evolving in the positive direction on a DSC trace is an endothermic event (usually melting).

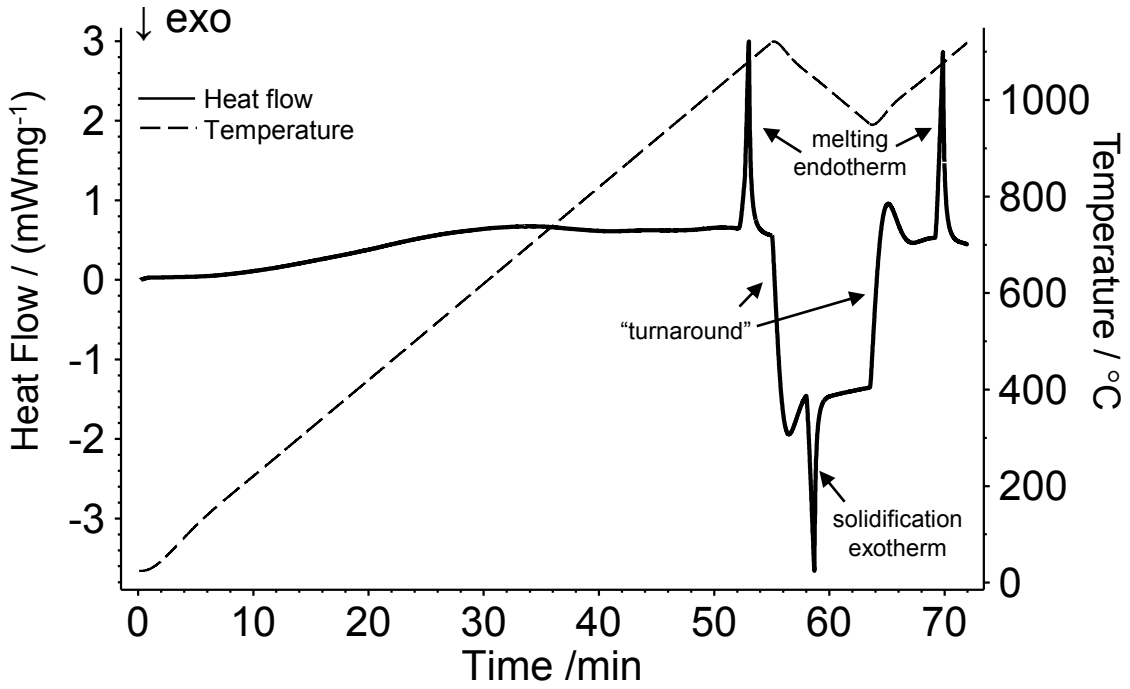

Figure 2.5 – DSC trace of a gold sample.

Two melting endotherms, and a solidification exotherm are shown in Figure 2.5. The enthalpy of melting and solidification events can be determined by measuring the area of the endothermic peak and exothermic valley respectively. The solidus and liquidus temperature can be determined by the onset and end of the endothermic melting peak. The feature in Figure 2.5 denoted "turnaround" is the drastic change in DSC baseline caused by the change in heating rate from + 20 °C/min. to – 20 °C/min. This is an artifact of the instrument and is not indicative of a reaction of phase transformation. When analysing a DSC trace, it is important that the user has familiarity with the system so that artifacts of the instrument are not misinterpreted as phase transformations.

2.2.1 Quantifying kinetics of TLPB using DSC

Thermal analysis lends itself well to examining the progression of TLPB. Work by Corbin et al has successfully developed a technique using DSC and thermal analysis to investigate and quantify the stages and progression of TLPB. This technique was

developed to examine TLP sintering and brazing of filler metals [28], [29], solid/liquid diffusion couples [23], and specifically applied to TLP bonding in the 2005 thesis by Kuntz [30]. The nature of measuring the enthalpy by thermal analysis means that it considers the entire sample at once rather than one cross section of the sample in metallographic methods of TLPB kinetic determination as described in Section 2.1.4.

As applied to TLP bonding, the initial liquid formation on melting, kinetics of the system, and progression of isothermal solidification can be measured and quantified in situ. The technique measures the enthalpy of melting and/or solidification events of the system after various hold time at brazing temperature.

In the paper by Corbin and Lucier [28] examining the Pb-Sn system for soldering it was shown that the kinetics of isothermal solidification could be quantified using DSC. A great example showing, qualitatively the progression of isothermal solidification as a function of time at brazing temperature is shown in Figure 2.6. It was found that when a Pb-Sn FM alloy was held at 186 °C (slightly above the eutectic temperature), cooled, and remelted, the enthalpy of solidification and remelting peaks were similar and significantly less than the initial melting peak. This indicates that isothermal solidification at the brazing temperature did take place. Increasing the hold time at brazing temperature resulted in a decrease in solidification and remelting enthalpy as shown in Figure 2.6.

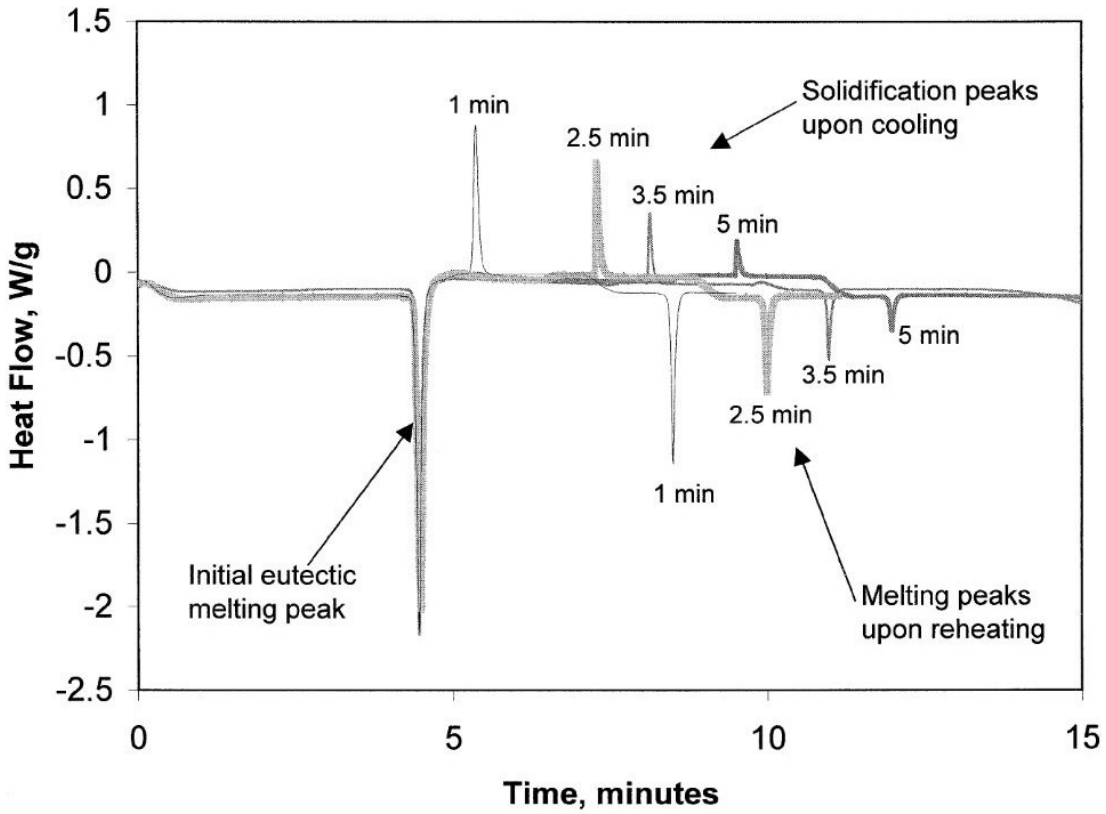

Figure 2.6 – DSC trace of Pb-Sn solder alloy heated to 186 °C and increasing the hold time [28].

Because isothermal solidification is a diffusion based process, increasing the time at the brazing temperatures reduces the volume fraction of the liquid left on cooling (ASZ) which will decrease the enthalpy of solidification and remelting. The reduction in ASZ (eutectic Pb-Sn in this case) was confirmed by microstructural analysis which showed that the fraction of eutectic phase decreased with increasing hold time at brazing temperature [28].

In a recent paper, Murray and Corbin [31] expanded upon previous DSC TLPB work by applying a cyclic DSC method to measure the kinetics of IS with a single sample. Instead of preparing multiple samples each with a different hold time, one sample is prepared and subjected to a cyclic thermal profile. This work used an IN625/BNi-2 brazing joint. After initial heating to brazing temperature, the sample was

held for 5 min, cooled below the solidus temperature, reheated to brazing temperature, and held for 5 min. This cyclic thermal profile was repeated, and the enthalpy of solidification and melting was measured at each cycle. The enthalpy of solidification was found to decrease with each subsequent cycle until it reached 0, indicating that complete IS had been achieved. The cyclic DSC method has also been successfully applied to TLPB of aluminum alloys using a Al-Si FM [32].

The measured enthalpy at a corresponding hold time at T_B can be related to the percent of liquid left on cooling, the width of the ASZ, and, finally, the maximum brazing clearance. The maximum brazing clearance is the clearance (or gap width) at which complete IS has taken place for a certain hold time [7]. These relationships were examined and are quantified in detail in Section 5.7.2.

2.3 Review of boron free brazing literature

2.3.1 Use of alternative MPD

The development of boron free filler metals to braze Ni-based superalloys has recently been an active area of study, with the goal of reducing joint embrittlement. A number of alternative (boron free) braze metals have been researched but none have experienced commercial application as significant as boron containing alloys.

One such alloy comprised of nickel, chromium, silicon and phosphorous, achieved comparable strength to that of the base metal [33]. FM alloy development has also utilized phosphorous as an effective MPD added to a Ni-Cr-Fe alloy. A drawback to this alloy is the high brazing temperature of 1095 °C. This is above the established brazing temperature limit of 1050 °C. Phosphorous will alloy with many metals to precipitate phosphides, a brittle phase which has been shown by Jalilian et al. [34] to

precipitate in grain boundaries and within the grains of the DAZ. This brittle phase can have a similar effect on the mechanical properties as borides due to their similar high hardness, and brittle characteristics. The kinetics of phosphorous FM alloy was reported to be slow compared to boron, requiring 14 and 18 hours at 1150 °C to braze with a 25.4 and 38.1 μm interlayer respectively [34]. A boron and phosphorous free filler metal, BNi-5, uses silicon as the MPD with added Cr but can also develop a hard and brittle silicide phase which can have detrimental effects [24].

Figure 2.7 shows the brazing temperature for several researched alternative MPDs used in boron free FM development. A common drawback in many boron free filler metals is the system's need for a high brazing temperature. BNi-2 filler metal (Ni-Cr-Si-B) can be brazed at 1050 °C, well below most alternative MPD systems as shown in Figure 2.7.

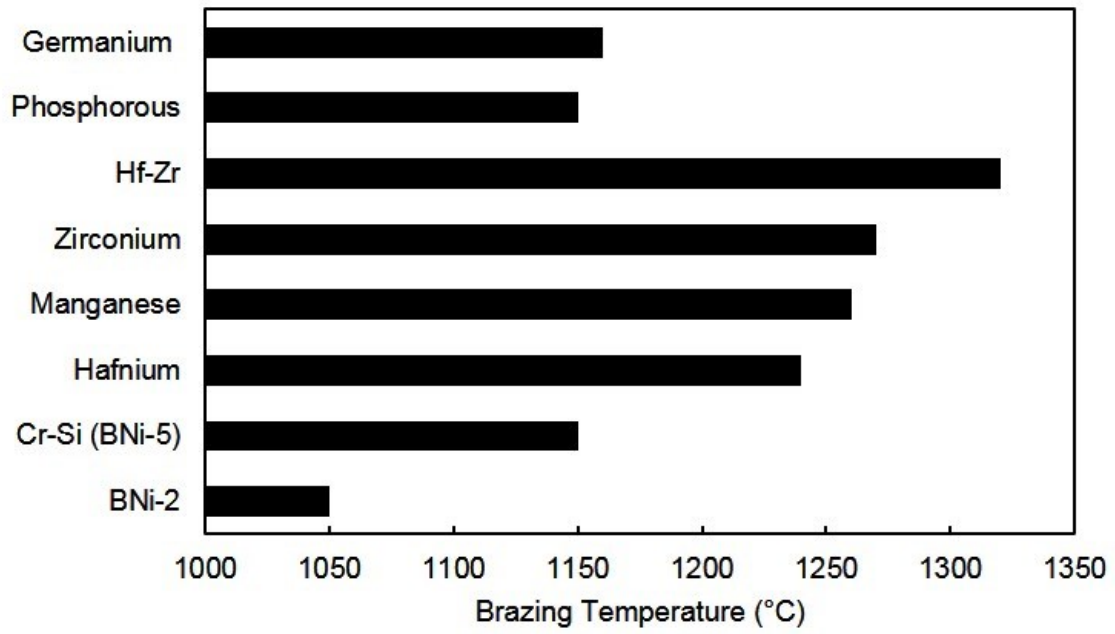

Figure 2.7 – Brazing temperature of common FM alloys used in TLP bonding of Ni base superalloys [24], [33]–[41]

Buschke and Lugscheider [35] investigated nickel hafnium braze metals with additions of cobalt, chromium, and molybdenum. Additions of 7 wt% Hf required a brazing temperature of 1235 °C, above the IN625 solution treating temperature of 1150 °C [3]. High strength, corrosion resistance, and ductility were reported with this alloy [35].

Zheng et al. [40] used a 50 μm multi-component (Co, Cr, W, and Zr) boron free filler metal containing 13 wt% Zr to TLP bond single crystal superalloys at 1270 °C. Complete isothermal solidification was achieved after 48 hours of braze time. Work by Huang [36] used a boron free filler metal containing both Hf and Zr to braze CMSX-4 superalloy BM at a temperature of 1240 °C for 40 minutes. Intermetallic phases remained at the joint but were reduced in volume fraction after a 10 hour homogenization period at 1200 °C.

Khorunov and Maksymova [18] found that in a Ni-Cr-Zr system high levels of Cr (15 to 24.4 wt%) caused significant erosion of the base metal and a Cr-Ni eutectic structure at the BM interface indicating IS was not complete. In addition, these high levels of Cr reduced the wetting ability of the FM alloy and did not perform well in narrow (20 to 30 μm) capillary brazing experiments. These experimental FM alloys used a brazing temperature of 1160 to 1220 °C.

Work by Heinz et al. [38] and Dinkel et al. [39] explored the use of germanium as an alternative, boron free MPD. Brazing of superalloys using a Ni-23% Ge filler alloy was successful at temperatures in the range of 1160 to 1260 °C. Complete isothermal solidification (IS) within a 200 μm wide gap was possible at the lower braze temperatures, after times of 24 to 48 hours. Zhongci et al. [37] used 50 to 70 μm thick Ni-

Hf based boron free fillers to TLP bond Ni-based superalloys at temperatures of 1240 to 1280 °C, where complete IS was achieved in 48 hours. Miglietti and Du Toit, [42], [43] investigated the use of Ni-Cr-Hf and Ni-Cr-Zr boron free fillers to join IN738 plates. They explored both narrow gap and wide gap TLPB at a brazing temperature of 1238 °C. Narrow gap joints had residual centreline Hf or Zr based eutectic regions present after 18 hours of isothermal hold time (i.e. IS was incomplete). Wide gap joints exhibited lower amounts of eutectic and good mechanical properties.

The previously discussed studies focussed on boron free MPD additions which develop a lower temperature eutectic melting event involving solid solution Ni and an intermetallic phase (i.e. Ni_5Zr, Ni_5Hf, and Ni_3Ge). Therefore, to avoid the formation of intermetallic compounds in the joint, complete isothermal solidification was required. As the above studies indicate, this often necessitated long brazing times at high temperatures for the boron free alloy compositions that were studied.

Another possible route is the application of a solid solution FM alloy without using a eutectic forming system. This has been applied by FM alloys using precious metals (AWS alloy name BAu and BAg) and copper (AWS alloy name BCu and BCuP) as MPDs. Noble filler metals utilizing gold, silver, and palladium have a brazing temperature between 900 and 1300 °C [14]. Because of the high cost of precious metals, industrial application of these FM alloys has been limited. Copper has also been used as a MPD to braze steel (stainless, low carbon, and alloy), nickel, and copper nickel [7].

2.3.2 Ni-Cu-Mn braze alloy system

Examining the above literature, it is clear that a significant limitation in developing a boron free FM alloy is an economically, and industrially viable braze

temperature and brazing time. The potential commercial application of this work limits the brazing temperature to 1050 °C. Ideally, the new boron free FM would have IS kinetics similar to that of BNi-2, reported in literature between -3.5 to -8.5 μm $min^{-1/2}$ [31]. To avoid detrimental phases, a solid solution FM alloy approach will be taken. This work aims to utilize the Ni-Cu-Mn system as a basis for a novel boron-free FM for Ni base superalloy brazing.

The use of the Ni-Cu-Mn system as a braze alloy has been briefly examined at the E.O. Paton Welding Institute in Ukraine. Diverse compositions (nickel-rich, manganese-rich, and copper-rich) of this system were examined while brazing cryogenic steel with mixed results. The nickel-rich braze alloy showed high strengths but all alloys had limited diffusion into the base metal [44].

The Ni-Cu-Mn ternary liquidus diagram is shown in Figure 2.8. The ternary system at liquidus shows complete solid solution (γ) at all compositions with no intermetallic phases present. Therefore, during cooling, no eutectic solidification event and associated intermetallic compounds will form in the ASZ of the joint. The depressed melting point effect of Mn and Cu is evident in the liquidus diagram. A commercially available master alloy (MA) filler metal of composition 52.8wt% Cu, 37.5wt% Mn and 9.7wt% Ni (AMS 4764F or NiCuMan37) is shown to have a liquidus temperature of approximately 940 °C. AMS4764 has been used in vacuum brazing of WC-Co cutter bits to high-carbon tool steel at 950 °C [7].

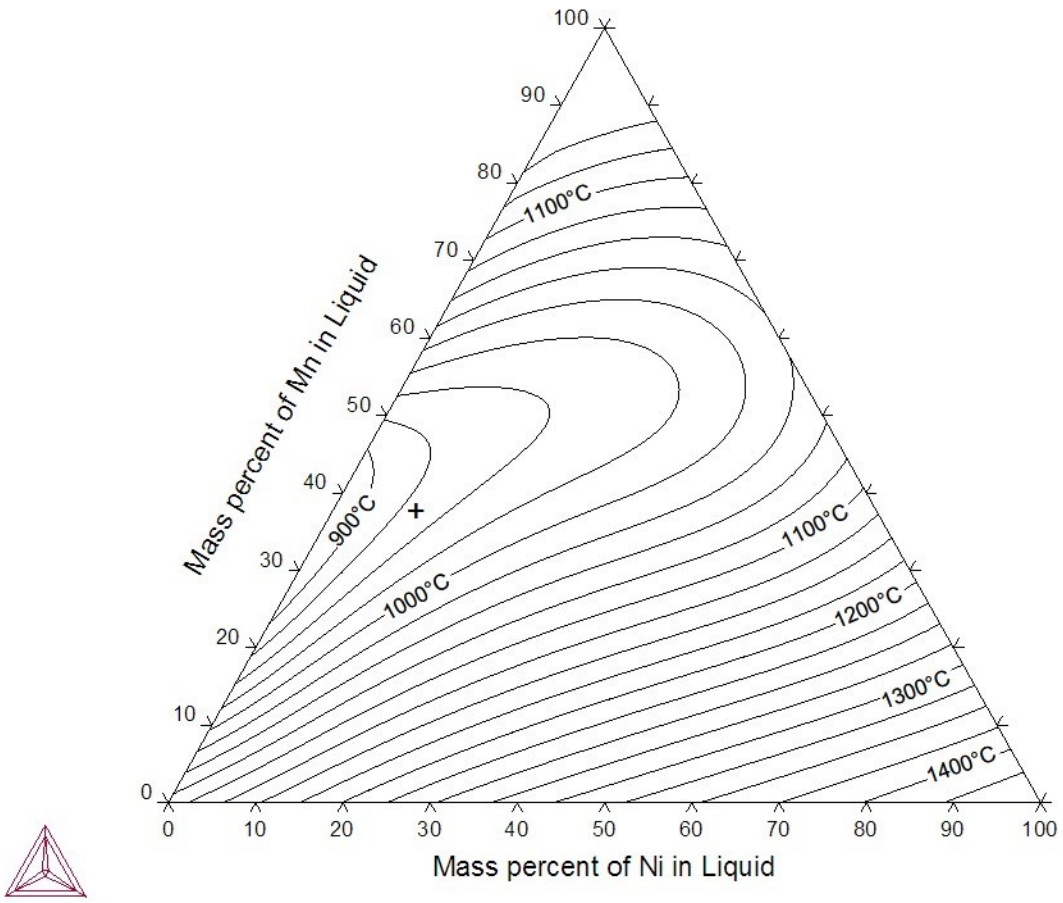

Figure 2.8 – Ternary phase diagram of Ni-Cu-Mn system produced using Thermo-Calc [45]. + indicates composition of NiCuMan37 (AMS4764F).

Roy et al. [46] used an alloy of similar composition to join 304 stainless steel using conventional, non-TLPB brazing at 1000 °C for 5 minutes. The joints consisted of a single-phase solid solution and exhibited joint strengths in the range of 70% of the base metal. Roy et al. point out that this joint strength is significantly higher than that achieved through brazing stainless steel with the boron and silicon containing BNi-2 filler metal. An advantage of the AMS 4764 is the low solidus and liquid temperature of 900 and 940°C. Examining the liquidus diagram in Figure 2.8, increasing the Ni content of Ni-Cu-Mn alloys up to 30 wt% is predicted to increase the liquidus temperature to

approximately 1050°C. This was confirmed by Sun et al. [47] and Bazhenov [48] in separate works modelling the Ni-Cu-Mn phase diagram.

Work by Laux et al. [49], [50] investigated a Ni-Mn based filler metal to join and repair single crystal Ni-based superalloys at braze temperatures above 1160 °C. Mn exhibits complete solid-state solubility in Ni above 900 °C. Slow cooling from the braze temperature was used to control the athermal solidification process and joint microstructure. Using only manganese as a melting point depressant produced a liquidus of 1120 °C but the system required a brazing temperature of 1260 °C [50]. Braze repair of single crystal alloys has a different objective than TLPB, complete homogenization and removal of grain boundaries, which may have influenced the high brazing temperature used in the works.

Ghasemi and Pouranvari [51] examined a 50 μm pure copper interlayer to TLP bond Monel 400 (Ni-31.5Cu) at 1120 °C. The purpose of the study was to compare the kinetics of a boron containing FM, MBF-30 (Ni-3.2B-4.5Si), and pure Cu. Cu has full solubility in Ni, and no intermediate phases have been reported. This means that the braze joint will have a solid solution microstructure even if IS is not complete. In this work IS was confirmed by SEM/EDS elemental analysis. It was found that the isothermal solidification time when using the pure Cu FM was 23 times faster than the boron containing FM alloy (MBF-30). This was attributed to the high solubility of Cu in Ni which led to a high driving force for Cu-Ni interdiffusion which allows for isothermal solidification. The high brazing temperature in this work led to excessive grain growth of the Monel400 base metal [51].

After careful analysis of the above studies, a promising, but previously not studied, direction can be developed by combining aspects from several studies. The Ni-Cu-Mn system can be manipulated by altering the composition. According to the ternary phase diagram, the liquidus can remain below 1050 °C if the nickel content is below 30 wt% and the copper content is increased to approximately 50-60 wt%. As found by Huang [36], increasing the amount of pure nickel in the braze alloy will increase diffusion rates at lower temperatures further decreasing the time to complete IS.

Chapter 3 Research Objectives

The objective of the proposed research is to develop a boron-free braze alloy based on a Ni-Cu-Mn composition to braze IN625 by TLPB. The novel FM alloy and the brazing process will be designed to satisfy the following specifications:

- liquidus below 1050 °C
- solid solution joint microstructure free of detrimental phases
- good solubility of MPD elements in Ni
- mechanical properties comparable IN625

TLP bonding of IN625 is a complex subject so it is helpful to establish the scope of the project with respect to the AWS defined elements of brazing to focus this thesis. The scope is as follows:

1. Design – Joint designs assessed will be half braze joints, and single lap joints. Tack welding will be performed on single lap joints as the fixture.
2. Base material – solid solution strengthened IN625. Microstructure and material strength will be assessed.
3. Filler material – new alloy will be developed using a defined brazing temperature of 1050 °C, brazing time will be assessed. Microstructure and joint strength will be assessed.
4. Source of heat – furnace brazing using resistance electrical heating using variable heating rates.
5. Protective cover – Samples will be brazed under flowing high purity argon (Ar) gas.

The major focus of this work is the development of the filler metal for use with IN625. While IN625 is the only base metal used in this work, it is probable that the filler metal will be compatible with other nickel-base superalloys.

Chapter 4 Experimental Methods

This thesis research was comprised of three phases: development and characterization of a novel braze FM alloy, application of novel FM alloy to half braze joint configuration including a determination of IS kinetics, and mechanical testing of single lap joints prepared with the novel FM alloy. A pivotal aspect of the research is the use of thermal analysis using differential scanning calorimetry, this will be described in detail in Section 4.3.

4.1 Novel braze alloys

A pre-alloyed master alloy from Vitta Corporation (trade names VittaBraz 1764, AMS 4764F, and NiCuMan37) was chosen as the base FM composition and is denoted Ni10. This master alloy has a d_{50} of 30 µm. Two additional compositions of FM alloys were studied, in which the nickel content was increased to 20 and 30 wt% by the addition of a 99.8% pure Ni powder. These are termed Ni20 and Ni30 respectively and compositions are included in Table 4.1. The 99.8% Ni powder, obtained from Alfa Aesar, were determined to be spherically shaped with a d_{50} of 10.1 µm. A maximum nickel content of 30 wt% was used to ensure that the liquidus temperature of the braze remained below the desired brazing temperature of 1050 °C.

Table 4.1 – Nominal composition of experimental FM alloy mixtures

	Composition (wt%)		
Alloy	Mn	Ni	Cu
Ni10	37.5	9.7	52.7
Ni20	31.6	20	48.4
Ni30	27.6	30	42.2

The Ni20 and Ni30 braze powder mixtures were blended by milling the powders for 30 minutes in a small (15 mL) vial with no grinding media present. The melting

behaviour of all three powder mixtures was determined using a Netzsch DSC 404 F1.To characterize the filler metals alone, approximately 100 mg each of Ni10, Ni20 and Ni30 powder mixtures was weighed into an alumina crucible and heated in the DSC.

4.2 Half braze joint experiments (narrow and wide gap)

A half braze joint (HBJ) configuration involves a filler metal in contact with one faying surface of a base metal as shown in Figure 4.1. In contrast, a full braze joint (FBJ) consists of a filler metal sandwiched between two base metal pieces in contact with two faying surfaces. Results of a HBJ configuration (of gap width or clearance *w*) correlate well to a FBJ configuration (of gap width or clearance *2w*). The sides of the IN625 base metal ingot were coated with an yttrium oxide layer thereby restricting metallurgical contact to only the filler metal powder and the bottom faying surface of the IN625 cylinder. Note that the FM alloy was placed on the bottom of the crucible to ensure the most accurate thermal reading from the DSC.

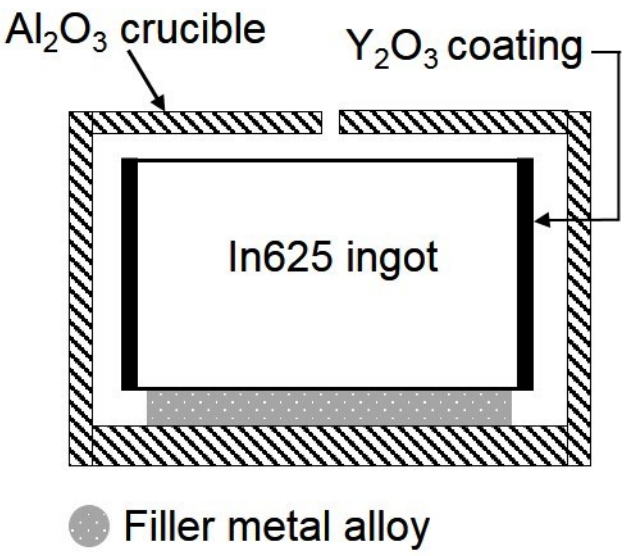

Figure 4.1 – Schematic of half braze joint set up in alumina DSC crucible.

Both narrow and wide gap HBJ conditions were examined in this work. Narrow gap conditions used 7 mg +/- 0.5 mg of loose powder, and wide gap used a 20 +/- 2 mg pressed powder disc. Wide gap Ni30 blended powder was pressed (~120 MPa) into a cylinder (diameter 4.7 mm) in a Carver punch and die set. The pressed disc method was developed to allow for an even distribution of filler metal to base metal prior to melting. In both cases the FM powder mixture was placed in the DSC alumina crucible and an IN625 ingot (4.8 mm diameter × 3 mm height) was placed on top. Previous work by Murray and Corbin [31] on braze half joints using boron containing fillers of a similar density as the Ni-Cu-Mn mixtures indicated that a braze foil mass of 7 mg achieved roughly a 50 μm filler thickness uniformly spread over the base metal.

The initial thickness of a solidified disc of Ni30 was determined by melting a series of 7, 20, and 40 mg of Ni30 in an alumina crucible in DSC, and pressing the resulting solidified sphere into a disc of diameter 4.7 mm. With this method, it was determined that the initial thickness of a 20 mg sample (wide gap) is 127 μm, and the thickness of a 7 mg sample is 44 μm. These values will be used in maximum braze clearance calculations in Section 5.7.2.

IN625 base metal, sourced from McMaster-Carr, was machined by wire electrical discharge machining (EDM) into small cylindrical ingots measuring 3/16” (4.8 mm) diameter × 1/12” (2.1 mm) in height. The faying surface of the IN625 sample was ground with 500 grit SiC paper and cleaned with acetone in an ultrasonic bath.

All brazing of HBJ samples took place in a Netzsch DSC 404 F1. The operation of the equipment and experimental methods will be covered in Section 4.3.

4.3 Differential Scanning Calorimetry (DSC)

The DSC used in this work is Netzsch DSC 404 F1 Pegasus, a schematic is shown in Figure 2.4. This instrument has a platinum furnace and maximum operating temperature 1500 °C. Calibration involved melting In, Sn, Zn, Al, Au, Ag, and Ni samples and comparing the measured enthalpy of melting and onset temperature.

To reduce the oxygen content of the furnace atmosphere, the DSC is run under flowing high purity (99.999 %) Ar gas. The gas is introduced to the system through the bottom of the furnace and passes by an Oxygen Trap System (OTS ®) which aims to scrub any O_2 from the flowing Ar gas environment. A metallic (zirconium alloy) oxygen "getter" is placed just below the sample stage to remove O_2 immediately before it reaches the sample. Calibration of the instrument is performed with the getter in place.

All DSC runs used alumina sample and reference crucibles procured from Advalue Technology (USA) with removable lids. Alumina crucibles were chosen because it does not metallurgically interact with Ni alloys. The mass of the sample crucible was recorded before and after each DSC run to track any changes in mass which may have influenced DSC trace.

In this work three types of experiments with different thermal profiles were examined: isothermal hold, isothermal hold + remelt, and cyclic. Examples of each thermal profile when the specified isothermal hold time is 180 min, are pictured in Figure 4.2. In isothermal hold tests, the DSC was heated to 1050 °C, held for a specified amount of time and cooled to room temperature. In cyclic tests, the DSC was heated to 1050 °C held for 60 minutes, cooled to 900 °C, and reheated to 1050 °C. This was repeated for a

specified number of cycles. Isothermal hold + remelt tests were heated to 1050 °C, cooled to 900 °C, heated to 1050 °C, and cooled.

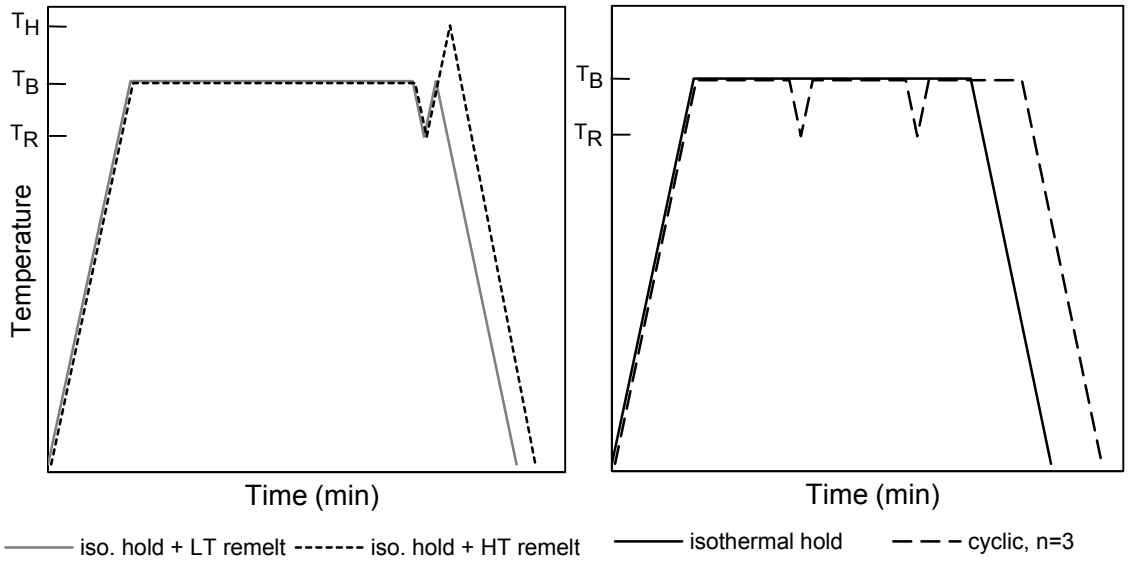

Figure 4.2 – Example DSC thermal profiles used for analysis of a 180 minute brazing process. T_B is the brazing temperature of 1050°C, T_R is the remelt temperature of 900 °C, T_H is the high temperature remelt of 1200 °C.

The remelt testing procedure was developed to more accurately measure the enthalpy after time at braze temperature. Because the liquidus of Ni30 is only 10-15 °C below 1050 °C, and no undercooling is present, samples which have liquid present begin solidifying immediately on cooling. Consequently, the solidification event is obscured by the drastic turnaround, as shown in Figure 2.5, in heat flow signal caused by the changing heating rate in the DSC. This makes the solidification event on cooling difficult to accurately measure and compare with other samples. A remelt in thermal profile after solidifying allows for measurement of the melting event up to 1050°C. Any melting event occurring on the remelt portion of the experiment must have been solidified on cooling from 1050 °C to 900 °C. The remelt enthalpy can then be compared to the enthalpy of remelt for cyclic samples.

4.4 Metallographic preparation and microscopy

After brazing, samples were first macroscopically examined to determine wetting response using a Zeiss stereomicroscope. Half braze joint (HBJ) samples were hot mounted using Struers Citopress-1 in PolyFast, a bakelite resin with conductive carbon filler. A Struers Tegramin-20 was used for grinding and polishing. Grinding and polishing followed standard procedure by grinding on progressively fine Si-C grit paper (220, 320, and 500 grit) and polishing with diamond suspensions (9, and 3 μm) and finishing with a 0.04 μm colloidal silica suspension. Etching was performed on polished surfaces (where noted) with waterless Kalling's reagent (100 mL hydrochloric acid, 100 mL ethanol, 5 mg cupric chloride) to expose the grain boundaries and reveal the microstructure of the sample. Optical microscopy was performed using a Zeiss Axiotech optical microscope to examine the microstructure of samples.

Certain samples were selected to undergo scanning electron microscope (SEM) imaging using Dalhousie's Hitachi S-4700 Field Emission SEM. Quantitative elemental composition was performed using energy dispersive spectroscopy (EDS). When using EDS an accelerating voltage of 20 kV, and emission current of 15 mA were used. Working distance was set to 12 mm according to equipment standards.

4.5 Mechanical Testing

The goal of TLP bonding is to create a joined component which has thermal, and mechanical properties similar to that of the BM. Thermal analysis of the TLP bonding process was used to assess the thermal properties (primarily melting point) of the bonded component. Because of the many factors associated with the design of brazed components, testing and assessing the mechanical properties is an important aspect of the

design process. Ideally, the testing process would emulate the service conditions but in most cases this is not possible [7].

In this work, mechanical testing consisted of shear testing of brazed single lap joints following AWS standard. The strength and failure mode of TLP bonded IN625 was examined in Chapter 6. A detailed introduction to the testing method and literature review of previous testing work is presented along with failure analysis.

4.6 Thermo-Calc software

Thermo-Calc [45] is a thermodynamic modeling software which uses CALPHAD (CALculation of PHAse Diagrams) methods and a thermodynamic database to model alloy systems. In this work, Thermo-Calc was used along with database TCNI8: Ni-based Superalloys database to produce a ternary phase diagram of the Ni-Cu-Mn system, and calculate the solidus and liquidus temperatures of various alloy compositions.

To determine the phases present up to and at brazing temperature, a single point equilibrium calculation was performed. NiCuMn is a solid solution FCC γ-Ni phase. Therefore, at the brazing temperature of 1050 °C, the only phases that could be present are FCC γ-Ni and liquid. A single point equilibrium calculation for the FM alloy at 1050 °C shows that only liquid will be present meaning that the liquidus temperature is below 1050 °C.

To calculate the T_{sol} and T_{liq} of a certain composition, a single point equilibrium calculation was performed with a fixed molar fraction of either FCC γ-Ni or liquid phase and setting T (temperature) as a variable. Because there are only two possible phases (solid and liquid) near the brazing temperature, all other phases were rejected to ensure they were not considered in the solidus or liquidus calculations. In this way, fixing the

molar fraction of the liquid to 0 mol will calculate the solidus temperature and fixing the FCC solid phase to 0 mol will calculate the liquidus temperature of the composition in question.

An important aspect of Thermo-Calc is that equilibrium conditions are assumed and a thermodynamic database, only, is considered. In practice, the brazing process is not at equilibrium. In literature, Thermo-Calc is often used, assuming equilibrium conditions, for various calculations. Pouranvari et al. [52] used Thermo-Calc to calculate a IN718-boron quasi-binary phase diagram as applied to TLPB. Wieczerzak et al [53] calculated a quasi-binary phase diagram in development of Fe-Cr-Ni-Mo-C alloys and compared phase transformation temperatures calculated and measured by DSC.

The equilibrium conditions assumed by Thermo-Calc is a drawback to the methodology, but it is a necessary and viable simplification of the brazing process as it applies to this work. The accuracy and effectiveness of Thermo-Calc as it pertains to the complex IN625/Ni-Cu-Mn system will be assessed by comparing solidus and liquidus temperatures as measured by DSC to calculated values.

Chapter 5 Results and Discussion

5.1 Filler metal characterization

Each braze filler metal mixture was heated to 1050 °C at 20 K min^{-1} and held isothermal for 30 minutes in the DSC to determine the melting and solidification behaviour. Figure 5.1 presents the DSC results for the heating segment, showing the melting range for each of the filler metals. The melting event for the base Ni10 braze has the sharpest melting peak, ranging from 903 to 931 °C, due to the master alloy nature of the powder. As the nickel content is increased by mixing pure Ni powder with Ni10 MA powder, the temperature range of melting increases accordingly. The end temperatures of the melting peaks (i.e. 931, 976 and 1034 °C) measured from Figure 5.1 are consistent with the theoretical phase diagram liquidus temperatures depicted in the ternary phase diagram shown in Section 2.3.2 Figure 2.8. Furthermore, the melting range is broadened and separates into two endothermic events, a small initial melting event which onsets near the solidus temperature of the Ni10 (903°C), and a larger melting peak shifted to higher temperatures as the Ni content increases.

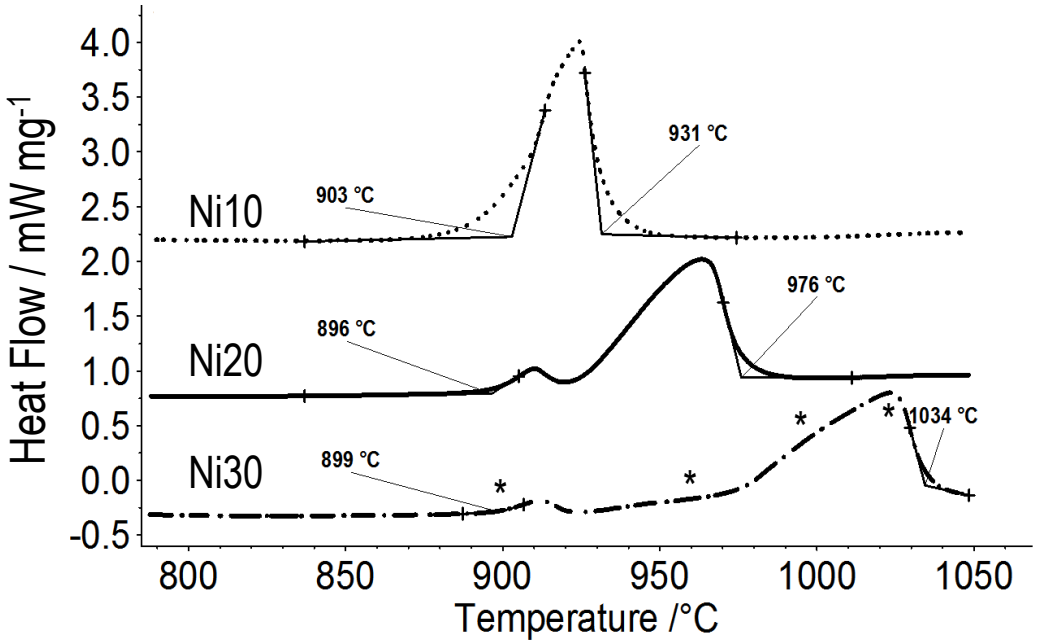

Figure 5.1 – DSC results of heating segment of Ni10, Ni20, Ni30 indicating melting endotherms of the braze filler metals. The symbols (*) indicate additional interrupted tests for the Ni30 filler metal.

When the sample is heated to 1050°C, cooled to room temperature and subsequently reheated to 1050°C the second heating DSC trace is simplified, as shown in Figure 5.2. The second heating, (in which the sample begins as a consolidated solid sphere) shows that only one melting peak is present with a solidus of 991°C and liquidus of 1041°C. The initial melting peak at 898°C, attributed to melting of Ni10 particles, is not present as these particles have fully melted and increased in Ni content up to 30 wt%. These DSC results indicate that alloying between the Ni10 braze powder and added Ni powder has occurred to a significant extent during initial heating.

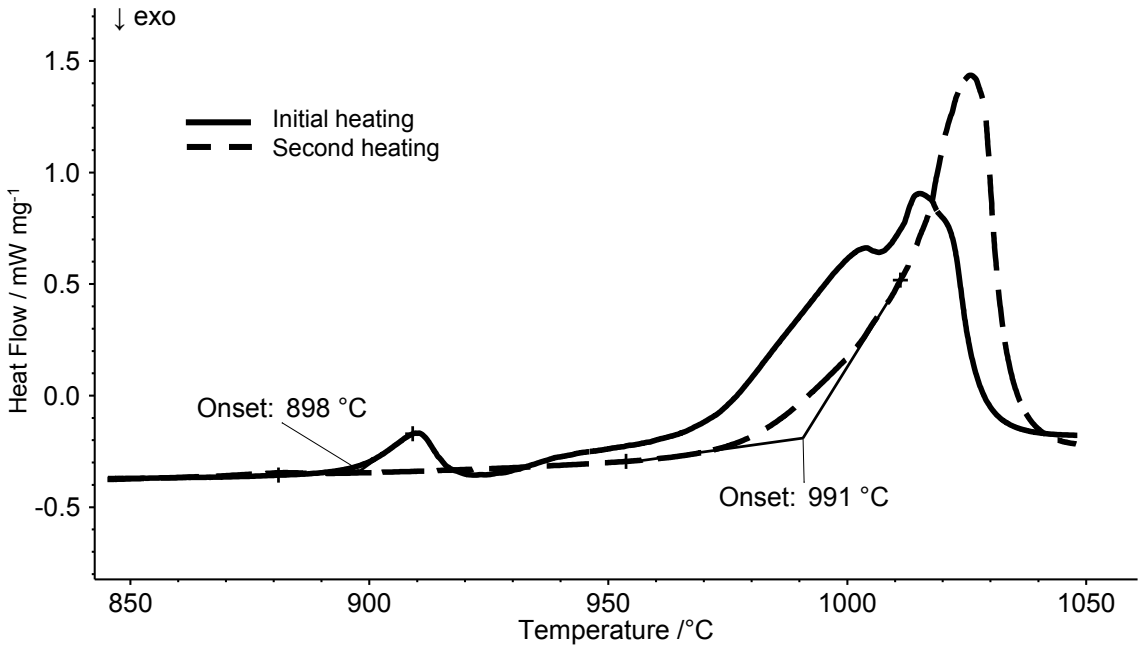

Figure 5.2 – DSC results of Ni30 filler metal (40 mg sample) on first and second heating. Ni30 powder mixture was heated to 1050 °C, cooled to room temperature, and re heated to 1050 °C for second heating.

To confirm this alloying process and better understand the two-step melting phenomenon exhibited by the higher nickel content samples, the Ni30 filler mixture was heated to temperatures of 900, 960, 995 and 1025 °C and immediately cooled so the microstructural development and in-situ alloying during heating could be observed. Figure 5.3 shows the optical microscope images of the polished DSC samples from the interrupted tests.

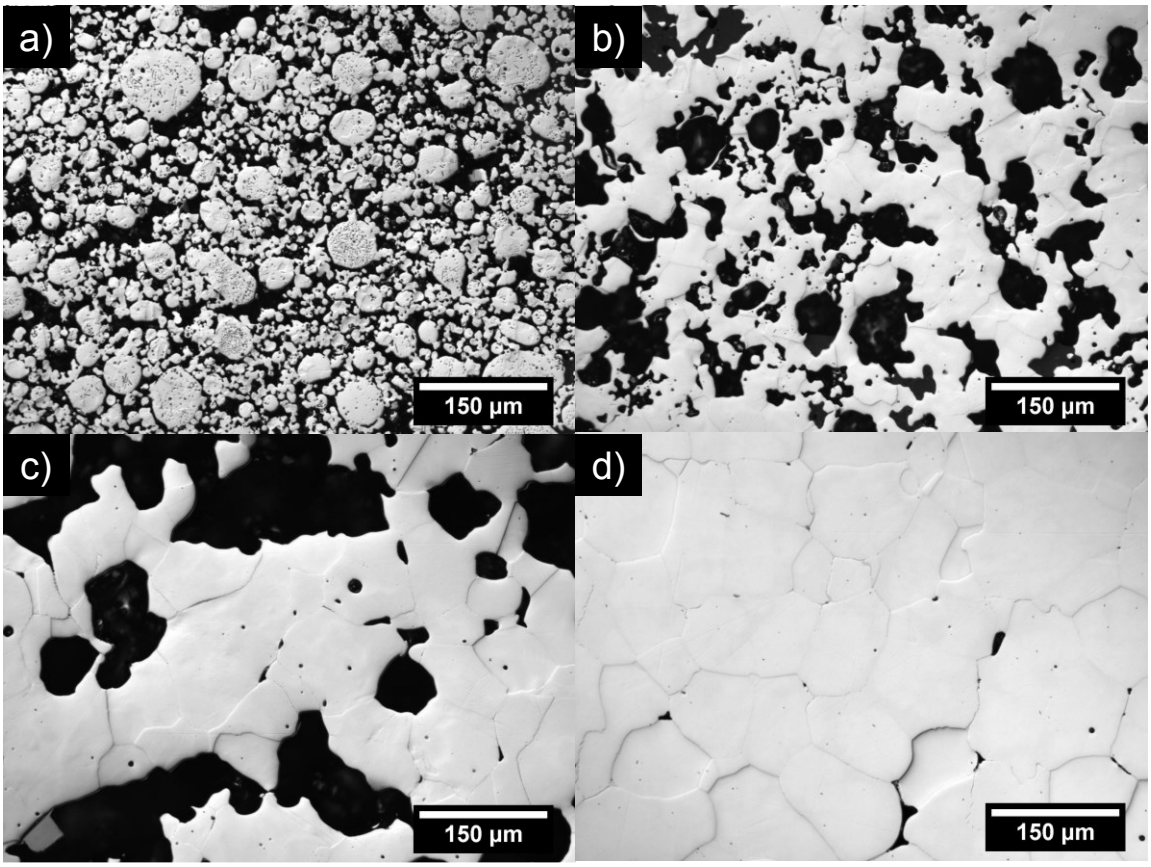

Figure 5.3 – Optical micrographs of Ni30 braze DSC samples after heating to a) 900°C, b) 960°C, c) 955°C, d) 1025°C.

When the sample cooled from 900 °C was removed from the crucible, it was a single, fused disc. This indicated the presence of interdiffusion and solid-state sintering. This is confirmed by Figure 5.3a), which illustrates many Ni particles surrounded and fused to larger Ni10 MA powder. Figure 5.4a) shows a high magnification image of the DSC experiment interrupted at 900 °C. The image confirms that the larger Ni10 master alloy braze particles are in contact with several smaller Ni particles. A neck has formed between these particles indicating solid-state sintering and interdiffusion, the extent to which was quantified using EDS. Figure 5.4b) is a graph of concentration of Ni, Cu and Mn across the interface of a Ni10 master alloy particle and Ni particle. The EDS results indicate a significant amount of diffusion between the two particles. The Ni10 particle is

enriched with Ni from the original 10 wt% to greater than 18.5 wt% 18 µm from the surface of the master alloy particle. Additional EDS analysis of the centre of several Ni10 master alloy particles confirmed that the interior of the master alloy particles reached a uniform composition of 16 wt% Ni at this stage of heating. Therefore, these particles have already obtained a composition that would have a higher melting point than 930 °C, consistent with the DSC measurements.

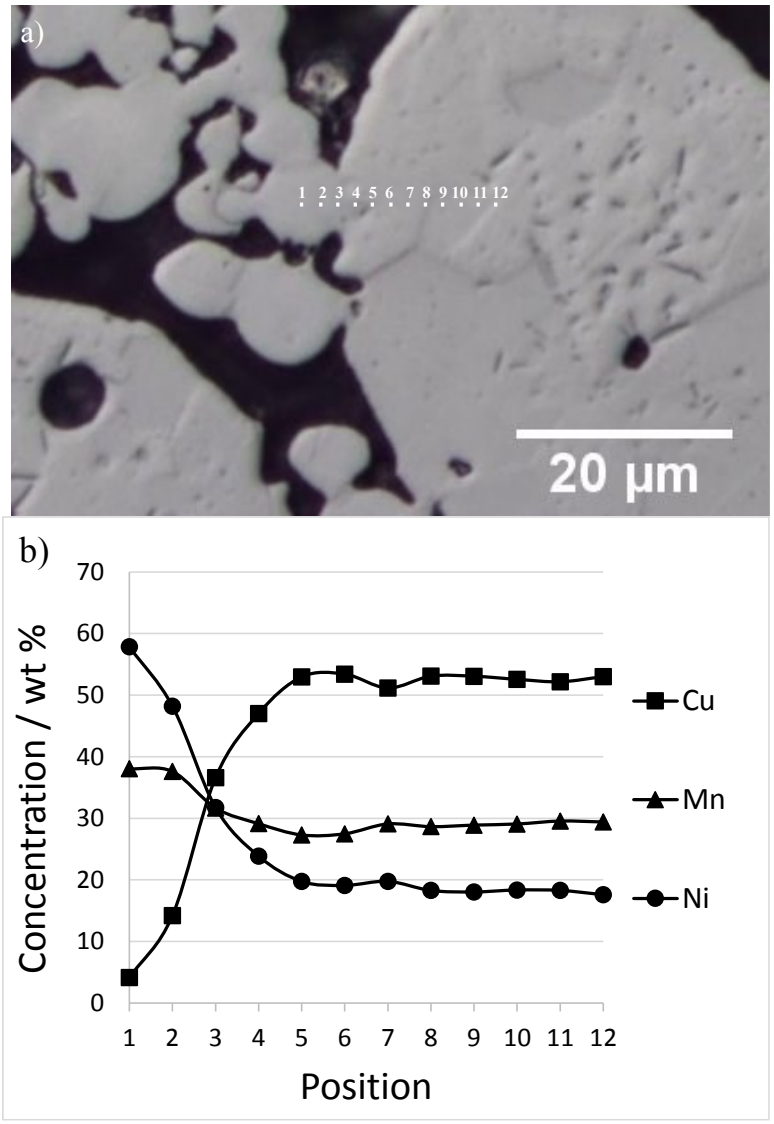

Figure 5.4 – a) Optical micrograph of Ni30 filler metal DSC sample post heating to 900°C in DSC indicating position of EDS analysis and b) graph of concentrations of Cu, Mn, and Ni vs position along the necking particles.

The original pure Ni particles are also now enriched with some Cu but mostly Mn, nearly 40 wt% Mn as measured from EDS. Per the binary Ni-Mn phase diagram presented by Laux et al [49], Mn acts as a MPD, such that the liquidus for a 60 wt% Ni-40 wt% Mn alloy would decrease to 1020 °C. Thus, the diffusion of Ni into the Ni10 master alloy particles and Mn diffusion into the pure Ni particles in the solid state, both would promote melt formation in the range of 970 to 1020 °C. This is consistent with the DSC results.

As in the Ni30 sample heated to 900 °C, the samples heated to 960 and 995 °C appeared as single fused solid discs in the shape of the crucible bottom after cooling. Conversely, samples heated to 1025 and 1050 °C underwent significant shape change and formed a consolidated ball. Figure 5.3b), c), and d) illustrate the microstructures of Ni30 powder mixtures heated to the peak temperatures of 960, 995 and 1025 °C. At 960 °C, enough melting has occurred to remove most of the discrete, individual master alloy particles thus producing a network of consolidated alloy regions. Some isolated Ni rich solid-state sintered particle clusters still exist at this temperature. Large scale porosity has developed due to particle rearrangement and liquid redistribution in the semi-solid mixture. Further heating to 995 °C creates a continuous network of locally consolidated alloy regions and a removal of solid-state sintered Ni rich networks. Large scale pores still exist due to the persistence of a solid skeleton under this condition of limited melting. Heating to 1025 °C, results in a consolidated braze of near full density with a homogeneous microstructure. Samples cooled from 1050 °C exhibited microstructures like the sample heated to 1025 °C.

These interrupted braze experiments confirm that diffusion and alloying between the pure Ni particles and Ni10 master alloy powder is rapid and occurs during the heating stage prior to achieving the braze temperature of 1050 °C. A completely melted filler metal at 1050 °C is achieved for all three compositions.

Etching the polished Ni10 and Ni30 filler metal samples heated to 1050 °C with waterless Kalling's reagent revealed a largely solid solution matrix (denoted M), with darkly etched segregated regions (denoted S) concentrated at and around the grain boundaries. The etched microstructure of Ni30 filler metal is shown in Figure 5.5. Average values of EDS point scans (minimum of three points per region) of the noted major regions/phases for Ni10 and Ni30 filler metals are shown in Table 5.1. The bulk composition noted in Table 5.1 was determined by EDS analysis of large areas (450 x 350 μm) in two locations within the samples. The bulk composition of Ni10 and Ni30 were found to be very similar to that of nominal powder composition. Small amounts of Fe, found only in the Ni30 sample, can be attributed to minor Fe content in the pure Ni powder. Comparing the S region and matrix shows an increase in Cu content and decrease in Ni in the S region while Mn stays consistent in all regions. In some areas a light (L) region was located along the grain boundaries within the S region. Elemental analysis of L locations using EDS showed a composition very similar to the S region with increased Cu and Mn content. It was therefore determined to be a small portion of the S region.

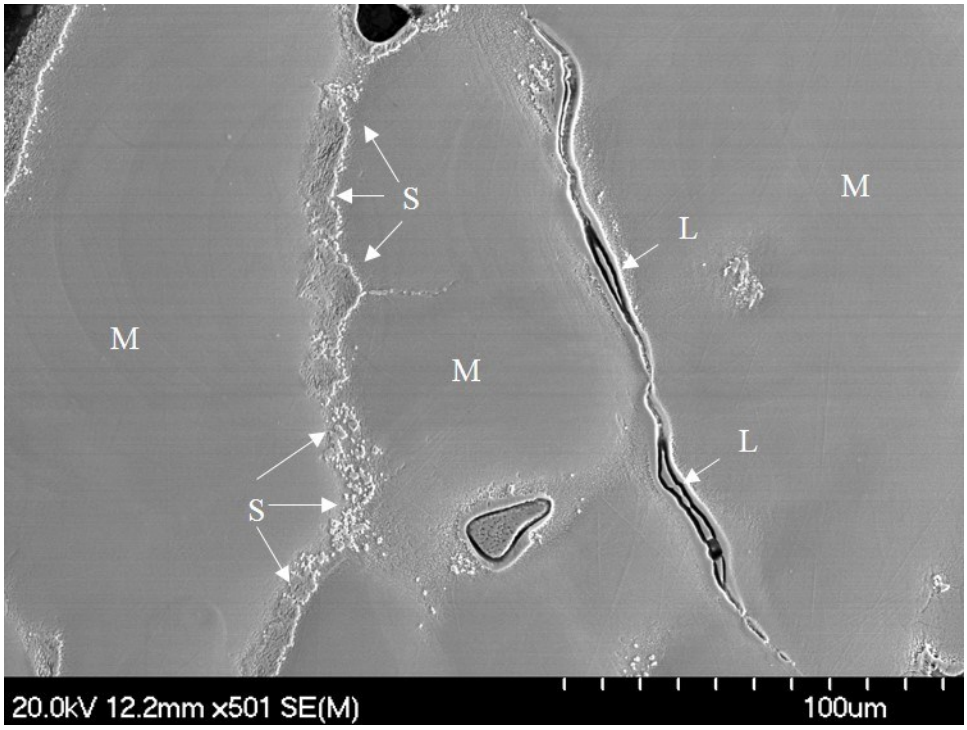

Figure 5.5 – SEM micrograph of Ni30 filler metal sample heated to 1050°C and cooled in DSC, etched with waterless Kalling's reagent. Major regions are denoted as segregated region (S), and matrix (M), and light oblong region (L).

Table 5.1 – EDS composition of main regions located in Ni10 and Ni30 filler metal samples heated to 1050°C. S region is the segregated region shown in Figure 5.5.

Region	Filler metal	Mn	Fe	Ni	Cu
Bulk	Ni10	36.7	0.0	9.7	53.5
	Ni30	29.3	0.2	28.4	42.0
Matrix	Ni10	35.9	0.0	9.8	54.2
	Ni30	28.7	0.3	32.2	38.8
S	Ni10	28.4	0.0	8.4	63.2
	Ni30	28.4	0.3	25.0	46.3

The ternary diagrams of projected solidus and liquidus for a Ni-Cu-Mn system were generated using Thermo-Calc software [45] TCNi database version 9 to determine the theoretical melting range of the bulk composition of Ni30, as well as the matrix, and S region. Figure 5.6 shows the generated ternary diagrams and plots the bulk

compositions of Ni10, Ni20, and Ni30 as well as regions (M, and S) for the Ni30 filler metal sample. As indicated previously, the liquidus temperature of Ni 10, Ni20 and Ni30 determined by DSC are approximately 931, 976 and 1040°C respectively. This agrees very well with the liquidus predictions in Figure 5.6b) for the bulk composition of these alloys (i.e. data points +, ∗ and ×). The calculated solidus temperatures of Ni10, 20, and 30 (shown in Figure 5.6b) do not agree with experimental data as well as the liquidus temperatures. Calculated solidus temperatures for Ni10, 20 and 30 are 923, 977, and 1015 °C respectively while experimental DSC results determined a solidus of 895, 940 and 991°C. Thus, the solidus temperature of the bulk composition of each filler metal is overestimated by Thermo-Calc by 25 to 37 °C. This can be explained by the microsegregated regions S noted in Figure 5.5. The copper rich S region in the solidified Ni30 was determined to have a slightly lower calculated solidus which, while still higher than experimental results, indicates a trend in decreasing solidus temperature. Conversely, the nickel rich matrix has a liquidus temperature close to the 1050 °C braze temperature (i.e. circular data set). Actually the liquidus temperature prediction for the M region of 1060 °C is slightly high, but nonetheless close to the expected 1050 °C. These temperature and composition values of the S and M regions are what would be expected from a microsegregation process when the Ni30 braze undergoes non-equilibrium freezing. The experimental melting range is widened by effectively lowering the solidus temperature due to the copper rich S region.

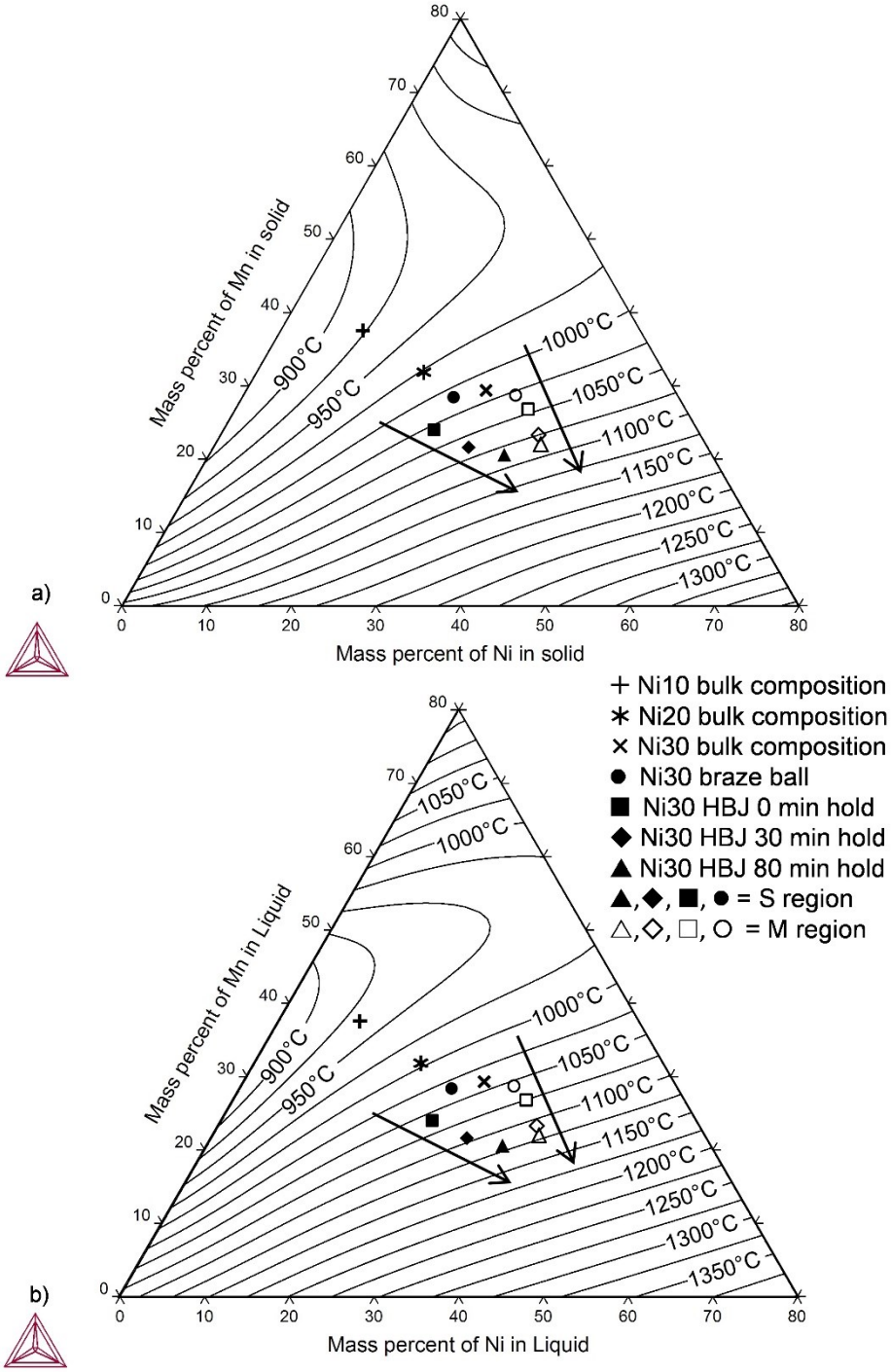

Figure 5.6 – Calculated projections of a) solidus surface and b) liquidus surface of partial Ni-Cu-Mn ternary system generated using Thermo-Calc software TCNi database version 9. Data points indicate composition of segregated region (S) and matrix region (M), of both the braze ball only (circular data) and half braze joints (square, diamond and triangular data). Arrows indicate increasing solidus and liquidus temperature of both regions as hold time increases.

5.2 Narrow gap half braze joint

With the melting characteristics of the mixed braze filler metal powders understood, a brazing process using the braze fillers was examined using DSC with the half joint setup previously shown in Figure 4.1. The heating segment DSC results of the braze half joint configuration shown in Figure 5.7 are similar to that of the filler metal alone (Figure 5.1). The half joint using Ni10 braze showed a single peak with the narrowest melting range. As the nickel content was increased to 20 wt% for Ni20, the melting phenomenon separates into two distinct events, a smaller initial melting peak followed by a second larger and broader melting peak. The DSC results for the Ni30 half joint still shows the small initial melting peak. However, the second thermal event is much broader, indicating a very gradual shift in baseline due to the melting process up to 1050 °C. The cooling segment of the DSC experiments did not show any signs of solidification of a filler metal liquid after the 30 minute hold at 1050 °C. This indicates that diffusion during heating and isothermal solidification during the hold segment lead to significant solidification of the filler metal prior to cooling. This phenomenon is explored further below.

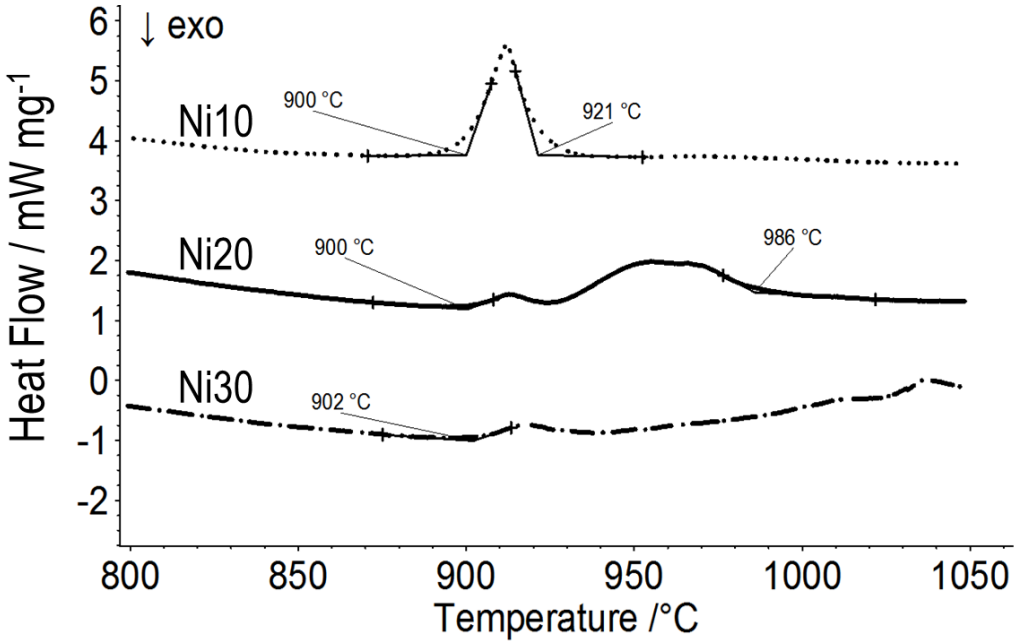

Figure 5.7 – DSC results of heating segment of narrow gap half joints using Ni10, Ni20, and Ni30 filler metals indicating melting endotherms of the braze filler metals.

The microstructural images of the Ni10 and Ni30 half braze joints after a 30 minute hold at 1050 °C are shown in Figure 5.8. Both half joints exhibited a well bonded, dense microstructure. The filler metal joint region for the Ni30 couple has a thickness of 54 µm which is close to the target thickness of 50 µm. The Ni10 half joint indicates a thicker filler/joint region of 80 µm. This is due to different levels of dissolution of the IN625 base metal, since heating to 1050 °C is 119 °C above the liquidus of Ni10 and only 10 °C above the liquidus of the Ni30 braze mixture.

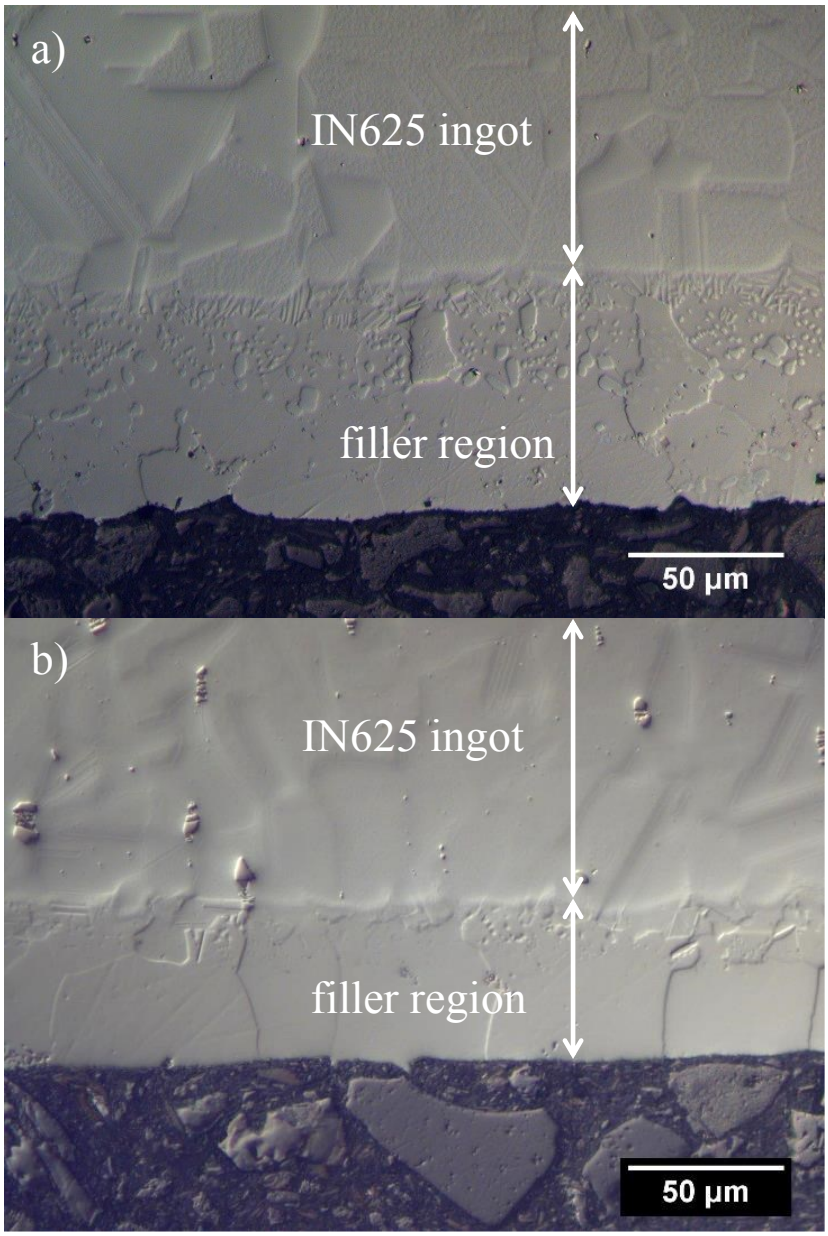

Figure 5.8 – Optical microscope image of narrow gap half braze joints held for 30 minutes at 1050°C in DSC using a) Ni10 filler metal and b) Ni30 filler metal.

Table 5.2 presents the average composition of the braze filler region of the joint determined by EDS analysis in comparison to the starting composition of the braze powder. In both, the Ni10 and Ni30 joints, the Ni content increases and the Cu and Mn content decrease. Base metal elements Cr, Mo, Fe and Nb were also detected in the braze filler region. These changing compositions are clear evidence for dissolution of the base

metal. The higher concentration of Ni, Cr, Mo, Fe and Nb in the braze portion of the half joint made with Ni10 is evidence of the increased dissolution using this braze filler composition due to its lower liquidus temperature.

Table 5.2 – Compositions of braze joint in narrow gap half joints after holding at 1050 °C for 30 minutes.

	Composition / wt%						
Alloy	Cr	Mn	Fe	Ni	Cu	Nb	Mo
Ni10 HBJ, after brazing	7.6	19.5	4.5	40.1	24.1	1.5	2.7
Ni30 HBJ, after brazing	2.0	24.2	1.6	39.3	32.3	0.2	0.4

The distribution of increased concentrations of Cr, Mo and Nb on the Ni10 joint microstructure is illustrated by the SEM-EDS mapping graphed in Figure 5.9. Two types of second phase particles are identified in the filler region as Cr-Mo and Cr-Mn-Mo rich solid solution phases.

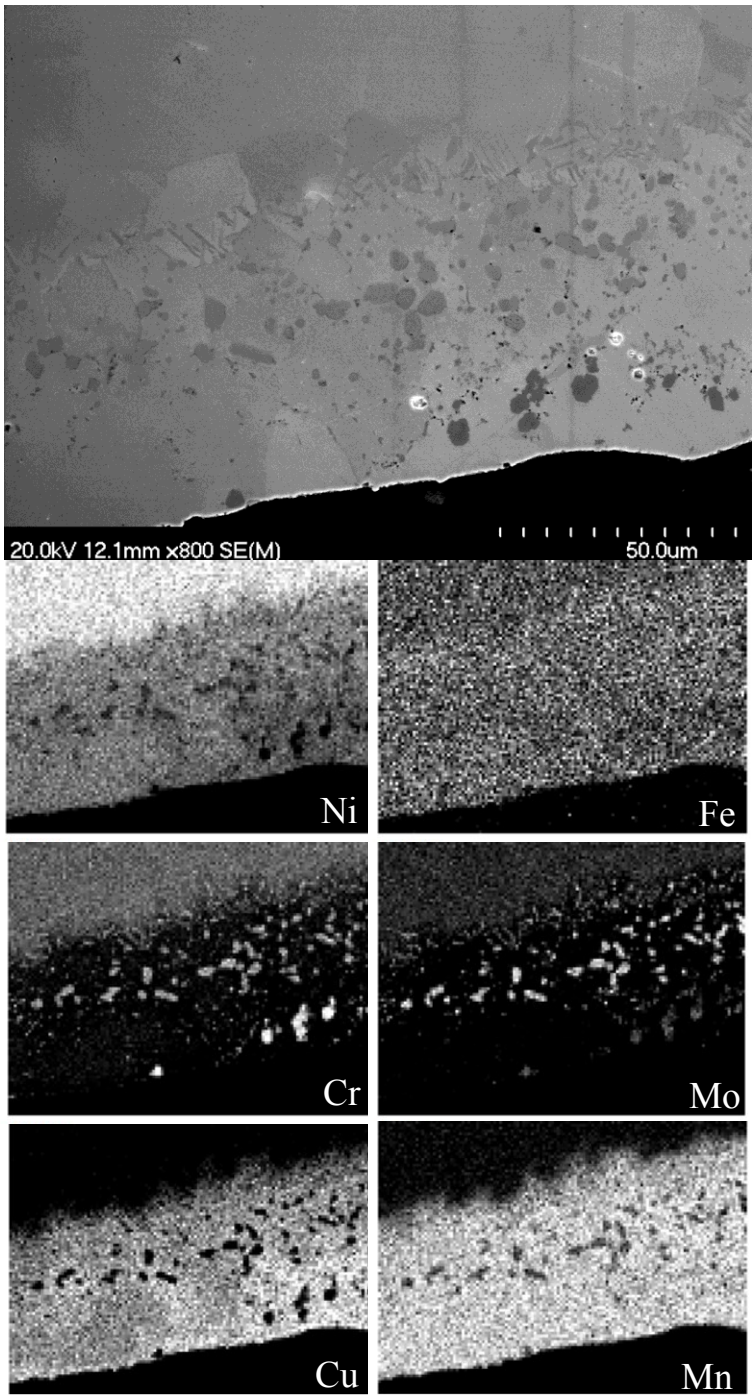

Figure 5.9 – SEM micrograph of Ni10 half braze joint held for 30 minutes at 1050°C and corresponding EDS elemental mapping.

Since the Ni30 half braze joint displayed largely single phase microstructure in the filler region of the joint and has a liquidus just under 1050 °C, it was chosen for further study with respect to isothermal solidification analysis. Half braze joints using

the Ni30 filler metal were heated in the DSC at a brazing temperature of 1050 °C and a heating rate of 20 K min^{-1} and were held at 1050 °C for varying amounts of time: 0, 30, 60, 80, and 180 minutes.

Interdiffusion during IS was measured through SEM-EDS spot analysis across the base/filler metal interface for Ni30 samples held at 1050 °C for 0 and 180 minutes (see Figure 5.10 for EDS results.). The compositional profile changes relatively sharply at the original base/filler interface for the 0 minute hold sample, with an interdiffusion zone of changing composition approximately 30 μm wide. The composition within the base metal is consistent with the composition of IN625. The interdiffusion zone increases to approximately 70 μm in width after 180 minutes at 1050 °C due to increased diffusion between the filler metal and the base metal. The uniform composition in the filler region away from the interface changes slightly after 180 minutes as can be seen from comparing Figure 5.10a) and b). There is an increase in Ni, Cr, Mo and Nb content and decrease in Cu and Mn content.

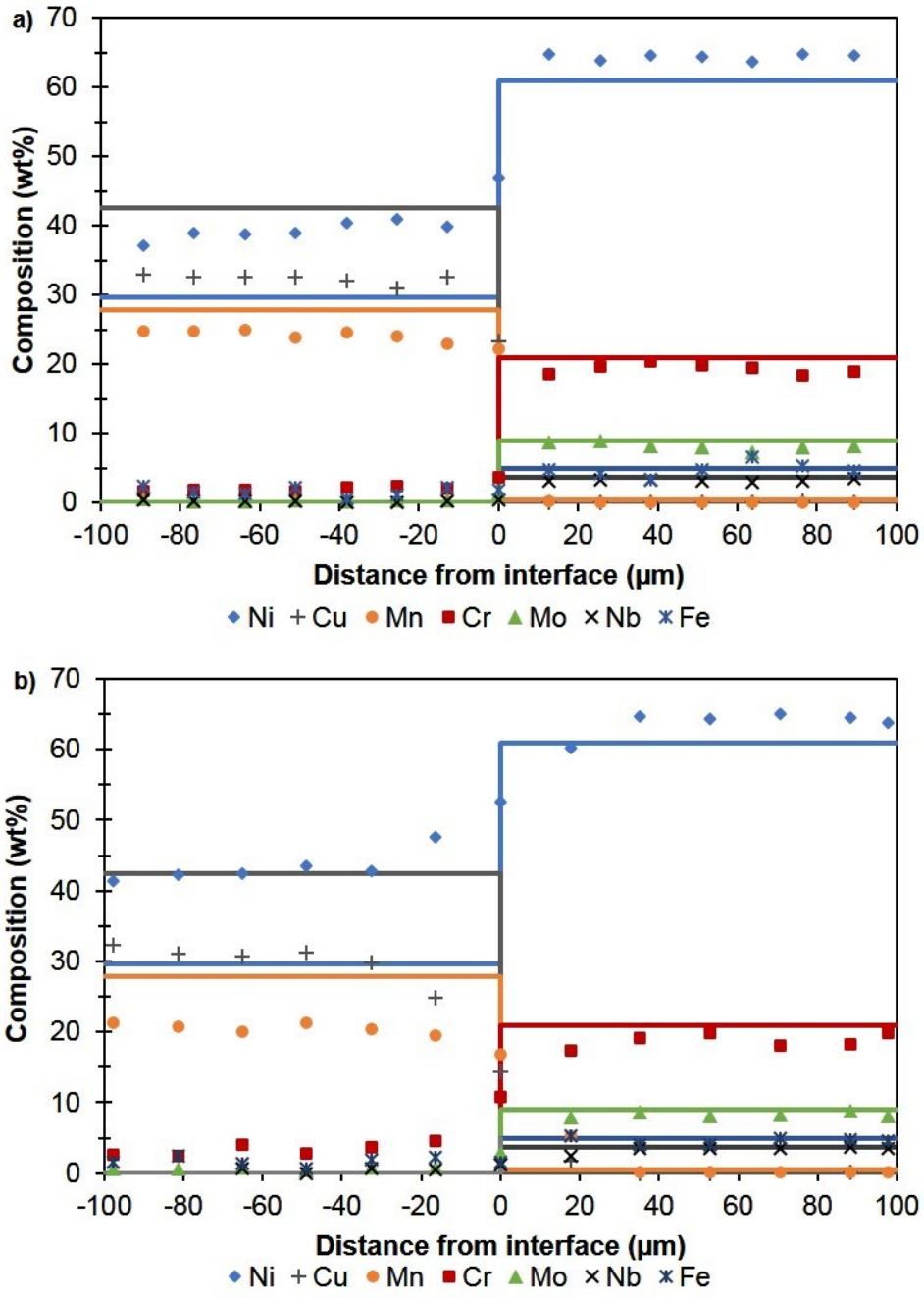

Figure 5.10 – EDS point analysis across the half braze joints of Ni30 samples held at 1050°C for a) 0 minutes, and b) 180 minutes.

Closer examination of the brazed region microstructure was performed on polished and etched Ni30 IN625 braze joints heated to 1050°C and held for 0, 30, and 80 minutes. Upon etching with waterless Kalling's reagent, a more complicated microstructure emerged showing a distinct darkly etched segregated region (S) and an

underlying matrix (M) similar to the Ni30 filler metal microstructure shown in Figure 5.5. The distinction of these two regions of the brazed joint in all three samples are shown in Figure 5.11. The S region was most concentrated at the "bottom" of the braze joint, farthest away from the filler/base metal interface, and along grain boundaries. At 0 min hold time (Figure 5.11a) the S region comprised a significant area of the brazed region, but this area decreased significantly in the 30 min hold time sample (Figure 5.11b). At 80 minute hold time, Figure 5.11c), the S region was found in small amounts along the grain boundaries and the "bottom" of the sample while the vast majority of brazed region was the single phase matrix.

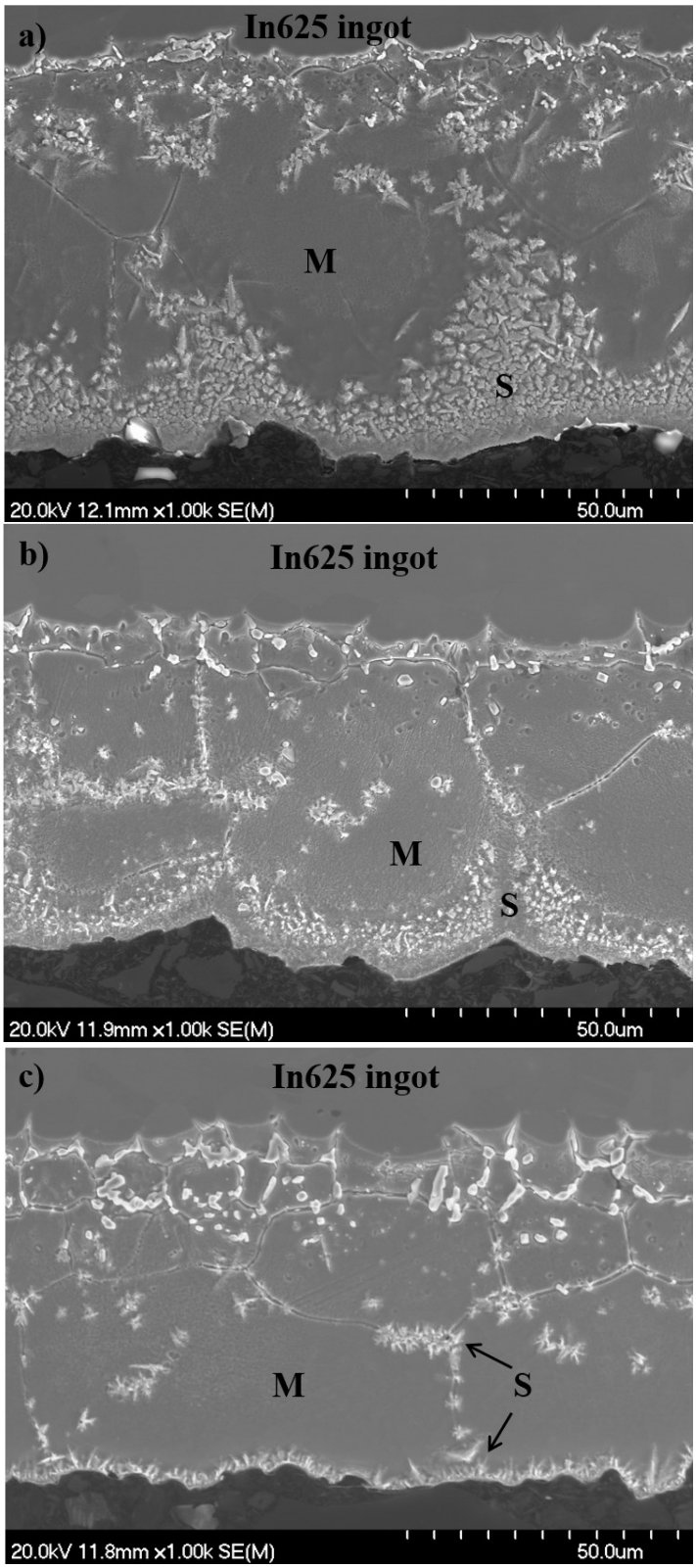

Figure 5.11 – SEM micrographs of Ni30 narrow gap half braze joints held at 1050 °C for a) 0 min b) 30 min and c) 80 min. M denotes matrix of brazed region, S denotes segregated region.

EDS spot scans were performed in four positions of each region (M and S) in two locations on the half braze joint samples and results are shown in Table 5.3. Elemental analysis confirmed that the composition of the S region consists of a higher amount of Cu, and lower amounts of Ni and Mn than the matrix for all three hold times. The trend of Cu segregation to the grain boundaries is expected as this was first shown to occur in the Ni10, and Ni30 filler metal samples (Table 5.1). Mn is well distributed throughout both regions with a slightly higher concentration in the matrix. Base metal elements Cr, Fe, and Mo were also present in both the M and S regions with Cr in highest concentrations (1 to 3.4 wt%).

Table 5.3 – EDS compositions of phases identified in brazed region of Ni30 narrow gap half joints brazed at 1050°C for various hold times. Microstructure of segregated region (S) and matrix shown in Figure 5.11.

Phase	Hold Time / minute	Cr	Mn	Fe	Ni	Cu	Nb	Mo
S	0	1.0	24.0	0.3	24.9	49.6	0.1	0.2
	30	2.3	21.6	0.5	30.2	45.0	0.0	0.4
	80	3.0	20.6	0.7	34.9	40.1	0.0	0.6
Matrix	0	1.8	26.8	0.5	34.6	35.9	0.0	0.3
	30	3.4	23.3	0.8	37.6	34.2	0.0	0.7
	80	3.4	22.0	0.7	38.5	34.7	0.0	0.6

As hold time increases, the S region decreases in Cu content from 50 to 40 wt%, and consequently increases in Ni from 25 to 35 wt% and decreases in Mn from 24 to 20 wt%. The matrix has a less drastic change in composition as hold time increases. In general, the composition of the S region approaches that of the matrix as hold time increases. This indicates that increased hold time allows for more interdiffusion of elements in the brazed region. The overall increase in Ni content in both phases with

increasing hold time also indicates that the base metal is enriching the brazed region with Ni and increasing the melting temperature of the brazed region.

This composition trend due to increasing hold time is best shown by plotting the composition of all phases on to the Ni-Cu-Mn projected liquidus and solidus diagrams of Figure 5.6. Because the half braze joint compositions contain trace amounts of base metal elements, the half braze joint compositions plotted in Figure 5.6 have been altered to only include Ni, Cu, and Mn. This is a simplification of the system, but since Ni, Cu, and Mn comprise a minimum of 95.1 wt%, the simplification will not drastically alter the main findings. Furthermore, the ternary diagrams will be used to show the general trends in melting range due to composition change rather than to determine definite liquidus temperatures for regions of the brazed joint.

In general, Figure 5.6 shows that the solidus and liquidus temperatures of the brazed region increase with hold time, and the S region and matrix compositions tend to converge as hold time is increased (in direction of arrows). This trend also translates to the converging of solidus and liquidus temperatures for the S region and matrix. At 0 minute hold time, the S region is found to have a liquidus temperature approximately 18 °C lower than the matrix. At 30 min hold time, the liquidus temperature difference decreases to 12 °C, and at 80 minute hold time there is no discernible difference in liquidus temperature for the S region and matrix. This trend is also observed in calculated solidus temperatures.

The calculated solidus temperatures of Ni10, 20 and 30, were determined to be consistently overestimated by 27 to 36 °C. Because the conditions (heating rate, gas flow rate) of the samples in this work were kept constant (with the exception of sample mass)

it can be assumed that this overestimation trend will continue with half braze joint samples. With this consideration, the solidus and liquidus temperatures of each sample can indicate, qualitatively, whether there was liquid phase remaining prior to cooling from the braze temperature of 1050 °C. Figure 5.6 indicates that the 0 minute hold half braze joint would have liquid present on cooling (i.e. a solidus temperature less than 1050 °C). The S region of 30 minute hold half braze joint has a solidus close to 1050 °C indicating that liquid is likely present on cooling but to a lesser extent than the 0 minute hold sample. The S region is still copper rich at 80 minute hold time but has the same solidus and liquidus temperature as the matrix. Figure 5.6 indicates that both regions have solidus and liquidus temperatures above 1050 °C, indicating full isothermal solidification was achieved. The presence of a diffusionally affected zone (DAZ) in the 0 minute hold HBJ, while small, is evidence of alloying and diffusion between the base metal and filler metal prior to 1050 °C. With increasing hold time, the DAZ increases in thickness and becomes a more defined region. The developed DAZ of 80 minute hold sample is shown in Figure 5.12.

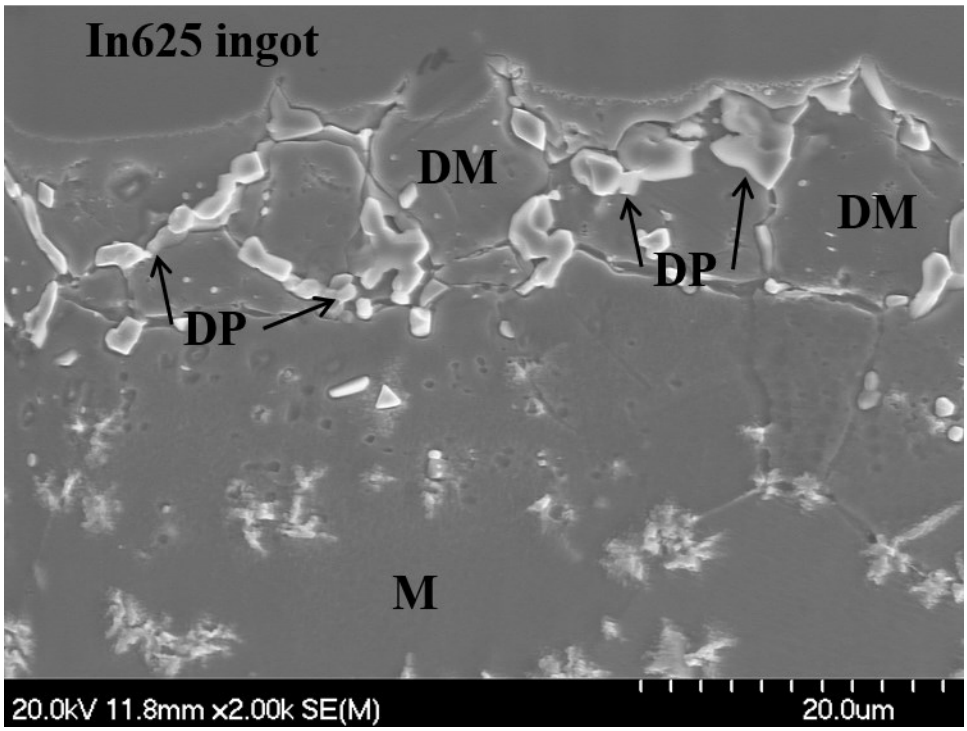

Figure 5.12 – High magnification SEM micrograph of DAZ region of Ni30 HBJ 80 minute hold. DP denotes DAZ precipitates, DM denotes matrix of DAZ, and M denotes matrix of braze joint.

The DAZ is composed of small oblong precipitates (3-5 μm in length), collected on grain boundaries near the filler metal/base metal interface. The underlying matrix in this region has a composition distinct from that of the base metal and the brazed region. The composition of the DAZ matrix, and DAZ precipitates, in Table 5.4 shows this distinction. The DAZ precipitates have a complex composition high in Mo, Cr, Ni, and Nb. At this point, the effect of DAZ precipitates on the mechanical properties of the joint is unclear. The DAZ matrix at 0 minute hold is similar to the brazed region matrix, but as hold time increases the DAZ matrix becomes enriched with Cr, Mo, Nb, Ni, and Fe and decreases in Cu, and Mn content. This suggests that widening of the DAZ is due to interdiffusion between the ISZ and base metal made possible with longer hold time at brazing temperature.

Table 5.4 – EDS compositions of phases identified in DAZ of Ni30 half braze joints brazed at 1050°C for increasing hold time. Half joints were polished and etched with waterless Kalling's reagent. Microstructure of DAZ shown in Figure 5.12.

Phase	Hold time / min	Ti	Cr	Mn	Fe	Ni	Cu	Nb	Mo
DAZ ppt	0	0.2	22.4	5.3	1.6	20.5	2.4	7.2	40.4
	30	0.2	12.9	3.9	1.4	19.7	2.0	10.1	49.8
	80	0.2	13.7	3.3	1.6	20.3	1.7	13.0	46.1
DAZ M	0	0.0	2.8	24.8	0.7	36.9	34.1	0.1	0.6
	30	0.1	5.3	22.0	1.2	41.2	28.2	0.7	1.4
	80	0.1	9.4	18.3	2.0	47.6	17.8	1.4	3.4

5.3 Isothermal solidification characterization

To more completely characterize the process of IS and its kinetics, joints were subjected to a "remelt" test within the DSC where, after the brazing process, samples were cooled to 800 °C, and then reheated to 1200 °C to determine the melting temperature of the braze in the half joints. Figure 5.13 gives the results of the remelt DSC segments of the half gap Ni30 joints after being held at 1050 °C for five different hold times: 0, 30, 60, 120 and 180 minutes. The analysis of the remelt peaks show that as the hold time was increased, the new solidus temperature and overall melting range of the filler metal also increased. This is due to the increasing Ni and decreasing Cu and Mn content of the filler region matrix during homogenization and the decrease in amount of S region present in the joint as indicated in Figure 5.6, Figure 5.10, and Figure 5.11.

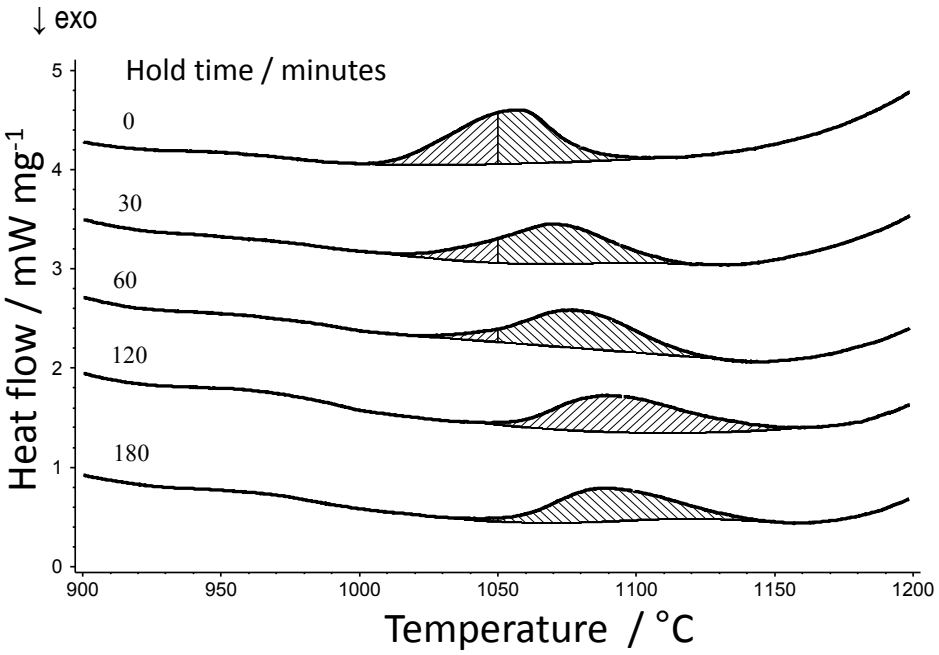

Figure 5.13 – DSC results for Ni30 half braze joints of reheat segment after increasing hold times at 1050°C and cooled to 800°C prior to reheat to 1200°C. Vertical line on individual heating segments indicated 1050 °C cut-off for area measurement.

The remelt tests also give insight into the rate of isothermal solidification and help clarify the nature of solidification. Previously, the absence of any solidification peaks on the DSC cooling trace suggested that the solidification occurs very rapidly and that no liquid remains during cooling even after no hold time at the braze temperature. However, the calculated solidus temperatures of both the S region and matrix of this sample (shown in Figure 5.6) based on EDS results are below 1050 °C. This indicates that a significant portion of the filler region would be liquid at 1050 °C and athermally solidify upon cooling. The remelt tests of Figure 5.13 agree with the calculated liquidus temperatures of Figure 5.6. Remelt of the 0 minute, and 30 minute hold samples establish liquidus temperatures (by DSC) of 1090 °C and 1118 °C respectively. The calculated liquidus temperatures based on composition of the matrix for 0 minute and 30 minute hold samples were determined to be approximately 1075 °C, and 1110 °C respectively,

showing good agreement between experimental and calculated melting ranges. The small discrepancy could be attributed to base metal elements which are not considered in the Ni-Cu-Mn liquidus diagram.

The 0, 30, and 60 minute hold time samples have remelt onset temperatures that are below 1050 °C. Therefore, if the filler metal melting range begins before 1050 °C, there must have been liquid present during the hold time at 1050 °C, that solidified athermally during cooling. EDS analysis and calculated liquidus temperatures have confirmed that the S region consistently has the lowest liquidus temperature and would, in some cases, solidify upon cooling. In contrast, the 120 and 180 minute samples have remelt onset temperatures above 1050 °C, indicating that no liquid would have been present during cooling from 1050 °C. Hence, isothermal solidification is complete between 60 and 120 minutes of hold time at the brazing temperature of 1050 °C. Microstructural examination of the 80 minute hold sample found that, while the matrix and S region had different elemental compositions, their respective calculated liquidus temperatures are equal as shown in Figure 5.6.

The IS kinetics of the braze filler can be estimated by graphing the amount of liquid that remains on reheating against the liquid duration which is defined as the time at which the temperature is above the solidus. A partial integration of the DSC melting endotherms from the solidus temperature to the peak temperature of 1050 °C was performed. The resulting enthalpy in J/g was taken as a measurement of the liquid formed below 1050 °C and is shown in Figure 5.14 for the Ni30 half braze joint. Linear regression was performed using all data points which had a measured enthalpy greater than 0 (i.e. excluding the final two data points).

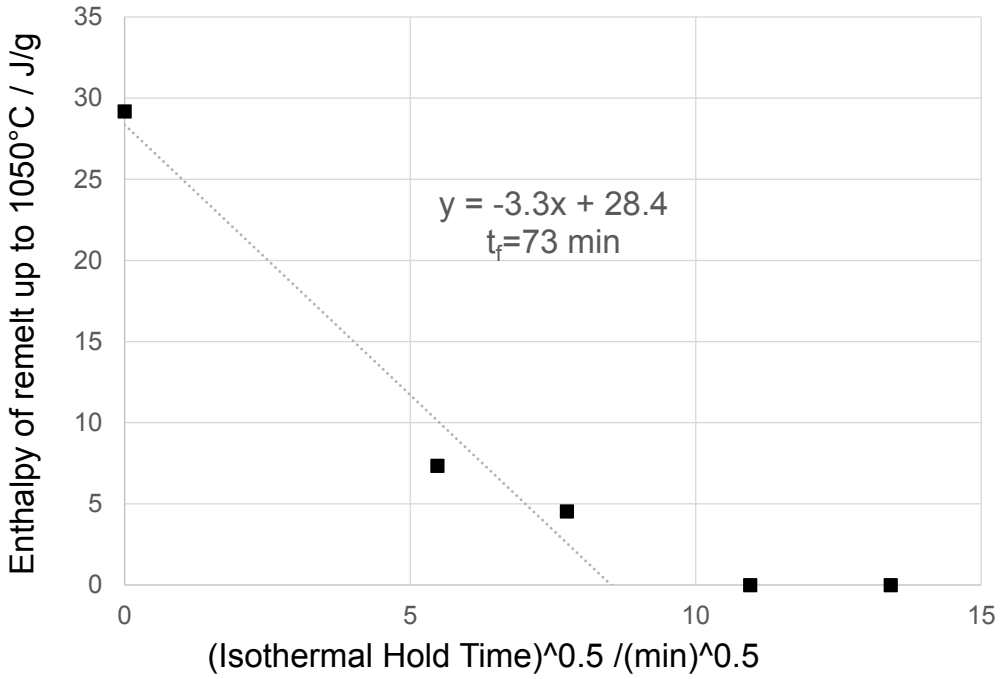

Figure 5.14 – Graph of enthalpy of remelt up to 1050°C and square root of isothermal hold time for narrow and wide gap braze joints.

The time for which the sample will have no liquid remaining, i.e. complete isothermal solidification, can be estimated from the *x*-intercept of the graph of enthalpy of remelt vs. isothermal hold time. The graph shows that the time for 100% isothermal solidification at 1050 °C is estimated to be 73 minutes for the half gap half joint. This agrees well with the previous statement that Ni30 80 minute half braze joint could have been completely isothermally solidified based on calculated solidus and liquidus temperatures (above 1050 °C) of the brazed region.

5.4 Conclusions

Braze filler metals in the Ni-Cu-Mn system were investigated to find a suitable substitute for boron containing filler metals used in aerospace brazing techniques. The melting behaviour of three potential braze filler metal alloys were examined; Ni10, Ni20, and Ni30 where the 10, 20, and 30 represents the nominal wt% of Ni in the alloy. Dense

and void free braze half joints were produced using these filler metals by brazing at 1050 °C. Good wetting of IN625 base metal was observed for all filler metal alloys.

The highest nickel content of 30 wt% produces a solid solution joint enriched with base metal elements and a copper rich segregated region determined to have a lower liquidus temperature than the joint matrix. The amount of this liquid phase decreases significantly with increasing hold time. Isothermal solidification kinetics of the Ni30 half braze joint indicated that a hold time of 73 minutes at 1050 °C will result in a fully isothermally solidified braze joint with no liquid phase present on cooling. EDS composition of half braze joint held for 80 minutes and calculated solidus and liquidus temperatures for these compositions confirmed that the brazed region would be isothermally solidified. Longer hold times show evidence of homogenization occurring and increased interdiffusion between ISZ and base metal, however even after a 180 minute hold at braze temperature (the longest hold time studied herein), there remains a large difference in composition between the filler metal and base metal.

5.5 Wide gap melting behaviour

In Section 5.1 it was shown that, on heating Ni30 mixture to the brazing temperature of 1050 °C, solid state interdiffusion between the Ni and MA particles takes place. This enriched the pure Ni particles with Cu, and Mn, MA particles then begin to melt further (shown by a small endothermic peak at 898 °C) increasing the rate of diffusion and alloying of the two particles. Regions of high Ni content diffusionally freeze after alloying and subsequently melt as temperature is increased. This continues until the Ni30 liquidus of 1040 °C after which the alloy is fully liquid.

Determination of the melting behaviour of the Ni30/IN625 HBJ primarily utilized the remelt (both high and low temperature), and cyclic thermal profiles described in Section 4.3 Figure 4.2. Half braze joints (HBJ) prepared using the isothermal hold only thermal profile were examined primarily for microstructure, and SEM/EDS analysis. The cyclic thermal profile as applied to HBJ samples allows for a significant amount of data to be collected. The extent of isothermal solidification can be tracked as time above solidus is increased. Figure 5.15 shows the melting segments of a Ni30/IN625 HBJ 22 cycle sample.

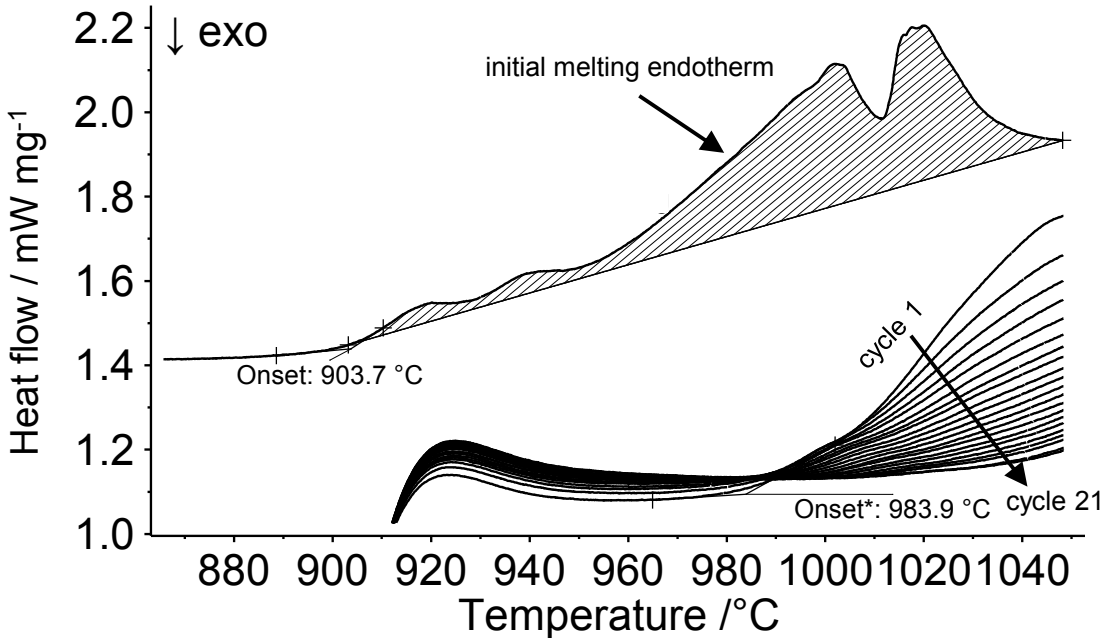

Figure 5.15 – DSC trace on melting of 22 cycle Ni30 HBJ. Onset of melting on initial heating 903.7 °C. Remelt temperature of subsequent heating cycles on heating increases to 980 to 1000 °C. Shaded region in initial melting endotherm is area included in enthalpy measurement.

The thermal profile using 22 cycles (60 minute hold per segment) has a cumulative 1393 min above solidus temperature. On initial heating, a fully resolved melting endotherm has a solidus temperature of 904 °C and liquidus of 1040 °C. The melting onset has been identified as the melting of pure NiCuMan37 particles remaining

in the powder mixture (Section 5.1). The liquidus of 1040 °C indicates that a significant amount of solid state diffusion has taken place prior to 900 °C. Evident in Figure 5.15 is the decrease in area of melting endotherm in each subsequent cycle. This proves that the amount of liquid present is decreasing as time above solidus increases.

The melting endotherm after 60 minute hold at 1050°C (i.e. cycle 1) has an increase in solidus temperature to 984 °C. As the cycle number increases, and thus the cumulative hold time at 1050 °C increases, the solidus temperature of the melting endotherm slightly increases from 984 °C to approximately 995 °C. While the shift in solidus temperature is modest, the area (enthalpy) of the melting endotherm decreases drastically.

The high temperature remelt profile gives a full view of the melting range of the brazed region after a certain hold time as shown in Figure 5.16. The high temperature remelt segment of Ni30/IN625 HBJ samples after holding at 1050 °C for increasing times are shown in Figure 5.16. As the hold time at 1050°C increases, the melting range of the brazed region becomes wider (i.e. T_{liq}-T_{sol} increases) and the enthalpy of melting prior to 1050 °C decreases. Additionally, T_{sol} increases from approximately 970 °C (0 minute hold) to 990 °C (480 min hold). This is in agreement with the features found in DSC traces using the cyclic thermal profile (Figure 5.15).

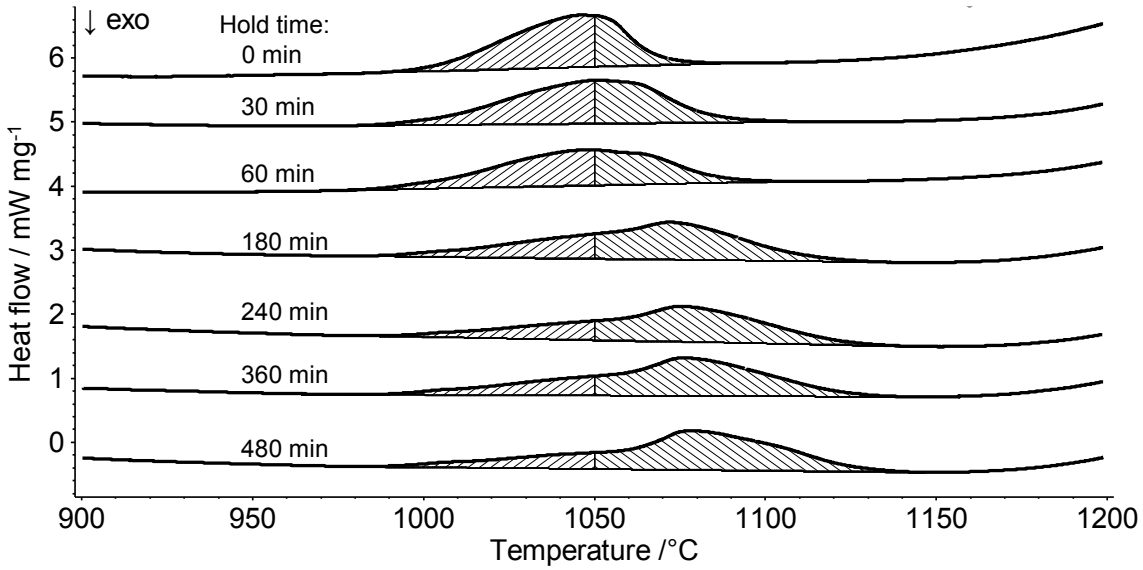

Figure 5.16 - DSC results on high temperature remelt up to 1200°C after increasing hold time (indicated on figure) at 1050 °C. Solid vertical line indicates position of brazing temperature of 1050°C.

The agreement between Figure 5.15 and Figure 5.16 is important to this work. It proves that both thermal profiles are valid and can be compared. For this reason, DSC traces using remelt, interrupted and cyclic thermal profiles will be compared in this work. Both thermal profiles resulted in an increase in T_{sol} and decrease in enthalpy as the hold time at 1050 °C is increased. These important features of the DSC trace suggest two facts about the microstructure of the brazed region:

1. The portion of the brazed region that is still liquid on cooling (i.e. the athermally solidified zone) decreases in volume with increasing time above solidus temperature. This is indicated by the decrease in enthalpy.
2. The elemental composition of the ASZ changes slightly as time above solidus temperature is increased. This is indicated by the small change in solidus temperature.

These features will be examined in detail through optical microscopy and SEM/EDS analysis.

5.6 Microstructural examination of brazed region

The microstructure of Ni30/IN625 narrow gap half braze joints was described in the earlier Section 5.2. As expected, wide gap conditions resulted in similar microstructure of the brazed region. As shown in Figure 5.17 the Ni30/IN625 wide gap HBJ samples have a segregated region (denoted S) focussed around the grain boundaries in the braze region. A diffusional affected zone (DAZ) was identified at the original solid liquid interface. The DAZ is composed of an underlying matrix (found to be of variable composition) and small precipitates distributed throughout the region. The DAZ precipitates shown are of circular and oblong shape, measured to be between 1 and 20 μm in size.

The brazed region of HBJ samples was micrographed along the entire width of the sample and images were stitched together using the built in grid-stitching function [54] in Fiji software [55] to create a composite micrograph. An example of this composite image is shown in Figure 5.18. Variance in braze joint thickness was noted in all samples. The largest variance was focussed around the perimeter of the base metal ingot. Variance throughout the interior of the brazed region can be attributed to the imperfect surface of the Al_2O_3 crucible.

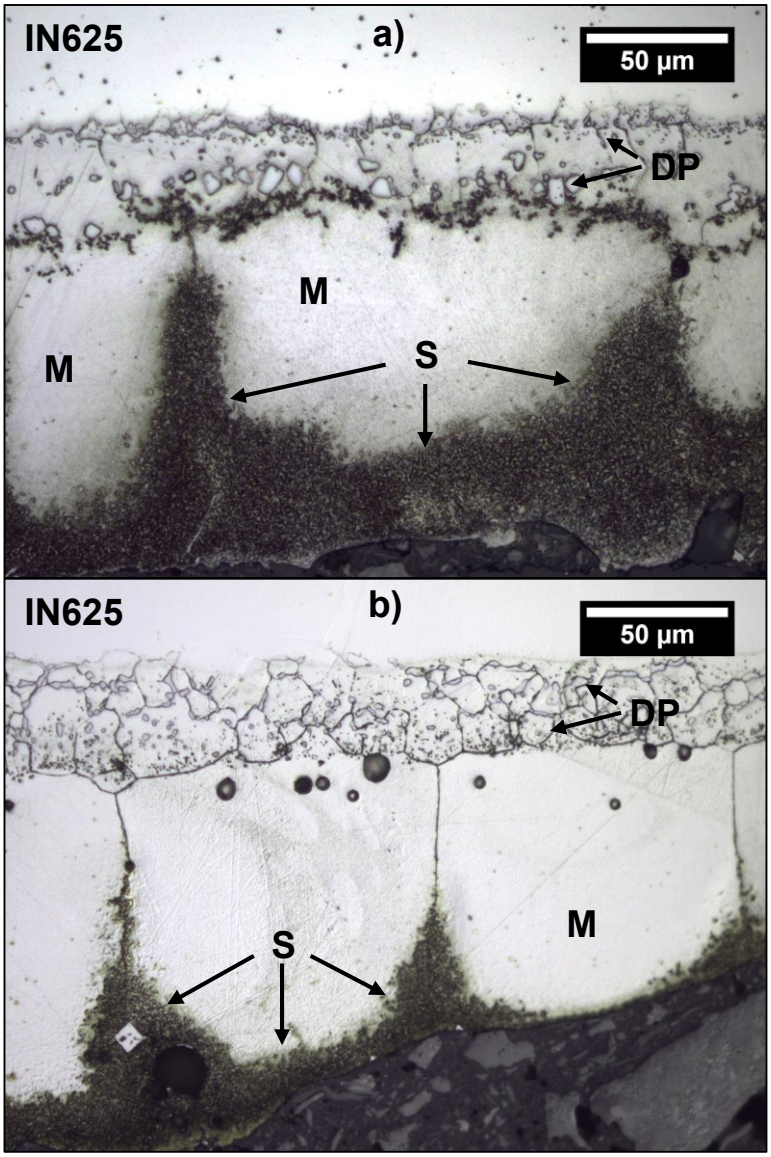

Figure 5.17 – Optical micrographs of Ni30 braze half joints etched with waterless Kalling's reagent brazed at 1050°C for a) 30 minutes b) 240 minutes. Region/phases shown are matrix (M), segregated (S), and diffusional affected zone precipitates (DP).

Figure 5.18 – Stitched composite micrograph of Ni30/IN625 wide gap half braze joint held at 1050 °C for 240 minutes. Examined braze joint width is 4.5 mm. Darkly etched region is the S region.

The average measured braze thickness data for various hold times at 1050 °C is presented in Figure 5.19 showing the variation in thickness for each sample. Over the range of hold times (30 to 1320 minutes) the measured thickness of braze joint remains relatively constant Braze joints held at 1050 °C for 30 and 60 minutes have a slightly lower range of values but, as shown in Figure 5.19 this is not a statistically significant difference. So, it can be said that there is no relationship between hold time and braze joint thickness. This is significant because it proves that isothermal solidification is not occurring by increased dissolution of the base metal but by diffusion of MPD into the base metal. If dissolution of the base metal were causing the progression of isothermal solidification, there would be a marked increase in the braze joint thickness with increase in hold time.

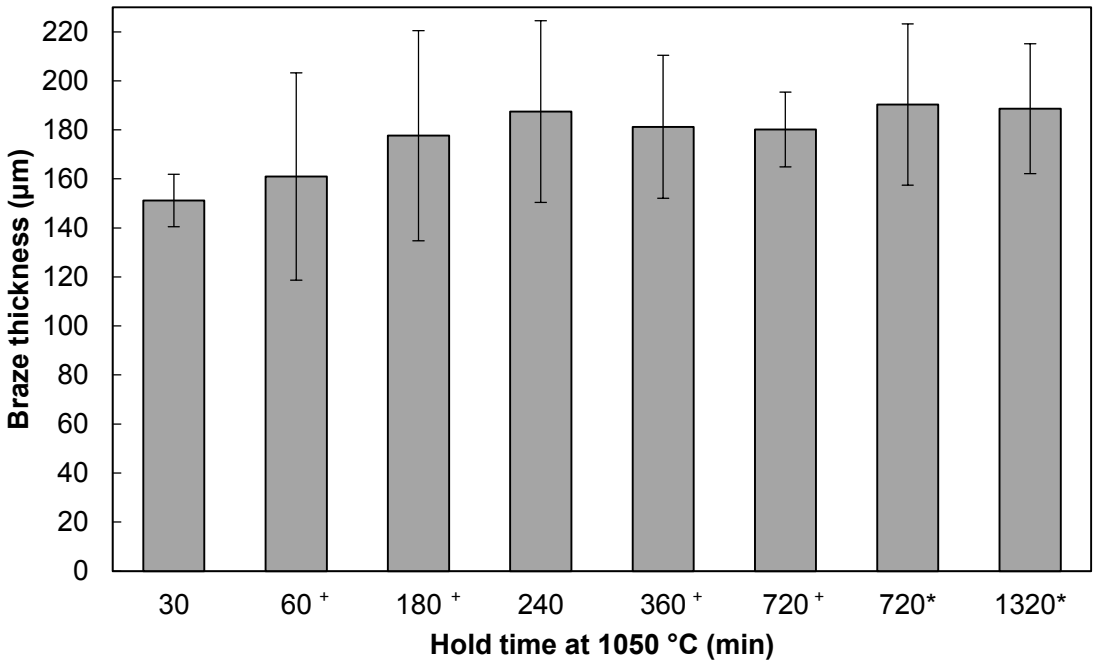

Figure 5.19 – Measured thickness of Ni30/IN625 half braze joints for various hold times. *samples brazed using cyclic thermal profile, + samples brazed using iso hold + low temperature remelt thermal profile, other samples brazed using isothermal hold thermal profile.

5.6.1 Elemental composition of brazed Ni30/IN625 brazed region

Ni30/IN625 wide gap HBJ samples were examined by EDS (energy dispersive spectroscopy) to determine the elemental composition of the S region and matrix. Table 5.5 summarizes the measured composition for HBJ samples brazed for 30, 240, 720, and 1320 minutes to track the change in composition as hold time increases. In general, with increasing hold time the braze region tends to increase in Ni content and decrease in Cu, and Mn content. The decrease in concentration of MPD elements (Cu and Mn) in the brazed region will ultimately push the melting range to higher temperatures indicating that isothermal solidification is progressing as hold time increases.

Table 5.5 – EDS measured elemental composition of matrix (M) and segregated region (S) for Ni30/In625 wide gap HBJ samples at various hold times at T_B (1050 °C).

Region	Hold time at T_B (min)	Cr	Mn	Fe	Ni	Cu	Nb	Mo
S	30+	0.9	17.2	0.1	15.9	65.9	0.0	0.0
	240+	1.1	20.8	0.1	19.3	58.5	0.0	0.1
	720*	1.6	21.4	0.4	23.7	52.9	0.0	0.0
	1320*	2.7	18.2	0.6	25.2	53.3	0.0	0.0
M	30+	2.3	24.4	0.5	31.4	40.7	0.2	0.5
	240+	2.8	23.8	0.5	32.9	39.3	0.2	0.5
	720*	3.7	22.2	0.9	37.2	36.1	0.0	0.0
	1320*	3.7	21.4	0.9	36.7	37.3	0.0	0.0

+ Samples brazed using isothermal hold thermal profile
*Samples brazed using cyclic thermal profile

The solid solution matrix of the brazed region stays relatively constant as hold time increases. There is a slight increase in Ni content, and decrease in Mn, and Cu content. Ni increases a total of 5.3 wt%, and Mn and Cu decrease by 3.0, and 3.4 wt% respectively. Considering the experimental error of EDS detection is ± 1 wt%, and standard deviation of four measurements ranges from 0.2 to 1.7 wt% these trends are minor but will have an effect on the melting range. The S region has a more significant

trend in composition change. Ni content increases by 9.3 wt%, and Cu decreases by 12.6 wt%. Mn increases by 4.2 wt% from 30 to 720 minutes and decreases by 3.2 wt% at 1320 minute hold. These trends will be examined in more detail in Section 5.6.2.

A magnified SEM micrograph of the DAZ of Ni30/IN625 HBJ is shown in Figure 5.20 and Table 5.6 presents the elemental composition of the DAZ precipitates and the DAZ matrix. The matrix of the DAZ (MD) is a solid solution FCC gamma phase typical in Ni-base superalloys [5]. The MD is similar to the matrix of the brazed region but with an increased Cr content. Because this region is diffusionally affected there is a significant amount of variation in elemental composition moving away from the initial solid-liquid interface. This region is studied in a later Section 5.6.3.

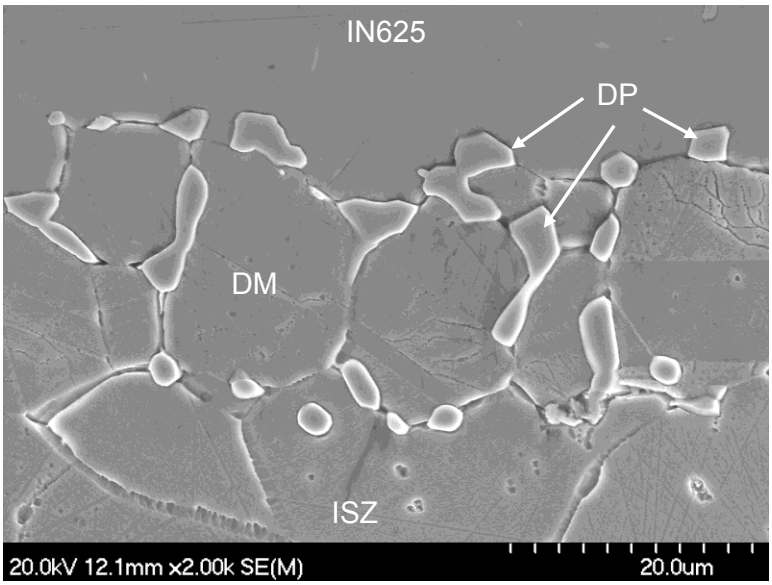

Figure 5.20 – SEM micrograph of Ni30/IN625 HBJ cyclic sample brazed for 720 minutes. DP indicates DAZ precipitates, MD is DAZ matrix, ISZ is isothermally solidified zone.

Table 5.6 – EDS measured elemental composition (wt%) of DAZ for various hold times at 1050 °C. DAZ M is the solid solution of the DAZ, DAZ ppt is the precipitate formed in the DAZ as identified in Figure 5.20.

Phase	Hold time at T_B (min)	Cr	Mn	Fe	Ni	Cu	Nb	Mo
DAZ ppt	30+	11.8	4.1	1.4	19.7	2.1	6.1	54.9
	240+	12.0	3.8	1.3	19.8	1.9	6.1	55.1
	720*	14.8	2.7	1.8	19.1	1.1	15.2	45.7
	1320*	14.4	2.8	1.8	19.4	1.0	13.2	47.4
DAZ M	30+	2.7	23.4	0.8	33.3	38.5	0.6	0.8
	240+	4.1	21.5	1.2	35.5	36.0	0.5	1.3
	720*	8.9	19.6	2.1	46.9	20.4	0.0	2.1
	1320*	6.9	20.3	1.7	43.8	26.4	0.0	0.9

+ Samples brazed using isothermal hold thermal profile
*Samples brazed using cyclic thermal profile

The small DAZ precipitates are distributed as discontinuous chains along the grain boundaries. These precipitates are found to be primarily composed of Nb, Mo, Ni, and Cr with small contributions from Mn, Fe, and Cu. The precipitates have a content of between 45 and 55 wt% Mo, significantly higher than the nominal Mo content of IN625 (9 wt%). DAZ precipitates are identified in all Ni30/IN625 HBJ samples regardless of hold time meaning that they are most likely formed rapidly on initial heating of the braze joint. The width of the DAZ, and the volume fraction of DAZ precipitates does increase with increasing hold time.

Chromium and molybdenum are both carbide-forming elements in Ni-based superalloys. In these alloys, carbides form at the grain boundaries and can form during heat treatments from 760 to 980 °C. The EDS system used does not have the capability of detecting carbon, so it is unknown if carbon is present in the DAZ. It is possible that the DAZ precipitates are carbides.

5.6.2 Determination of ASZ and ISZ

In boron containing braze systems, distinguishing between the ASZ and ISZ is straightforward microstructurally. The ASZ has a large fraction of second phase brittle borides while the ISZ is a single phase solid solution [31]. In the current boron free braze, the ASZ and ISZ are both part of the same extended single phase solid solution, albeit with varying composition. In this case, the extent of isothermal solidification and the change in melting range was determined by plotting the composition of both the S region and matrix on Ni-Cu-Mn ternary solidus and liquidus diagrams shown in Figure 5.21. The T_{sol} of the S region and T_{liq} of the matrix will encompass the entirety of the melting range. The compositions plotted in Figure 5.21 only consider the Ni-Cu-Mn content of each region and is therefore an estimation of T_{sol} and T_{liq} only. The exact T_{sol} and T_{liq} values (using full composition) of each region were determined in Thermocalc ® using a single point equilibrium calculation and are included in Appendix A. Comparing these values, it was determined that small additions of Cr and Fe did not have a significant effect on the calculated melting range. With this consideration, the trends of melting range can be determined from Figure 5.21.

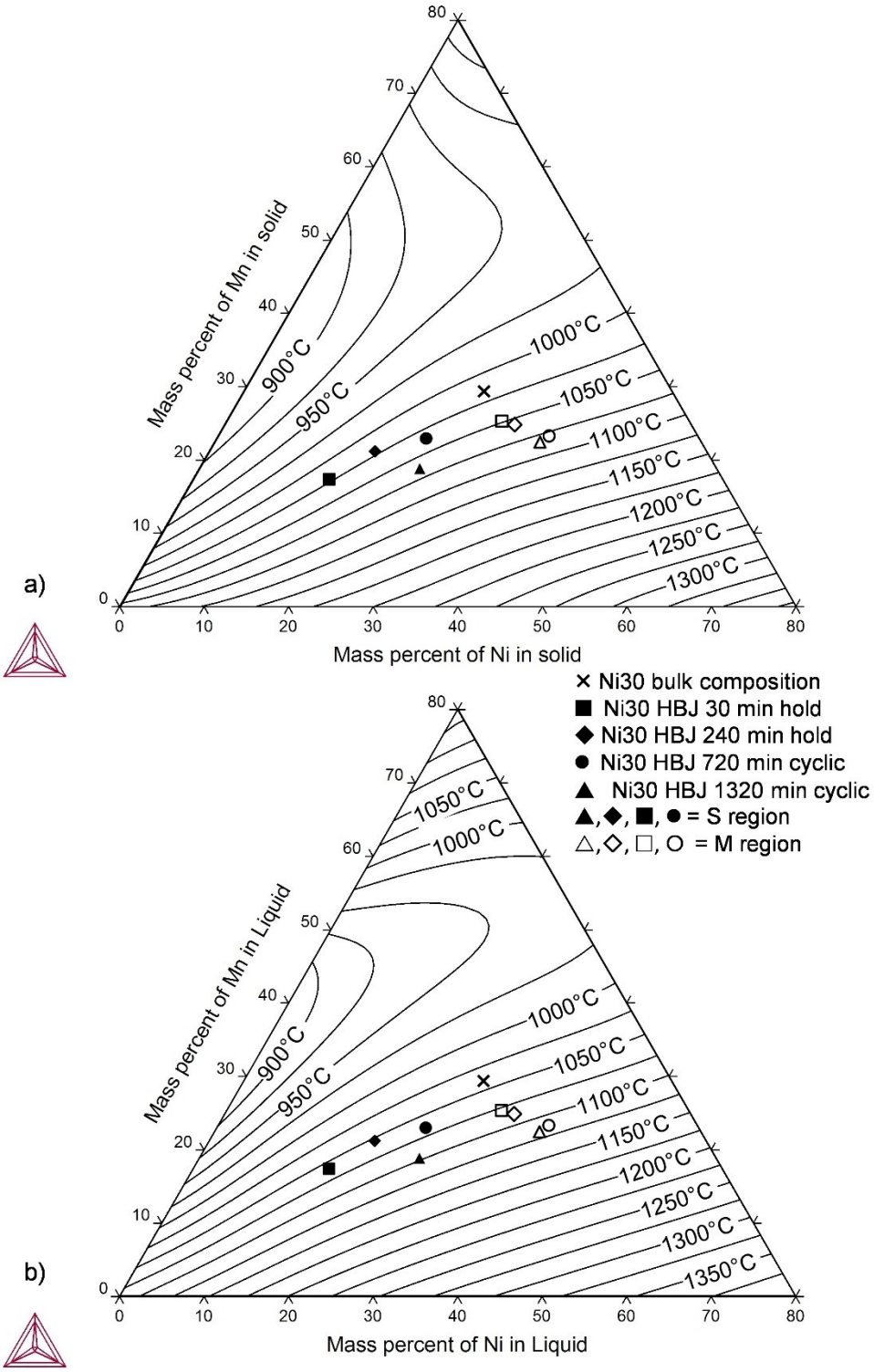

Figure 5.21 – Ni-Cu-Mn ternary solidus (a) and liquidus (b) diagrams with measured wide gap compositions plotted to estimate melting range of matrix and S region for each hold time 30 to 1320 minutes.

The T_{sol} of the matrix for a sample with a 30 minute hold is just below 1050 °C (1048.2 °C) indicating that the matrix would have been mostly solid on cooling identifying this region as the ISZ. The S region of the same sample has a calculated T_{sol} of 1015.33 °C indicating it would have been liquid on cooling identifying the S region as the ASZ. With all other hold times (240, 720, and 1320 minutes) the matrix was determined to have a T_{sol} above 1050 °C therefore confirming this to be the ISZ.

The calculated T_{sol} of the S region is found to increase as hold time increases due to the decrease in MPD content. HBJ samples held for 30 minutes and 240 minutes were found to have similar melting range. Examining cyclic samples brazed for a cumulative hold time of 720 and 1320 minutes shows IS progress in the form of increasing T_{sol} of the S region. The S region after 12 cycles (720 min) has a melting range of 1033 to 1068.7 °C indicating that a portion of this region was liquid on cooling, i.e. ASZ. The S region of 22 cycle HBJ sample (1320 min) was found to have a T_{sol} of 1052.81 °C and T_{liq} of 1093.01 °C. It was previously found (Section 5.2) that T_{sol} calculated by Thermocalc® can be underestimated by 5-20°C when compared to experimental T_{sol} measured by DSC for Ni-Cu-Mn ternary alloys. This suggests that the S region could have an actual T_{sol} of 1048 °C meaning that any liquid left after cycle 22 would be a very small volume fraction. The S region (ASZ) would be limited to small pockets of Cu-rich phase concentrated in the grain boundaries of the brazed region. Despite the small pockets of ASZ in the S region, the Ni30 HBJ brazed at 1050 °C for a cumulative 1320 minutes is considered to have reached full isothermal solidification. Figure 5.22 shows SEM micrographs of cyclic half braze joints held for 720 and 1320 minutes with the confirmed ASZ and ISZ labelled.

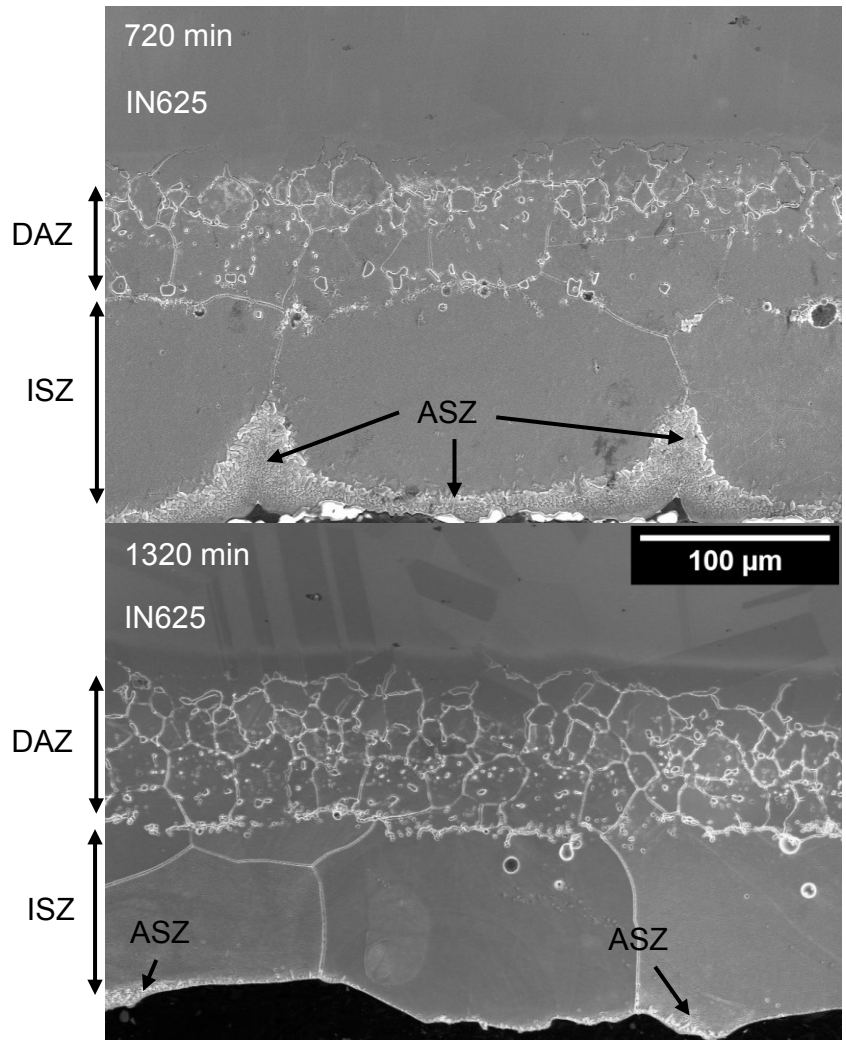

Figure 5.22 – SEM micrographs of Ni30/IN625 HBJ cyclic samples brazed for 720 and 1320 minutes.

5.6.3 EDS elemental line scans

EDS line scans were performed on the brazed region of wide gap HBJ samples brazed for 30, 240, 720 and 1320 minutes to determine the distribution of elements within the braze joint. The composition of thirty to forty points through the brazed region, DAZ, and base metal were taken and the results of all four line scans are shown in Figure 5.23. Accompanying micrographs showing the location of EDS points are included in Appendix A. The zero point in each graph is the location of the initial solid-liquid

interface which is the visible start of the DAZ. This is also the starting point measured for each braze joint in Figure 5.19.

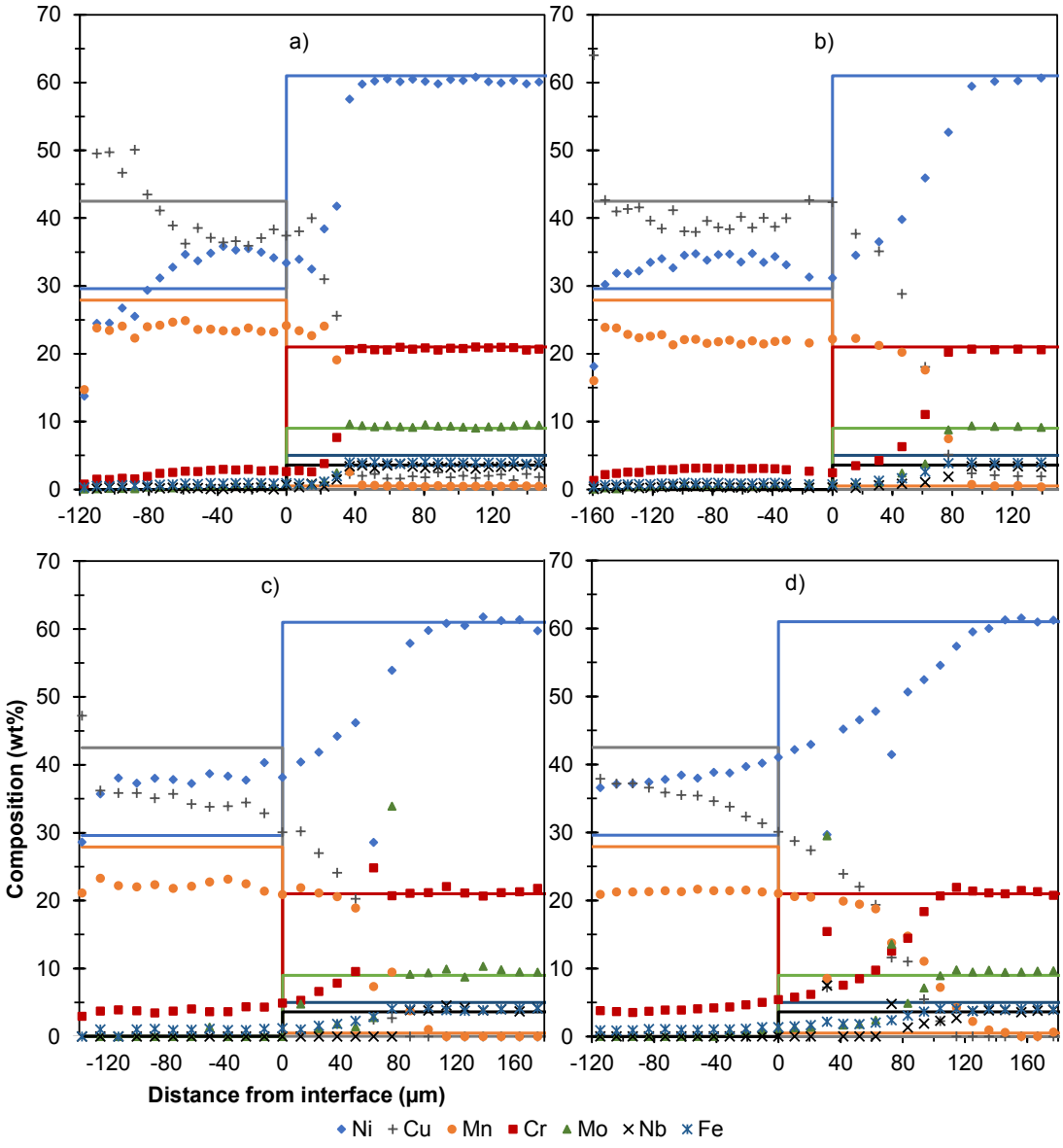

Figure 5.23 – EDS elemental line scans of wide gap Ni30/IN625 half braze joints held at 1050 °C for a) 30 minutes b) 240 minutes c) 720 minutes d) 1320 minutes. Zero point of each chart is the position of the initial solid liquid interface. Solid lines of each colour represent the initial composition of Ni30 (distance < 0) or IN625 (distance > 0).

Examining the left hand side of each graph (the brazed region) the measured composition of the braze joint can easily be compared to the initial composition of the Ni30 filler metal (shown as solid lines to the left of 0 µm in Figure 5.23). As shown

earlier (Section 5.6.1) the brazed region is primarily composed of Ni, Cu, and Mn, with small contributions (<5 wt%) of Cr, and Fe. In all braze joints, the Cu, and Mn content of the brazed region has decreased below the nominal Ni30 composition indicating that the MPD have diffused into the base metal. In Figure 5.23 a) and b) the data point with high Cu content are measured portions of the segregated region, this region was not captured in line scan in Figure 5.23 c) and d), though small amounts of the S region was present in these samples. Additionally, it can be seen that as the hold time at 1050 °C increases, the MPD content (Cu and Mn) decreases, and Ni content increases. As explained in the previous section, this means that the ISZ is growing (MPD content decreasing), and the ASZ is shrinking which indicates that isothermal solidification is progressing.

Another important feature illustrated in Figure 5.23 is the DAZ. Data points in the DAZ were selected to avoid measuring the precipitates. In some cases, Figure 5.23 c) and d), this was not possible due to the size of the electron beam. DAZ precipitates are shown in the line scans as points in which Mo is very high (>30 wt%). As expected, the composition of the DAZ matrix (positive distance from the interface) decreases in MPD elements, and increases in base metal elements until it returns to the composition of the base metal (solid lines to the right of 0 μm). The distance from the interface to the point where the composition resembles the unaffected base metal increases as hold time increases. This distance (the thickness of the DAZ) is measured to be roughly 44, 90, 110, and 125 μm for samples 30, 240, 720, and 1320 min hold time respectively. This increase in DAZ thickness is caused by increased diffusion of MPD elements into the base metal. Within the DAZ, the Cu content drastically decreases at the interface (x=0 μm) while the Mn content tends to remain elevated for roughly 30 to 50 μm. This

suggests that Mn diffuses into the base metal quicker than Cu. Neither Cu nor Mn were found in significant quantity in the DAZ precipitates (5 wt%) both elements remained in the FCC solid solution matrix.

5.7 Ni30/IN625 DSC enthalpy of melting

Since the ASZ has been identified through EDS elemental analysis and melting range calculations, it is now necessary to quantify the progression of isothermal solidification. This is done by accurately measuring the enthalpy of melting on the relevant DSC trace which is a measure of the liquid present on cooling in the brazed region. An important aspect in measuring the enthalpy of melting is baseline determination. Which will be covered in the following section.

5.7.1 DSC baseline determination

Figure 5.15 shows the initial melting endotherm and the accompanying linear baseline used to calculate the enthalpy of melting. Because the initial melting event of Ni30 in contact with IN625 base metal completes just before 1050°C the enthalpy of melting can be measured using a linear baseline (drawn in Figure 5.15). In contrast, the subsequent cycles have a melting onset of 984 °C increasing to 995 °C without returning to baseline which indicates that the melting event has not completed at 1050 °C. To measure the enthalpy of melting for cycles 2 through 22, a new baseline must be constructed to accurately describe the melting behaviour and accompanying kinetics of the system. Ni30 HBJ DSC samples brazed using the high temperature remelt thermal profile allow for examination of the fully resolved melting peak after increasing hold time at 1050 °C as shown in Figure 5.16.

Ni30 wide gap HBJ samples were subjected the isothermal hold + high temperature remelt thermal profile with hold time at 1050 °C of 0, 30, 60, 180, 240, 360, and 480 minutes. The segment on heating from 900 to 1200 °C for previously mentioned hold times are shown in Figure 5.16. Despite efforts to reduce changes in DSC baseline by using the same Al_2O_3 sample and reference crucibles, identical heating and cooling rates, Ar flow rate, and data sampling rate, there is a difference in baseline of the high temperature remelt. This is due to the nature of the half braze joint; there is a different amount of liquid present, and this liquid is of different composition after each hold time which has an effect on the baseline. Samples held for 0, 30 and 60 minutes at 1050 °C, the baseline of the HT remelt segment has a slight positive slope. The baseline for this segment has a slight negative slope in samples held for 180 to 480 minutes. Because the melting endotherm is fully resolved when heating to 1200 °C, a linear baseline is appropriate when measuring enthalpy and these differences in baseline slope are easily justified. With cyclic and low temperature remelt thermal profiles the heat flow of the end of peak, and therefore the slope of baseline, is not known.

There is a general trend in the slope of baseline: samples with larger amounts of liquid present on heating (i.e. shorter hold time or low cycle number) tend to have a slight positive slope, and samples with smaller amounts of liquid present (i.e. long hold time or high cycle number) tend to have a slight negative slope. Noting this trend is helpful but does not allow for quantification or prediction of baseline slope in samples which do not have a fully resolved melting peak. This makes accurate enthalpy determination of the cyclic and low temperature remelt samples difficult, but worthy of extensive analysis.

Three potential alternatives will be discussed: IN625 ingot subtraction baseline, left start tangential baseline, and last cyclic segment subtraction.

The sample mass and thermal contact with the crucible have a significant effect on the DSC trace [26] even if no phase transformation is occurring. To determine the DSC trace of IN625 the base metal ingot was heated in the DSC using the cyclic thermal profile heated to 1050 °C. The resulting DSC trace of the ingot can then be subtracted from the DSC trace of a Ni30/IN625 HBJ in NETZSCH Proteus ® software thus removing any thermal artifacts caused by the large mass of IN625 base metal.

The IN625 base metal brazing surface was prepared as outlined previously and placed in an alumina crucible with brazing surface in contact with crucible bottom. This sample was run as a correction file, meaning that the sample mass is not included in heat flow calculations. The resulting DSC trace is shown in Figure 5.24 as the dashed line. The baseline is shown to have a similar “swing” caused by the drastic change in heating rate when changing from cooling to heating at 900 °C and has a slight negative slope on heating from 900 to 1050°C. Compared to the DSC trace of Ni30/IN625 22 cycle HBJ sample (1320 min hold time) the DSC trace of the IN625 ingot only is most similar to cycle 22 on heating which has the smallest amount of liquid present. As confirmed in Section 5.6.2, this sample has undergone complete isothermal solidification but does contain very small pockets of liquid left on cooling.

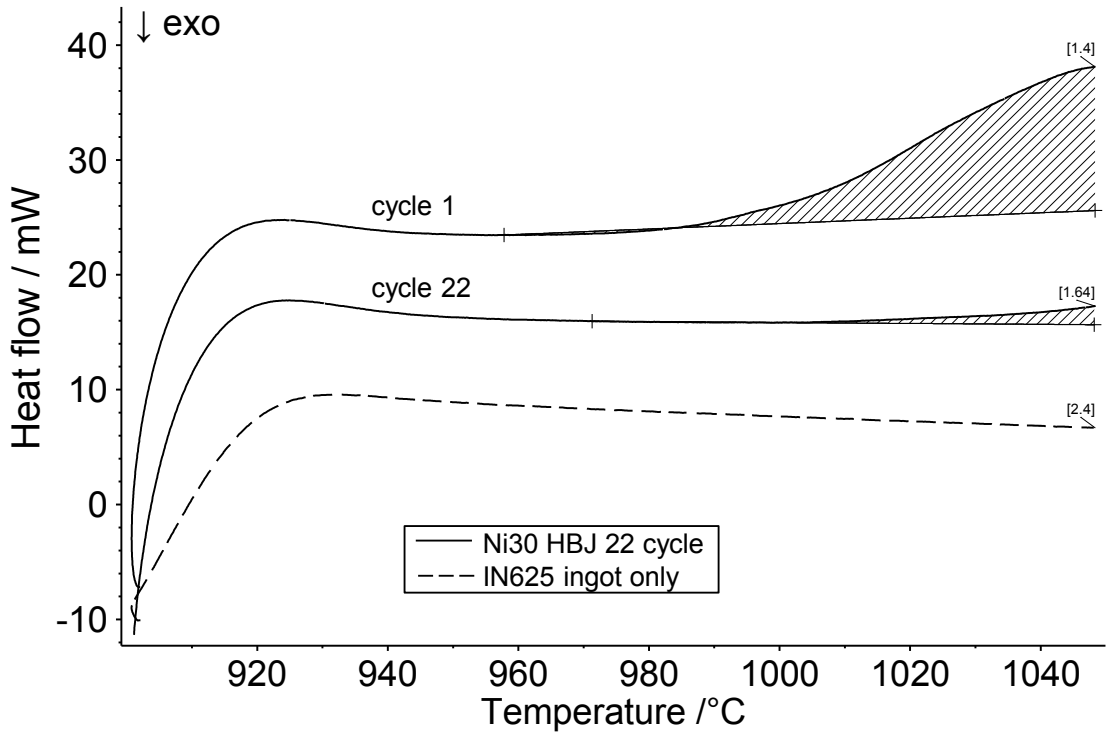

Figure 5.24 – DSC traces of Ni30 HBJ 22 cycle and IN625 ingot only samples comparing the respective baselines on heating from 900 to 1050 °C. Measured melting endotherms (shaded area) of Ni30 HBJ 22 cycle sample are determined using left start tangential baseline. Note: heat flow units are mW rather than mW mg^{-1}.

In NETZSCH Proteus ® software the IN625 ingot only DSC trace remelt segment was used as a direct subtraction for cyclic and low temperature remelt thermal profiles. The resulting enthalpy values for selected samples are shown in Figure 5.25 (grey data points). It was found that using the IN625 ingot as a direct subtraction results in an artificial increase in measured enthalpy in all cases. This is because the baseline is forced to be negative for all segments increasing the area of the peak. Looking at the DSC trace of HT remelt samples in Figure 5.16 it is known that this is not always the case.

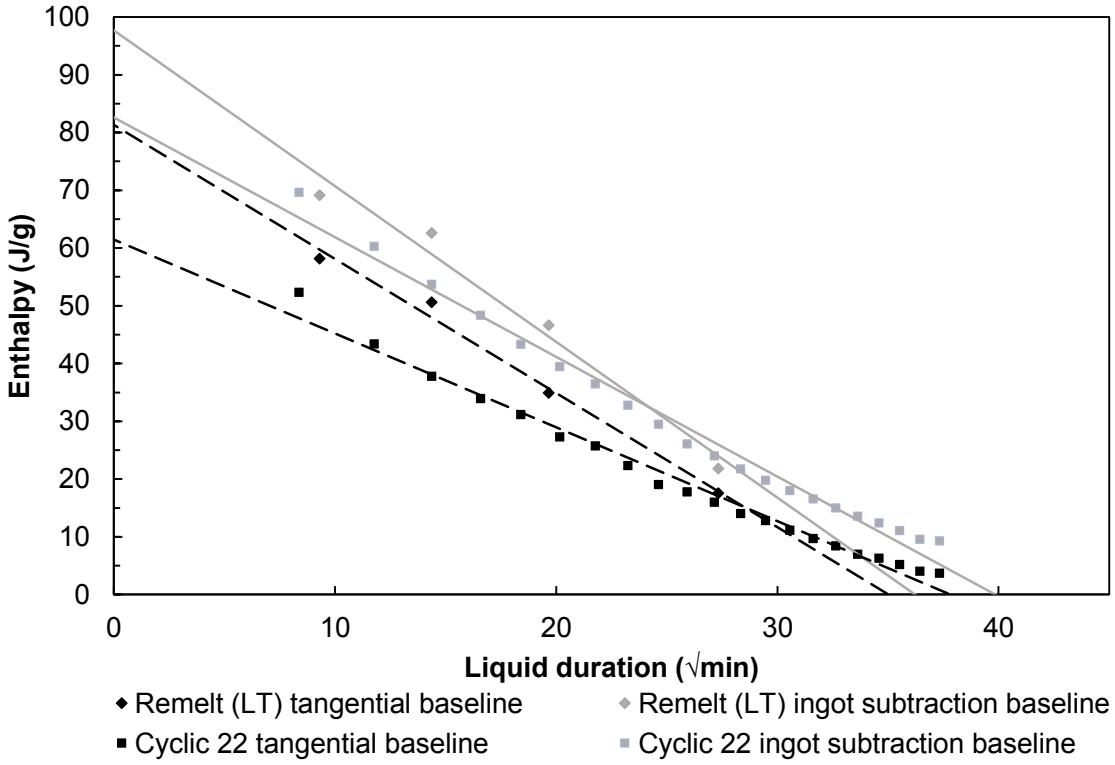

Figure 5.25 – Comparison of measured enthalpy values of cyclic and low temperature remelt half braze joints using tangential baselines (black data points) and IN625 ingot subtraction baselines (grey data points).

As an alternative to direct subtraction of baseline, the IN625 ingot only DSC trace can be used as a guide to determine when HBJ DSC traces begin to deviate from the IN625 ingot trace. This deviation can be thought of as the point at which liquid begins to form on remelt. At this point, a left start tangential baseline calculated in NETZSCH Proteus ® software can be applied. This baseline is shown as calculated by Proteus® in Figure 5.24 for Ni30/IN625 HBJ 22 cycle sample. Only cycles 1 and 22 on heating are shown in Figure 5.24 to clearly illustrate the difference in slope of baseline as cycle number increases and thus liquid fraction present decreases. The left start tangential method results in a slightly positive sloped baseline for cycle 1, and a slightly negative sloped baseline for cycle 22. This is consistent with the trend of baselines found in high temperature remelt samples (shown in Figure 5.16) suggesting that this is a suitable

method of baseline determination for both cyclic, and low temperature remelt thermal profiles. A comparison of resulting enthalpies with these two baseline determinations is shown in Figure 5.25. The use of ingot subtraction method increases the melting endotherm measurement in both cases.

The final potential method for baseline determination is last cycle segment subtraction proposed by Moreau and Corbin [56], and used by Tadgell [57] valid only for cyclic thermal profiles. The method creates a self correction for individual samples by using the final cycle of the DSC trace as the baseline for all previous cycles. Using a baseline calculated from the same DSC sample removes any concern of baseline deviation caused by sample mass, thermal contact between sample and crucible, or sample location within crucible; all factors which can have an effect on the baseline of the resulting DSC trace. This method can only be used if the braze joint has undergone complete isothermal solidification. Samples brazed with boron containing braze metals, can be examined optically to determine that no centreline eutectic phase (liquid) is present in the resulting microstructure. When brazing with Ni30 filler metal, as in current study, the presence of a liquid phase cannot be identified by optical microscopy alone but must use EDS analysis and calculation of melting range for each region as explained in Section 5.6.2. The S region of Ni30/IN625 HBJ sample brazed for 12 cycles (720 min) was found to have a T_{sol} of 1033.84 °C confirming this region as the ASZ. This liquid portion means that the last heating segment of 12 cycle DSC trace cannot be used to self correct the initial 11 heating segments. It was determined previously that the Ni30/IN625 HBJ brazed at 1050 °C for 22 cycles (1320 minutes) is considered to have reached full isothermal solidification and therefore is permitted to use this baseline determination.

This is the only sample examined in this work that can use the last cycle subtraction method for baseline determination.

A linear regression was performed for all three baseline determinations using the 22 cycle HBJ sample. The resulting linear trendlines are shown in Figure 5.26 as a graphical comparison. All baseline determination methods resulted in a linear relationship between enthalpy of melting and square root of liquid duration. All data sets resulted in an R^2 value of greater than 0.98 indicating a strong linear relationship. The decrease in enthalpy of melting as time above solidus increases indicates that isothermal solidification is progressing through diffusion between the base metal and braze joint. The effect of baseline determination on enthalpy measurement for successive cycles is apparent, and influences both the trendline slope, and the time to full isothermal solidification (denoted as t_f). The baseline using the IN625 base metal as a subtraction resulted in a slope of -2.07 J/g$\sqrt{}$min and t_f of 1588.9 min. A left start tangential baseline resulted in a slope of -1.63 J/g$\sqrt{}$min and t_f of 1429.9 min. The last cycle segment subtraction baseline resulted in a slope of -2.15 J/g$\sqrt{}$min and t_f of 1227.6 min. The base metal subtraction baseline increases the enthalpy for all cycles and results in the highest t_f. This baseline method artificially increases the measured enthalpy and is not the most suitable baseline.

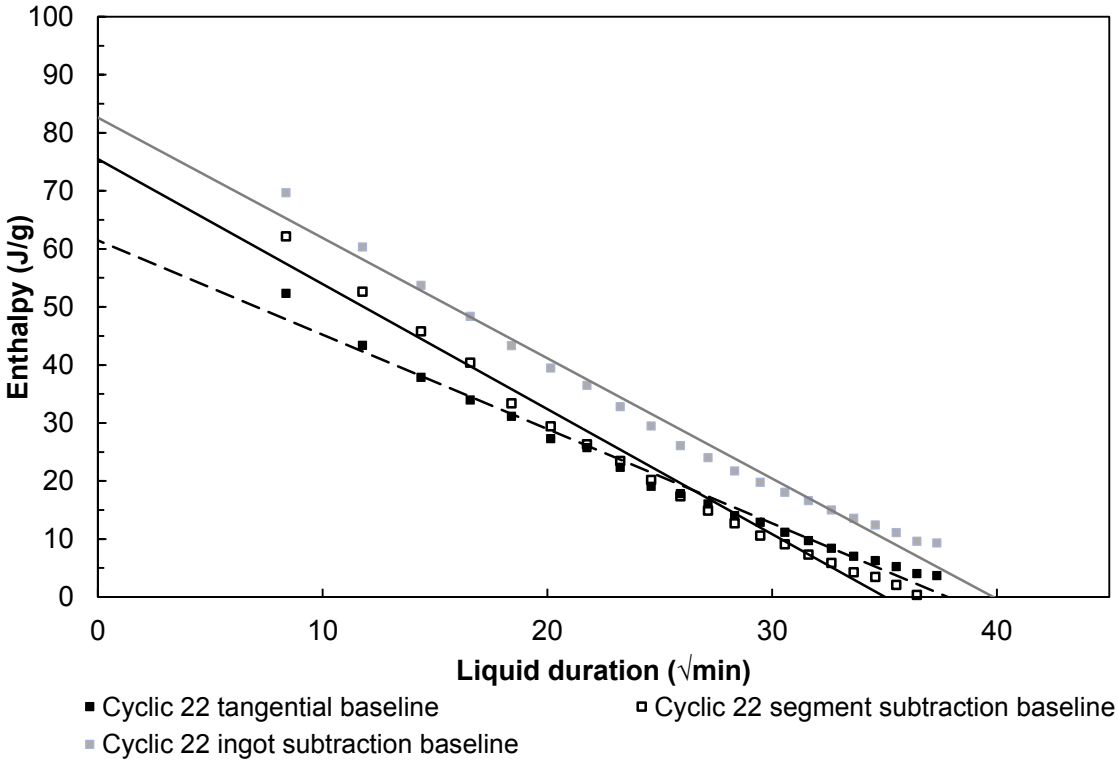

Figure 5.26 – Comparison of enthalpy of melting in 22 cycle Ni30 HBJ using three baseline determination methods: tangential baseline, ingot subtraction baseline, and last cycle segment subtraction.

The last cycle segment subtraction method and left start tangential baseline method have the most significant difference in enthalpy measurements in cycles 1 to 5. Cycles 6 and greater have very similar measured enthalpy meaning the baselines are similar. The tangential baseline method is the most viable method for two reasons: 1) the method can be applied on any isothermal hold or cyclic thermal profile making comparisons viable, 2) the baseline is determined based on data from the relevant DSC trace. For these reasons a tangential baseline will be used for enthalpy measurements in all DSC traces. The enthalpy measurements of the 22 cycle wide gap HBJ will be shown using both tangential and last segment subtraction in the following work to illustrate how the baseline determination affects the calculated kinetics of the system.

5.7.2 Experimental kinetics of isothermal solidification

With an acc urate and consistent method of baseline determination defined, enthalpy measurements from cyclic, and low temperature remelt samples were made in NETZSCH Proteus ®. These enthalpy values are used to calculate the liquid fraction remaining in the HBJ. Liquid fraction can in turn be used to calculate the liquid width, and maximum braze clearance of the IN625 Ni30 half braze joint. The relationship between liquid width and time of liquid duration determine the progress of isothermal solidification and the kinetics of the system. The technique used to determine liquid fraction was developed by Kuntz et al. [23], [30] while studying TLPB of Ag base metal and Ag-Cu eutectic foil. To determine the liquid fraction present in the system, the enthalpy of the fully liquid filler metal must be known. As found by Kuntz, the measured enthalpy of HBJ (filler metal in contact with the base metal), is significantly lower than the measured enthalpy of only the filler metal. The decrease was noted to be caused by two factors: solid state diffusion between the filler metal and base metal, and thermal dampening caused by the comparatively massive base metal. The solid state diffusion is an important factor in TLPB and can be confirmed by microstructural examination. Thermal dampening is an artifact of DSC measurement caused by the comparatively massive base metal ingot and must be addressed to ensure proper determination of kinetics.

Kuntz et al. proposed a thermal barrier DSC test in which the filler metal is prepared as normal, and the base metal is encased in a “stop off” compound to act as a metallurgical barrier between the filler metal and base metal. In this configuration, the filler metal will fully melt at the brazing temperature without metallurgical interaction

with the base metal but replicating the effect of thermal dampening of the IN625 base metal mass. The thermal barrier configuration will be referred to as Ni30//IN625 for brevity. Figure 5.27 shows the melting endotherms of Ni30 filler metal only and Ni30//IN625 on 2nd and 3rd melting cycle (using cyclic DSC thermal profile as described in Section 4.3 Figure 4.2). The DSC traces are of very similar shape and melting range indicating that no metallurgical interaction with the base metal is taking place and at 1050 °C the Ni30 is fully liquid. Post DSC, the Ni30 filler metal solidified in the shape of flattened disc when in the presence of IN625 thermal barrier. The disc and base metal were examined macroscopically and were found to have no obvious metallurgical interaction with each other. Furthermore, the Y_2O_3 layer was intact on surface of the IN625 base metal indicating that there had been no wetting of the base metal by the liquid Ni30 filler metal.

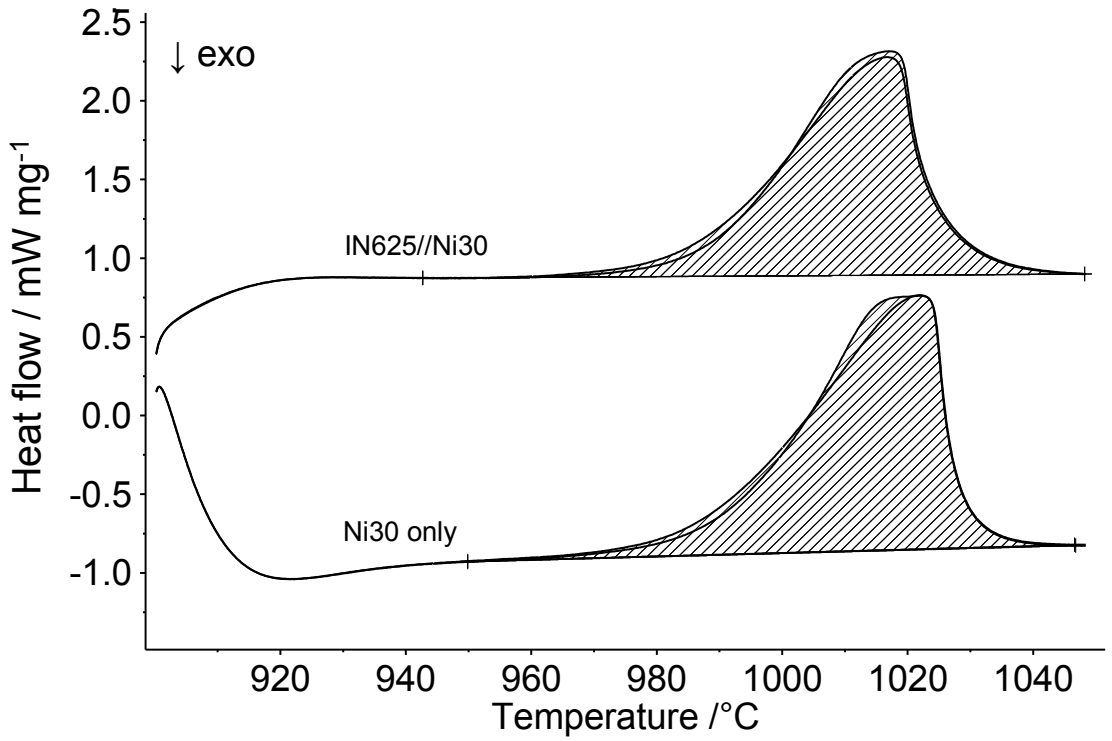

Figure 5.27 – DSC traces of Ni30 filler metal only (20 mg) and Ni30 filler metal (20 mg) with thermal barrier between IN625 base metal and filler metal (IN625//Ni30). Cycles 2 and 3 are shown. Note: traces have been offset in the y-direction to separate traces.

Table 5.7 shows the measured enthalpy of melting for both sample configurations for narrow and wide gap conditions. As expected, the enthalpy of melting and solidification of Ni30 decreased when IN625 base metal was added in thermal contact only. Wide gap melting enthalpy decreased from 124 to 108 J/g, and solidification enthalpy decreased from 126 to 108 J/g, a loss of 12.9% and 14.2% respectively. Narrow gap melting enthalpy decreased to 96.9 J/g, and solidification enthalpy decreased to 93.0 J/g. It is clear from these measurements that the base metal does cause thermal dampening and decreases the ability of the DSC to measure enthalpy.

Table 5.7 – DSC enthalpy measurements of Ni30 filler metal powder with and without presence of base metal on 2nd and 3rd melting cycles.

Sample type	Ni30 mass (mg)	Average enthalpy of melting (J/g)	Average enthalpy of solidification (J/g)
Ni30 (filler metal only)	20	123.7 ± 4.1	126.1 ± 3.4
Ni30//IN625 (thermal barrier)	20	107.9 ± 1.1	107.9 ± 0.8
Ni30//IN625 (thermal barrier)	7	96.9 ± 1.4	93.0 ± 3.0

To account for this thermal dampening in HBJ samples, the enthalpy of melting of the thermal barrier test (ΔH_0) will be used in liquid fraction calculations, i.e. ΔH_{0N} for narrow gap conditions is 96.9 J/g, and ΔH_{0W} for wide gap conditions is 107.9 J/g . The liquid fraction can now be calculated by Equation 2:

$$L_f = \frac{\Delta H_t}{\Delta H_0} \tag{2}$$

Where L_f is liquid fraction, and ΔH_t is the enthalpy of melting measured at a certain time. L_f is a quantification of the progress of isothermal solidification and can also measure the interaction between filler metal and base metal on initial melting. The enthalpy of initial melting of Ni30 IN625 HBJ, varies slightly by sample (to be expected with complicated powder melting, solidification, and remelting events) but is always less than ΔH_0. The average enthalpy of initial melting of Ni30 and IN625 half braze joints was calculated to be 68.7 ± 10.4 J/g resulting in a L_f of 0.636 ±0.096. This decreased enthalpy could be misconstrued to indicate that the Ni30 filler metal has not fully melted.

Microscopic evaluation has shown that after a 0 minute hold at 1050 °C and subsequent cooling, the filler braze joint has been fully melted indicated by the fully dense brazed region. Additionally, if the filler metal powder mixture did not fully melt there would be visible prior particle boundaries of the unaffected powder particles. No

evidence of prior particle boundaries was found on microstructural examination. Instead, the reduced L_f is attributed to metallurgical interaction with the base metal and diffusional solidification (DS) of a portion of the filler metal. This DS begins as soon as the solidus temperature is reached during initial heating to 1050 °C. A portion of the braze region alloys with the base metal to a point where the melting point has increased above 1050°C. This DS was examined in Section 5.2 for a zero min hold narrow gap sample (see Figure 5.10 and Figure 5.11 of Section 5.2). Through EDS elemental analysis, it is known that this mechanism is through diffusion of MPDs (Cu and Mn) from the braze region into the base metal, and diffusion of Ni from base metal in to the braze region. A DAZ region approximately 40 μm thick was measured for this zero min sample.

Using Equation 2, the liquid fraction was calculated for both wide and narrow gap half braze joints and plotted in Figure 5.28. As expected from enthalpy measurements, the liquid fraction decreases as liquid duration increases. A linear relationship is found when liquid duration unit is √min. There is good agreement between data sets using cyclic and isothermal hold remelt thermal profiles for wide gap conditions. This confirms that the cyclic method is valid for tracking the isothermal solidification progression. As expected, the narrow gap data set, using 7 mg Ni30 filler metal powder, has a lower initial liquid fraction compared to wide gap.

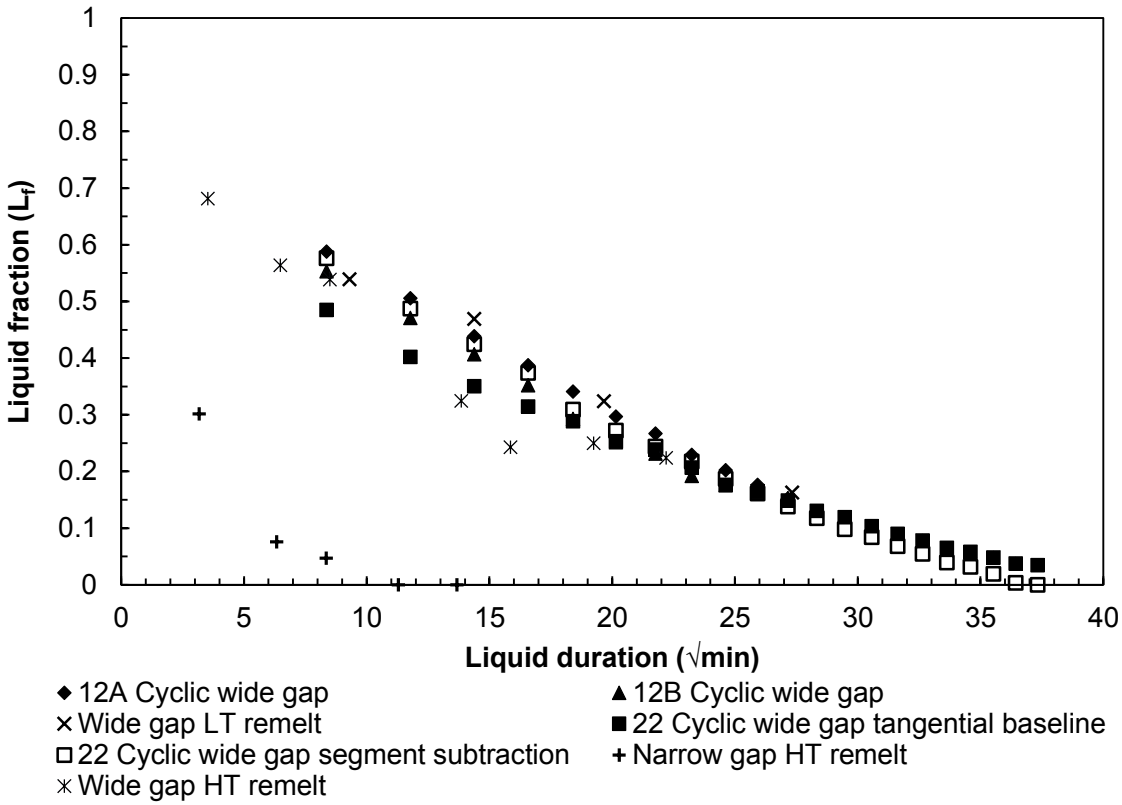

Figure 5.28 – Liquid fraction present as a function of liquid duration of Ni30/IN625 HBJ. Narrow and wide gap data. Where not specified, tangential baseline method was used.

When the initial width or gap of the braze joint is known, the liquid fraction can be converted to the width of remaining liquid phase, w_t, as shown in the following equation first explained by [31]:

$$2w_t = \frac{\Delta H_t}{\Delta H_0} 2w_0 = L_f \times 2w_0 \quad (3)$$

Where w_0 is the initial thickness of a half braze joint. Both the initial braze gap thickness and the width of remaining liquid phase are multiplied by two in Equation 3 to model a full braze joint which will be twice the width of the experimental half braze joints.

The initial width of braze gap is usually taken to be the thickness of filler metal foil, or, in the case of a full gap, the fixed distance between plates. As described earlier, the Ni30 is compacted to a DSC sized pressed disc. In the green state, this pressed disc is very fragile and accurately measuring the thickness of the disc is not possible. To

determine the theoretical thickness of the pressed disc, 20 mg of Ni30 was heated to 1050°C and cooled, fully melting the sample and solidifying into a sphere. This sphere of Ni30 was then pressed in the DSC sized die and punch used previously for powder compaction. This allowed the sphere to be pressed to a disc similar in diameter to that of the pressed powder discs. The density was then determined by measuring the surface area, and thickness through optical microscopy and image analysis software FIJI [55]. The density of the fully dense Ni30 discs was determined to be 8.54 g/cm^3. With volume conserved, a disc of this density, diameter 4.7 mm, and mass of 20 mg would therefore have a theoretical thickness of 127 μm. The theoretical thickness of the full wide gap braze joint is therefore 254 μm.

This theoretical braze joint thickness can be compared to the measured braze joint thickness of all narrow and wide HBJ samples as shown in Figure 5.19. The measured thickness was found to be consistently larger than the theoretical braze thickness by approximately 50 μm, at all hold times. This increase in braze thickness is attributed to a small amount of base metal dissolution. This dissolution would occur rapidly during initial heating of the base metal. To more accurately calculate the width of liquid and maximum brazing clearance, the larger measured thickness of braze joint will be used as w_0. Each data set will therefore have a slightly different w_0 (ranging from 150 to 190 μm) based on the measured braze thickness value. The $2w_0$ will therefore range from 300 to 380 μm. Wide gap samples brazed using the high temperature remelt thermal profile do not allow for a measured braze thickness because of significant widening due to the final heating segment (1200 °C). Therefore, this data set will not be included in further analysis which requires a measured braze thickness. The narrow gap HT remelt samples

have the same issue. In order to compare narrow and wide gap conditions, narrow gap samples were prepared using isothermal hold thermal profile for microstructure analysis and to measure the braze thickness. Narrow gap HT remelt data will use these measured values in further analysis. The liquid width plot for narrow and wide gap samples is shown in Figure 5.29.

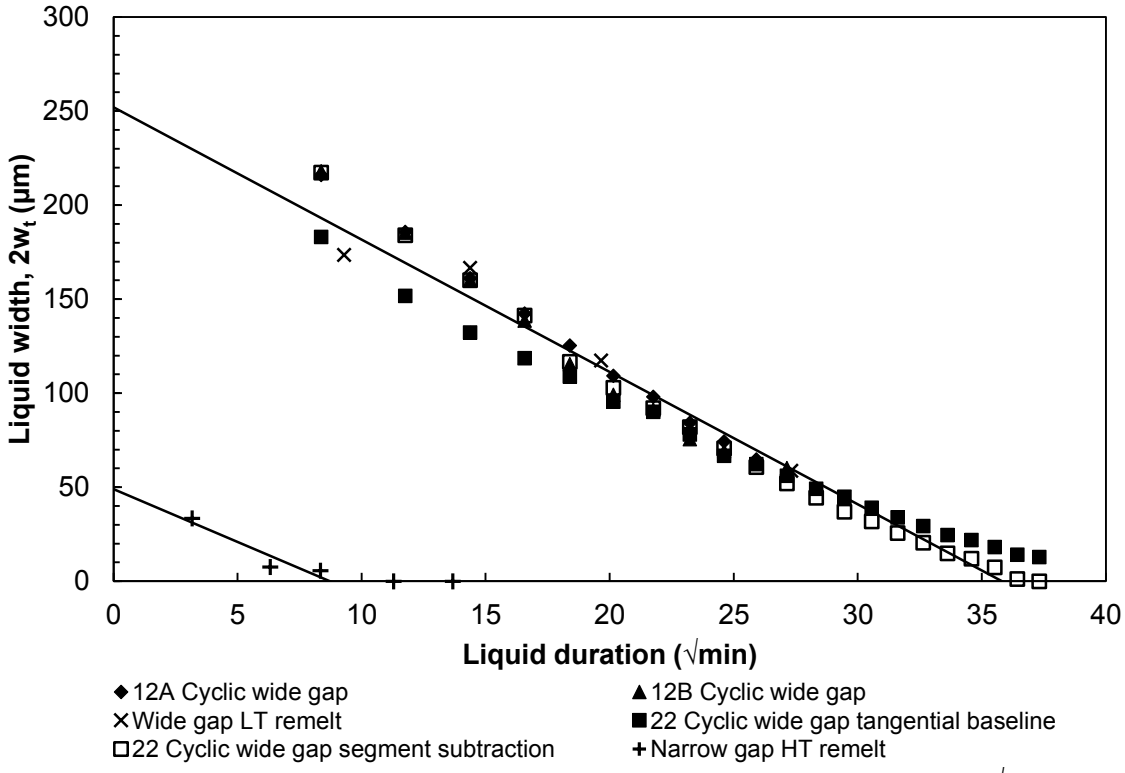

Figure 5.29 – Width of liquid left on cooling as a function of liquid duration (√min) Ni30/IN625 HBJ in narrow and wide conditions. Extrapolated initial wide gap $2w_i$= 253 µm. Extrapolated initial narrow gap $2w_i$= 52 µm. Wide gap linear regression includes all wide gap cyclic and remelt samples.

A linear regression of the data allows for analysis of the y-intercept and slope of the system as shown below:

$$2w_t = -kt^{\frac{1}{2}} + 2w_i \quad (4)$$

Where $2w_i$ (y-intercept) is the extrapolated initial width of the liquid region (ASZ) of a full braze ($2w_{ASZ0}$) and k is the growth rate of the ASZ. The linear trendline shown in

Figure 5.29 was calculated by taking all wide gap data (cyclic and isothermal hold samples) into account and is therefore an average trendline of multiple samples. The $2w_{ASZ0}$ value was calculated to be 253 μm for wide gap conditions and 52 μm for narrow conditions. The slope of the linear regression, k, the rate at which the ASZ decreases in width, was calculated to be -7.04 μm $min^{-1/2}$. For narrow conditions, k was calculated to be -6.17 μm $min^{-1/2}$.

The time of complete isothermal solidification, t_f, can be determined by setting $2w_t=0$, i.e. the liquid width is 0 μm or the x-intercept, in Equation 4 and rearranging to give:

$$t_f^{\frac{1}{2}} = \frac{2w_i}{k} \tag{5}$$

Using the linear regression variables stated above (k and $2w_i$), the experimental time of complete isothermal solidification was determined to be 1283±134 minutes for wide gap conditions, and 76 minutes for narrow gap conditions.

The maximum brazing clearance at a certain hold time indicates the width of the ISZ in the brazed region of a full braze joint. This plot predicts the hold time (time above solidus) that must be achieved to fully isothermally solidify a joint of any width. In this regard it also provides the rate of isothermal solidification. Theoretically, the width of the ISZ at any time before full isothermal solidification has occurred (when $w_{ASZ} > 0$) should not depend on the initial gap thickness. It should grow at a rate governed by the diffusion coefficients of the solute atoms. The MBC at any given hold time can be calculated using the w_t, as in Equation 6, or using L_f, as in Equation 7.

$$MBC_t = 2(w_0 - w_t) \tag{6}$$
$$MBC_t = 2w_O(1 - L_f) \tag{7}$$

Figure 5.30 presents the MBC plot of both wide and narrow gap conditions. As in the case of liquid width plot, a linear regression of the MBC_t versus square root of liquid duration gives Equation 8:

$$MBC_t = kt^{\frac{1}{2}} + 2w_i \quad (8)$$

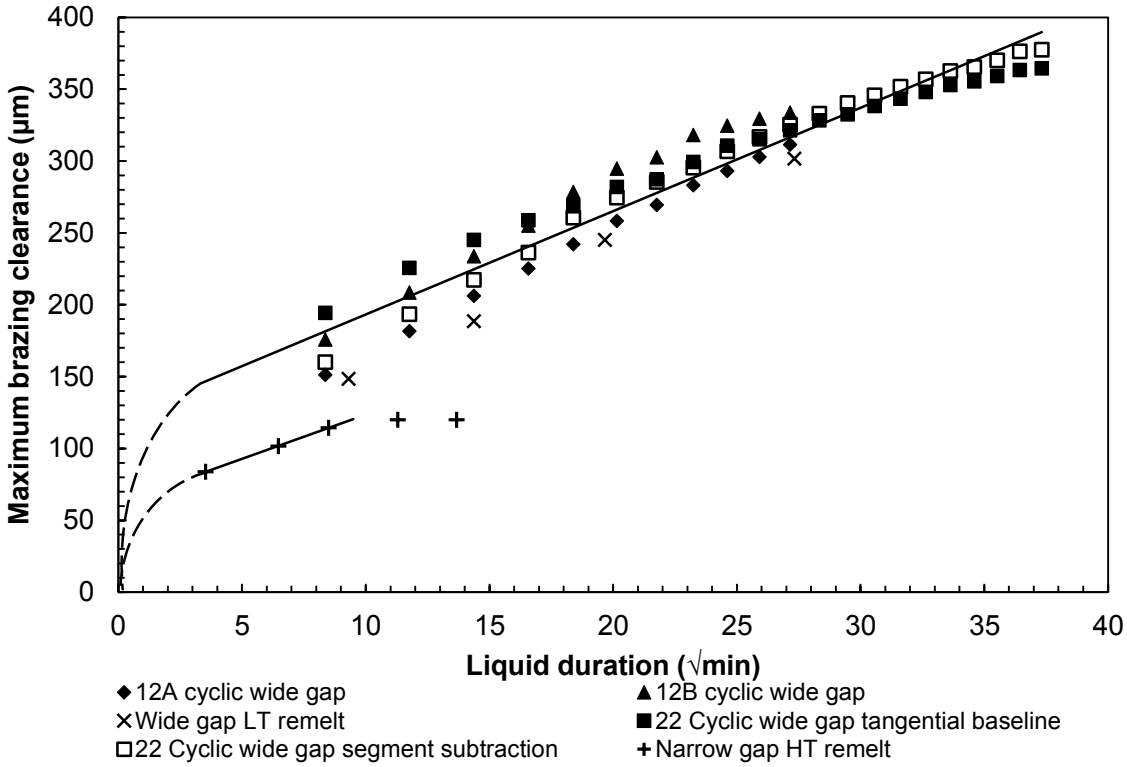

Figure 5.30 – Maximum brazing clearance as a function of liquid duration (√min) Ni30/IN625 HBJ in narrow and wide gap conditions. Solid line indicates calculated linear regression of data, dashed line indicates proposed growth of ISZ during initial melting and alloying of Ni30 filler metal powder mixture.

The linear regression of MBC using Equation 8 defines the extrapolated y-intercept as $2w_{ISZ0,}$ the initial width of the ISZ at 0 minute liquid duration. While this is a helpful value to compare agreement of data sets, it does not a have a valid physical definition. A Ni30/IN625 HBJ heated to 1050°C and immediately cooled experiences a liquid duration of 12.5 min (3.52 √min) which is the physical limit that can be experimentally examined in this system. The melting range of Ni30 FM (900 to 1050°C)

corresponds to liquid duration 0 to 7.5 min (2.74 √min) based on the DSC heating rate of 20 °C/min. At 0 √min liquid duration the Ni30 FM powder mixture has reached T_{sol} of initial melting and can not have an ISZ, therefore the MBC must have a y-intercept of 0. This temperature was characterized in Figure 5.3a) of Section 5.1 for Ni30 FM only (no base metal interaction) as the point in which NiCuMan37 powder particles begin to melt and alloy with pure Ni powder particles. Within this period of initial melting, the formation and growth of the ISZ is not known but would most likely be rapid growth once the filler metal metallurgically interacts with the base metal depicted as the dashed line in Figure 5.30. For this reason, the linear regression of Figure 5.30, Equation 8, is valid for liquid duration values greater than 3.52 √min.

Linear regression parameters calculated from liquid width, and MBC plots are summarized in Table 5.8. Analysing the slope of narrow and wide gap samples it is evident that in this case there is a small amount of discrepancy between the growth rate of samples conditions (approximately 1 μm $min^{-1/2}$). Under wide gap conditions the ISZ grows at a slightly faster rate than the narrow gap conditions. There exists a larger discrepancy between the extrapolated $2w_{ISZ0}$ (y-intercept) calculated to be 121 and 63 μm for wide gap and narrow gap conditions respectively. Possible explanations of this phenomenon are the effect of base metal dissolution, and experimental error in narrow gap work. As stated earlier, in wide gap samples the theoretical w_o was 127 μm, while the measured braze thickness ranged from 150 to 190 μm indicating an estimated base metal dissolution of between 23 and 63 μm in the half braze joint configuration. For a full gap, which is modelled in Figure 5.29 and Figure 5.30 this would equal 46 to 126 μm of base metal dissolution. Narrow gap samples had a measured thickness of 50 to 75 μm

indicating a maximum dissolution of 25 μm for a half joint and 50 μm for a full joint, significantly less than found in the wide gap. It is possible that the w_{ISZ} of the wide gap condition is taking this dissolution into account and the narrow gap condition does not take dissolution into account.

Table 5.8 - Summary of linear regression parameters calculated from Figure 5.29 and Figure 5.30.

Sample conditions	k (μm $min^{-1/2}$)	$2w_{AZS0}$ (μm)
Wide gap	7.04 - 7.19	252±18
Narrow gap	6.17 – 6.13	53

Less experimental work was performed with the narrow gap configuration because of limitations with the experimental design. It was found that using only 7 mg of filler metal powder resulted in inconsistent wetting of the base metal due to initial powder placement. Inconsistent wetting results in a large variation in braze thickness and decrease in surface area contact between the filler metal and base metal. Both of these inconsistencies have a negative effect on the repeatability of narrow gap conditions. Wide gap configuration using a larger mass of powder in a pressed disc resulted in better initial contact and complete wetting of the base metal by the Ni30 filler metal. More work utilizing the narrow gap configuration would allow for an error assessment of the extrapolated $2w_{ISZ0}$ (initial liquid width). As shown in Figure 5.29 and Figure 5.30, repeated DSC runs of wide gap Ni30/IN625 HBJ did result in a range of MBC values which would also be expected in the narrow gap configuration.

Additionally, short hold times (< 60 minutes) in the wide gap condition were not examined for thermal analysis because longer hold times were found to be necessary to

achieve full or high levels of IS. It is possible that examination of shorter hold times in the wide gap condition would clear up this disagreement.

5.8 Isothermal solidification prediction determination

To validate the findings of the experimental kinetics of TLPB found in Section 5.7.2 a theoretical prediction model was explored. Researchers have attempted to accurately model the isothermal solidification process of various TLPB filler metal/base metal couples to both verify their own work and compare to other work. Numerical, analytical, and hybrid models (using experimental and analytical methods) have been employed by researchers. As stated by Gale et al. [11], the most pressing challenge in isothermal solidification modelling is the lack of diffusivity data. Even models of boron containing filler metals and Ni-base superalloy systems use experimental diffusivity values that vary by two orders of magnitude [31]. Another complication of process modelling is the moving solid/liquid boundary. The motion of the boundary is assumed to follow a parabolic path mathematically. Compositionally it is not known whether equilibrium conditions can be applied to the solid-liquid interface as it moves with time [58].

In some systems (boron containing filler metals with Ni-base superalloys) it can be assumed that the compositions at the interface remain constant throughout isothermal solidification process because of the limited solubility of boron in nickel. While this is not true of the current work (Ni30 filler metal) this approach will be examined in the following section as a way to compare the kinetics of the Ni-Cu-Mn/IN625 system to a boron filler metal/Ni-base superalloy.

The process model used to predict isothermal solidification of the Ni30/IN625 diffusion couple is based on work completed by Murray, Arafin, Ojo, and Zhou [31], [58]–[60]. Zhou outlines separate analytical models for thermodynamically individual stages of TLP bonding: i) Initial heating to bonding temperature, ii) dissolution of base metal, iii) isothermal solidification, and iv) homogenization. The analytical model used in the following section considers only the isothermal solidification stage. As shown in Figure 5.31, the isothermal solidification phase of TLPB is the most time consuming. Dissolution occurs rapidly, on the order of a few seconds, while solidification is up to four orders of magnitude greater than dissolution. Note that homogenisation was not a goal of this study and will therefore not be considered. This work will be modelling only the isothermal solidification stage of TLPB.

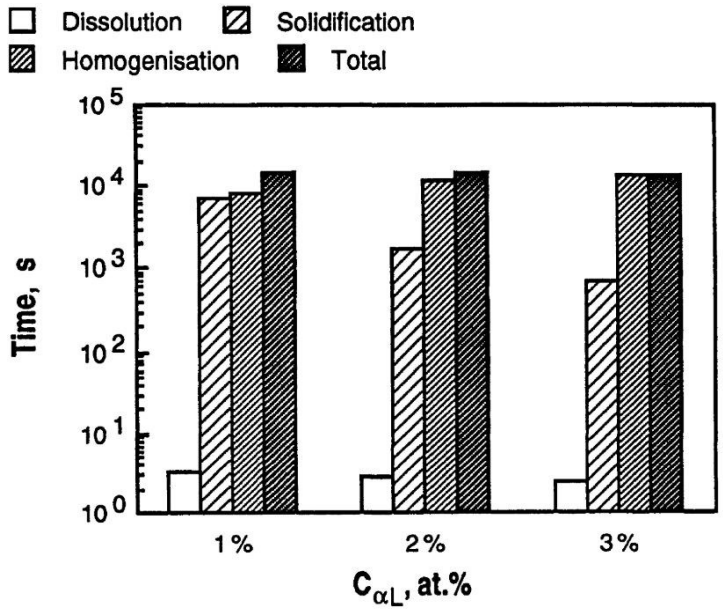

Figure 5.31 – Illustration of time contribution of each phase of TLP bonding. The effect of increasing solidus composition ($C_{\alpha L}$) on the completion time is shown [58]. Note: "Solidification" data set indicates isothermal solidification.

Arafin et al. [59] uses certain assumptions as the basis of their model which will be briefly outlined in this work for important areas. More detail can be found in works by

Arafin, and Zhou [59] , [11]. The model is a two phase moving boundary problem controlled by diffusion of solute into a substrate. The two phases are the solid phase (ISZ) and liquid phase (ASZ). The concentration of solute in the solid phase is modeled by a general error function [59]. The equation is based on a solution by Crank [61] for non-steady state diffusion of a solute into a semi-infinite substrate. For a full braze joint of thickness 2w isothermal solidification is considered to be complete when the solute concentration at the centre of the braze joint is equal to that of the solid phase. With these considerations Arafin [59] presents Equation 9:

$$C_s - C_m = (C_0 - C_m)\left(\text{erf}\frac{w}{\sqrt{4Dt_f}}\right) \tag{9}$$

Where C_s, C_0, and C_m are the MPD concentration of the solid phase, initial filler metal, and base metal (in at%.), w is the width of the braze joint, t is time, and D is the relevant interdiffusion coefficient. The content of both Cu and Mn in IN625 (C_m) is 0. Setting C_m=0 and rearranging to solve for t_f gives Equation 10 [31], [59]:

$$\sqrt{t_f} = \frac{2w_0}{4\,\text{erf}^{-1}\left(\frac{C_s}{C_0}\right)D^{1/2}} \tag{10}$$

Where $2w_0$ is the initial width of the full braze joint. For purposes of this model the initial width of joint will be the extrapolated full width of braze joint, $2w_{ASZ}$ or $2w_i$, determined from Figure 10, and presented in Table 5.8. This is 252 µm, and 53 µm for wide and narrow gap conditions respectively. Equation 10 was successfully used by Murray et al. [31] to experimentally predict the isothermal solidification time of a BNi-2 and IN625 braze joint and will therefore be used for the present Ni30/IN625 system.

5.8.1 Simplifications used in isothermal prediction calculation

Because Ni, Cu, and Mn are all atoms of similar sizes, the MPDs (Cu and Mn) will move by substitutional diffusion. Modelling diffusion of a ternary alloy system with a moving boundary is out of the scope of this thesis but several simplifications to the system can be made to describe a mathematical approximation of the system. In this way Equation 10, which is a model of a single solute into a substrate, can be used to model the Ni-Cu-Mn/IN625 system. The following simplifications were made:

1. The ternary Ni-Cu-Mn ternary system was converted to a pseudo-binary system by adding the compositions of both MPDs, Cu and Mn, in atomic percent. The combined MPD content will be the solute. For example, Ni30 alloy composition of 29.4Ni-39.3Cu-31.3Mn becomes 29.3Ni-70.6MPD (at%). Because Cu and Mn are of similar atomic radii (both substitutional diffusion with Ni), and similar coefficients of diffusion with Ni it was postulated that Cu and Mn must have similar contributions to the system. This is applied to C_S and C_0 of Equation 10.
2. Diffusion of base metal elements into the brazed region was not considered in the mathematical model. Inherent in the derivation of Equation 10 is that the composition in the liquid is fixed and uniform at C_0. Therefore, any mass transfer in the liquid layer is neglected.
3. D, diffusivity values were determined from literature values of interdiffusion coefficients of Cu, and Mn in pure Ni. A thorough literature search was performed and interdiffusion coefficients of Cu, and Mn in IN625 were not found.

In addition to simplification #1 stated above, C_s and C_0 must be considered for the Ni-Cu-Mn system. In boron containing alloys (BNi-2 for example), the composition of C_s is

limited by its low solubility in Ni, 0.3at%. Therefore, the composition of the solid, isothermally solidified phase, C_s, is constant. Conversely, Cu and Mn have very high solubility in Ni. Cu has full solid solubility in Ni, and Mn has very high solid solubility in Ni. Because of the high levels of solubility, C_s cannot be theoretically predicted and experimentally measured composition of the braze region will be utilized in the isothermal prediction model.

It has been experimentally determined that at certain hold times (> 30 minutes), the matrix (M) of the braze joint has been isothermally solidified. Therefore, this region will be thought of as the solid phase, C_s. The composition of the isothermally solidified matrix (M) has been found to change in composition based on hold time, decreasing in MPD content as hold time increases. Initially, Cs would be the first solid formed in the brazed region. In this study this was taken to be the composition of the matrix in the narrow gap half braze joint held at 1050 °C for 0 minutes. This composition will be noted as C_{S0}. The composition of this phase was calculated by Thermo-Calc to have a melting point above 1050°C confirming that it would have been isothermally solidified. C_s could also be thought of as the composition of the matrix phase after a very long hold time, experimentally in the wide gap HBJ cycled 22 times (1320 minutes at 1050 °C).This composition will be noted as C_{S1320}. The MPD content of C_{S0} is greater than that of C_{S1320}, and therefore the concentration gradient (Cs/C_0) will be greater. A larger concentration gradient will increase the rate of diffusion [62]. Both C_{S0} and C_{S1320} will be explored as possible C_s values because they will make the largest and smallest concentration gradient found in this work.

C_0 is defined by Arafin [59] and Murray [31] as the original composition of the filler metal (Ni30). In studying the composition of the braze ball, with no base metal interaction, there was a segregation of the matrix and S region (Table 5.1 of Section 5.1). Therefore the braze region on intial heating and remelting would not be homogeneous. Additionally, it was proven in Ni30/IN625 HBJ after 0 minute hold at 1050 °C that significant interdiffusion between the base metal and filler metal had occurred and caused partial DS. For these reasons it is valuable to examine several experimentally measured compositions in the model. The composition of the S region (ASZ, liquid) of the narrow gap HBJ held at 1050 °C for 0 minutes, and the wide gap HBJ cycled 22 times (1320 minutes at 1050 °C). Table 5.9 summarizes the compositions used in the isothermal solidification model.

Table 5.9 – Elemental compositions used for isothermal solidification predication model, Equation 10.

Sample conditions	Region	Name	Ni /at%	MPD (Cu + Mn) /at%
Ni30	Bulk composition	C_{0Ni30}	29.4	70.6 (39.2+31.4)
0 minute hold, narrow gap	S region (liquid)	C_{0Narr}	25.8	74.2 (47.6+26.6)
	Matrix (solid)	C_{SNarr}	35.9	64.1 (34.4+29.7)
22 cycle (1320 min hold), wide gap	S region (liquid)	C_{0W1320}	26.8	73.2 (52.5+20.7)
	Matrix (solid)	C_{SW1320}	39.1	60.9 (36.6+24.3)

5.8.2 Determination of interdiffusion coefficients

As stated in simplification #3 above, a literature search was performed to determine the diffusivity coefficients of Cu and Mn. Several groups ([63]–[65] have examined the Ni-Cu-Mn system both experimentally and computationally using DICTRA

(DIffusion Controlled TRAnsformation) module of Thermo-Calc. DICTRA® simulates diffusion based on a thermodynamic database, and an atomic mobility database (kinetic) [66]. For the purpose of this work, DICTRA can calculate the interdiffusion coefficients of the Ni-Cu-Mn system over a range of temperatures and solute concentrations. Diffusion modelling is a relatively new field and there has been a significant effort by computational materials engineers to thoroughly assess the accuracy and relevance of atomic mobility databases. Assessing the atomic mobility database across a range of temperatures and compositions for the Ni-Cu-Mn system is the primary focus of works [63]–[65].

Wang et al. [64] assessed the diffusion mobility of FCC Cu-Ni alloys and determined the DICTRA atomic mobility database resulted in good agreement between experimentally determined and calculated interdiffusion coefficients. Zhu [63] expanded on this work and analysed the application of diffusion and mobility database to Ni-Mn, Mn-Cu, and Ni-Cu-Mn systems. Zhu et al. again found calculated interdiffusion coefficients agreed well with experimental work. Because the interdiffusion coefficients are temperature and composition dependant it is important to define the parameters of the system. The brazing temperature of 1050 °C (1323 K), and MPD content (X_{MPD}) of 0.71 will be used. References generally focussed on examinations of temperature range 800 to 1050 °C, and Ni and Cu rich compositions. Diffusion coefficients for the ternary Ni-Cu-Mn system were used by Zhu et al. [63] to examine specific diffusion couples and were not relevant to this work. The restrictions in data will be discussed in more detail below.

Figure 5.32 shows the Ni-Cu interdiffusion coefficients over the full composition range, and at temperatures 1073, 1123, and 1273 K (800, 850, and 1000 °C). The data set

at 1273 K in [63], [64] is the highest temperature found in literature. While it would be ideal to have diffusivity data at 1323 K (the brazing temperature examined in this work) an extensive literature search did not return work at the brazing temperature. Using the 1273 K dataset the interdiffusion coefficient was read at X_{Cu}=0.71(composition of Ni30).

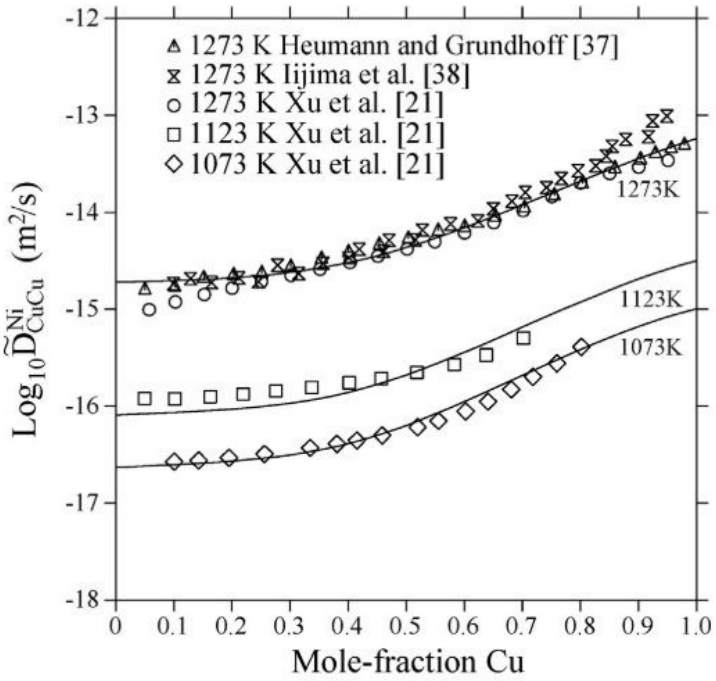

Figure 5.32 – Experimental and calculated interdiffusion coefficients for FCC Ni-Cu alloys [63].

As shown in Figure 5.32, the diffusion rate increases as temperature increases. Therefore, using the diffusion coefficient at a lower temperature will results in a slightly slower diffusion rate and ultimately increase the predicted time of isothermal solidification. The Ni-Cu interdiffusion coefficient used in the prediction model is shown in Table 5.10.

Table 5.10 – Summary of interdiffusion coefficient values used in isothermal predication model.

Reference	Species	Temperature /K (°C)	Interdiffusion coefficient /m^2 s^{-1}
[63], [64]	$\widetilde{D}^{Ni}_{Cu}$	1273 (1000)	1.37×10^{-14}
[63]	$\widetilde{D}^{Ni}_{Mn}$	1323 (1050)	39.8×10^{-14}

Figure 5.33 shows the Ni-Mn interdiffusion coefficients from X_{Mn}=0 to 0.6, at temperatures 1073 to 1323 K (800 to 1050 °C). Again, it would be ideal to have diffusivity data over the full composition range, but data found in literature was limited to the Ni rich portion of the Ni-Mn system. Using the 1323 K (1050 °C) dataset the Ni-Mn interdiffusion coefficient was read at X_{Mn}=0.6 and presented in Table 5.10. As the Mn fraction increases the interdiffusion coefficient also increases but above X_{Mn}=0.5 the slope decreases. Therefore, the interdiffusion read at X_{Mn}=0.6 is expected to be very similar, though slightly lower, than the value at X_{Mn}=0.71.

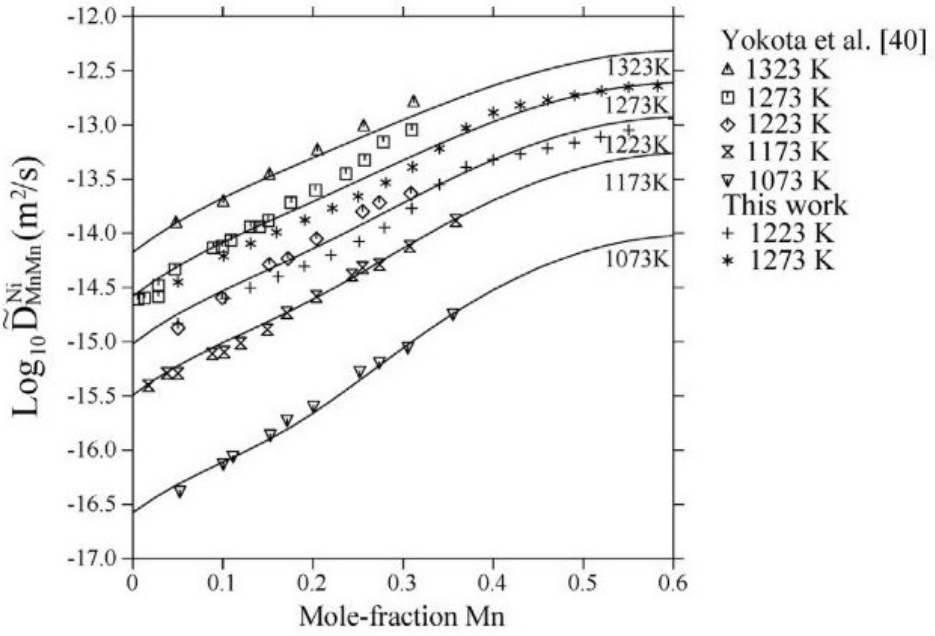

Figure 5.33 – Experimental and calculated interdiffusion coefficients for FCC Ni-Mn alloys [63].

Table 5.10 shows that the interdiffusion coefficient of Mn and Ni is 29 times faster than that of Cu and Ni. This is consistent with experimental work. In elemental analysis it was found that the Mn content (while lower than Cu) was more uniform in the braze region. Additionally, Mn was found to diffuse farther into the base metal than Cu at all hold times.

The actual Ni-Cu-Mn interdiffusion coefficient rate was hypothesized to be within the range of $\widetilde{D}_{Cu}^{Ni}$ and $\widetilde{D}_{Mn}^{Ni}$. The final Ni-Cu-Mn interdiffusion coefficient used in the prediction model was calculated using the rule of mixtures. This assumes that the contribution of Mn and Cu to $\widetilde{D}\,_{CuMn}^{Ni}$ is equal to the molar fraction of each element as in Equation 11.

$$\widetilde{D}\,_{CuMn}^{Ni} = X_{Cu}\widetilde{D}_{Cu}^{Ni} + X_{Mn}\widetilde{D}_{Mn}^{Ni} \tag{11}$$

Where X_A is the mole fraction or atomic fraction of species A in the initial composition, C_0, and D_A^{Ni} is the interdiffusion coefficient of Ni and species A. The determination of these diffusivity coefficients will be discussed below.

The coefficients of interdiffusion, joint width, and composition will be used in Equation 10 to predict the isothermal solidification time.

5.8.3 Varying starting composition

Using Equation 10, the isothermal solidification time was predicted using different values of C_s and C_0. As stated earlier, this was done because the composition of the solid and liquid are not limited by low solubility of the MPD elements (Cu and Mn) as in boron containing filler metals. The C_s/C_0 couples examined in this work are $\frac{C_{SNarr}}{C_{0Ni30}}$, $\frac{C_{Sw1320}}{C_{0Ni30}}$, $\frac{C_{SNarr}}{C_{0Narr}}$, and $\frac{C_{SW1320}}{C_{0W1320}}$. Subscript "Narr" and "W" refer to a composition

measured from a narrow gap condition sample, and a wide gap condition sample respectively. A summary of C_s and C_0 values is found in Table 5.9. Varying C_s and C_0 changes the C_s/C_0 ratio and the interdiffusion coefficient. When C_S/C_0 increases, erf^{-1} (Cs/C_0) increases, and predicted t_f will decrease. The interdiffusion coefficient, $\widetilde{D}^{Ni}_{Cu\ Mn}$, is calculated using literature values and the rule of mixtures (Equation 11) of Cu and Mn. Because Mn is found to have a faster interdiffusion coefficient in Ni (compared to Cu), the calculated, $\widetilde{D}^{Ni}_{Cu\ Mn}$, will increase with increasing Mn content. Of course, as the interdiffusion rate increases, the predicted t_f will decrease. The measured Mn content of initial composition (C_0) decreases with increasing hold time, Ni30 has the highest Mn content, therefore the predicted t_f will be the lowest. C_{0W1320}, has the lowest Mn content and will therefore have the highest predicted t_f.

As shown in Figure 5.34, all values of predicted isothermal solidification time are significantly less than the experimental. Wide gap predicted t_f times range from 255 to 566 minutes, well below 1283 min determined by DSC experiments. The compositions measured from Ni30 wide gap HBJ (1320 min hold time) $\frac{C_{SW1320}}{C_{0W1320}}$, result in the longest hold time (566, and 25 minutes for wide and narrow gap conditions) due to the decreased Mn content in C_0 and lowest value of C_S/C_0.

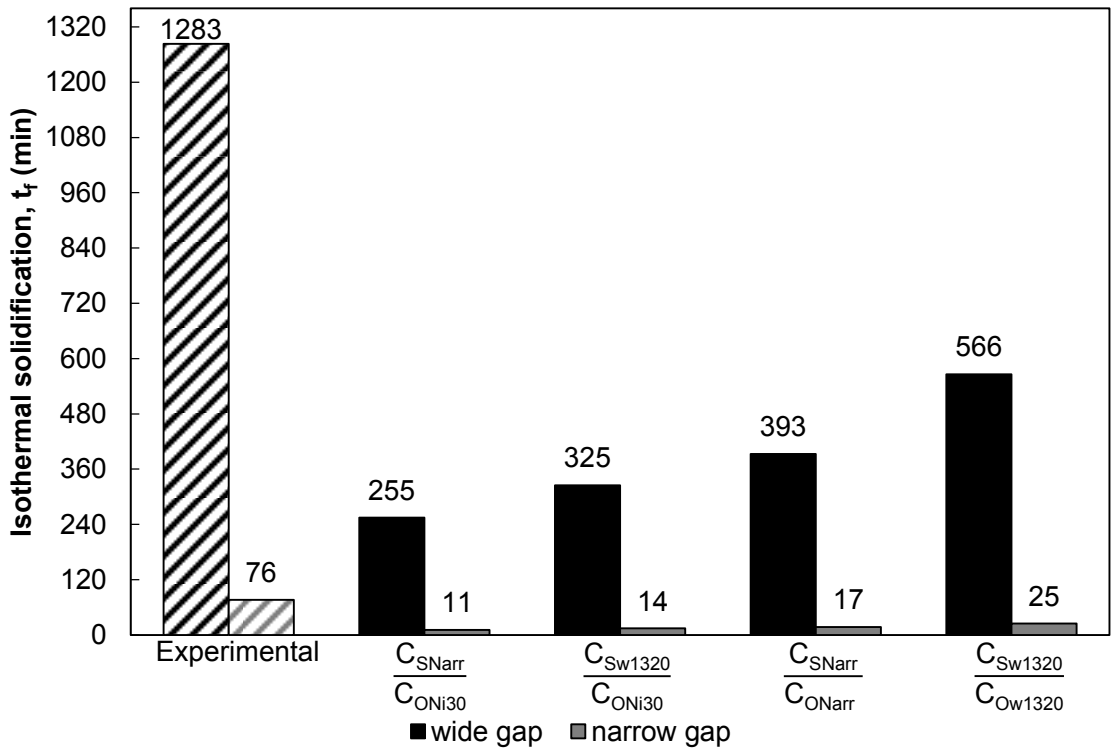

Figure 5.34 – Predicted isothermal solidification time based on model compared to experimental isothermal solidification time determined by DSC analysis for wide and narrow gap configurations. Solid bar data is predicted t_f using $\widetilde{D}$ determined by rule of mixtures.

Line scans of Ni30 HBJ (Figure 5.23) show that Mn does diffuse farther into the base metal than Cu. Cu tends to segregate to the grain boundaries in the brazed region which is to be expected based on the lower interdiffusion coefficient. Looking at the solidus diagram of Ni-Cu-Mn ternary system Figure 5.21, the combined MPD content (Cu and Mn) must decrease in weight percent by at least 15 wt% (if C_0 is Ni30) to increase T_{sol} to 1050°C. If Mn is preferentially diffusing into the solid phase the concentration of Cu and Ni in the brazed region will increase accordingly. At this point the appropriate $\widetilde{D}^{Ni}_{Cu\,Mn}$ calculated would be decreased therefore slowing down the rate of diffusion of MPD atoms into the base metal.

This analysis operates under the simplification that there is no diffusion of base metal elements into the brazed region. Experimentally, it was found that base metal

elements, primarily Cr, do diffuse into the brazed region up to 4 wt%. The presence of these elements could also slightly decrease the diffusion rate of MPD atoms which would increase the experimental time to isothermal solidification.

5.8.4 Experimental diffusivity calculation

The initial prediction model used to calculate t_f values presented in Figure 5.34 was created assuming that the binary interdiffusion coefficients and rule of mixtures was a valid way to determine the relevant theoretical Ni-Cu-Mn interdiffusion coefficient, $\widetilde{D}^{Ni}_{Cu\,Mn}$. While this assumption makes physical sense, it is a simplification of the system as explained in Section 5.8.1. To determine the interdiffusion coefficient necessary to arrive at a t_f of 1283 min (as found experimentally) Equation 10 was rearranged to form Equations 12 and 13 below:

$$\sqrt{\widetilde{D_{ex}}^{Ni}_{Cu\,Mn,}} = \frac{2w_0}{4\,\mathrm{erf}^{-1}\left(\frac{C_s}{C_0}\right) t_f{}^{\frac{1}{2}}} \tag{12}$$

$$\widetilde{D_{ex}}^{Ni}_{Cu\,Mn} = \left(\frac{2w_0}{4\,\mathrm{erf}^{-1}\left(\frac{C_s}{C_0}\right) t_f{}^{\frac{1}{2}}}\right)^{1/2} \tag{13}$$

Where $\widetilde{D_{ex}}^{Ni}_{Cu\,Mn}$, is the experimental interdiffusion rate of Ni-Cu-Mn. The results of applying Equation 13 are shown in Figure 5.35 along with the theoretical $\widetilde{D}^{Ni}_{Cu\,Mn}$ (calculated by rule of mixtures and used to determine t_f in Figure 5.34) and the binary interdiffusion coefficients from literature [63] for comparison.

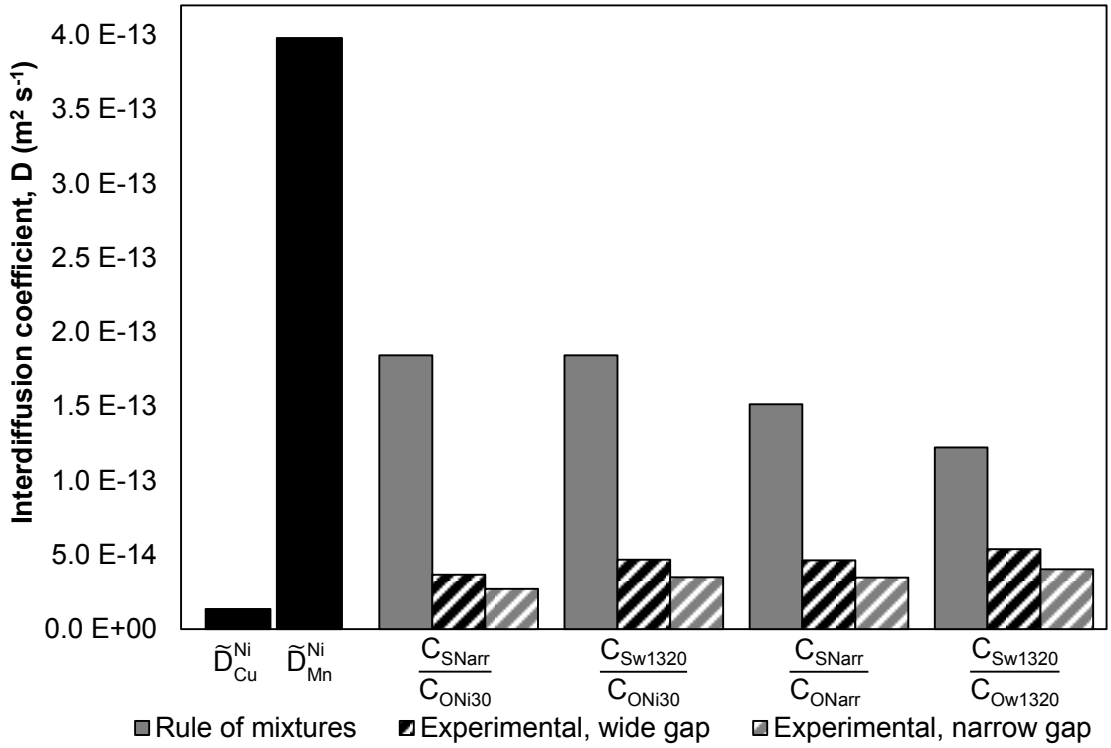

Figure 5.35 – Interdiffusion coefficients from literature [13]. Interdiffusion coefficients determined by rule of mixtures (grey data), and experimentally determined for wide gap, t_f=1283 min, and narrow gap, t_f=76 min.

As shown in Figure 5.35, the experimental interdiffusion coefficient, $\widetilde{D_{ex}}^{Ni}_{Cu\,Mn}$, is significantly lower than the theoretical $\widetilde{D}^{Ni}_{Cu\,Mn}$. It is important to note that while $\widetilde{D_{ex}}^{Ni}_{Cu\,Mn}$ are less than theoretically determined, they are similar to the interdiffusion coefficient of Ni and Cu, $\widetilde{D}^{Ni}_{Cu}$ (1.37×10^{-14}). This suggests that the diffusion coefficient of Ni-Cu-Mn and IN625 is governed more by the slower diffusing MPD element, Cu. Since the calculated interdiffusion coefficient is within the bounds of literature values for both narrow and wide gap conditions, the isothermal prediction model is determined to have good agreement with the experimental findings.

Chapter 6 Mechanical Testing of Single Lap Joints

6.1 Introduction

This Chapter evaluates the mechanical properties of both Ni30/IN625 and BNi-2/IN625 braze joints. Comparing the experimental boron free Ni30 filler metal with the widely used boron containing BNi-2 filler metal under identical conditions will be beneficial in defining applications for Ni30. The primary goal of this chapter is to determine the strength of the brazed joint through single lap joint shear testing and examine the resulting failure mode. The shear testing follows AWS C3.2M Standard Method for Evaluating the Strength of Brazed Joints [67] which is used as the industry standard for strength testing as exhibited in papers [21], [68]–[72]. AWS C3.2M standard was developed by in the 1960s after extensive research to develop a "simple and economical" test specimen. The single lap specimen was confirmed to be reliable with very little deviation across extensive data analysis and thus was chosen as the standard specimen [7]. Shear testing of single lap joints as defined by AWS C3.2 involves applying a tensile force to each end of a single lap joint machined to a dogbone shape, a schematic of the typical specimen is shown in Figure 6.1a). The single lap specimen has a bonded area between the top and bottom plates as shown in Figure 6.1b). The parameters of the single lap specimen are defined by the overlap distance (A), plate thickness (T), and gap clearance.

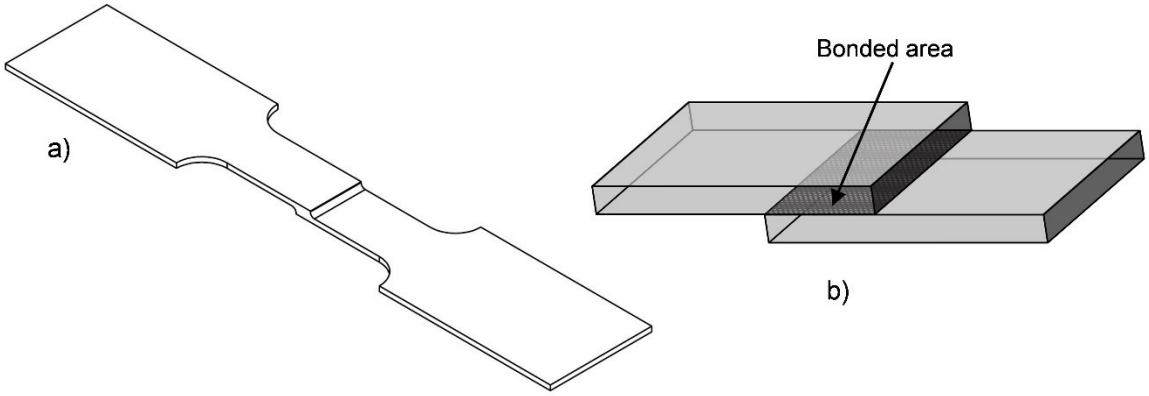

Figure 6.1 – Schematic of single lap joint specimens. a) Single lap joint dogbone shear testing specimen, b) close view of overlap region showing single lap bonded area.

The standard outlines a simple evaluation method for the data which will be explored in the following chapter. In addition, more extensive evaluation will be performed to more fully understand the performance and ultimate failure of the single lap specimens.

6.1.1 Lap joint gap wetting/filling ability

Work thus far has established that Ni30 exhibits good wetting of the IN625 surface in half braze joint experimental set ups. Wetting of the base metal by the molten filler metal is important in brazing and has an influence on the final properties of the joint. Filling a joint gap with molten filler metal by capillary action is related to base metal wetting but is not guaranteed [7]. Transient liquid phase bonding is often a capillary action process in which the filler metal is placed outside of the joint and, when molten, flows into the prepared gap [11]. The flow of molten filler metal into a joint has been experimentally determined to be affected by the capillary action driving force, viscosity and density of molten filler metal, and the geometry of the joint [7].

In modelling the complex wetting of surface by liquid, models assume the surface finish of the base metal to be flat, with surface roughness < 1 μm [11]. In

industrial TLP brazing of BNi-2/IN625 surface preparation of the BM consists of a Nicroblasting ® roughening step, and acid cleaning [21], [22]. In previous HBJ DSC work detailed in Chapter 5, the HTTAL developed surface preparation was employed on McMaster-Carr sourced IN625 plates. In this chapter, IN625 base metal provided by Pratt and Whitney Canada (Longueuil, QC) with industrial surface preparation was used to better emulate industrial conditions. Prior to shear testing, the newly developed Ni30 filler metal with IN625 base metal was evaluated to determine the ability of the Ni30 to flow into and fill a gap using both HTTAL and P&WC base metal and surface preparations. Significant differences in wetting and filling of the joint were not expected but were qualitatively evaluated.

6.1.2 Shear testing

The AWS C3.2 standard proposes evaluation of failure results based on the failure method (failure in braze joint, or base metal), calculated average shear and tensile stress at failure, and the overlap to thickness ratio. The summary chart proposed is shown in Figure 6.2. In this graph as the overlap to thickness ratio increases (A:T), the tensile stress increases and shear stress decreases accordingly. This chart is commonly used in the literature, especially in the AWS Brazing Handbook [7], when comparing different filler metal/base metal braze joints, Bredzs and Miller's examination of the AWS standard [73], and also in Chen et al.'s work examining the strength of Palnicro-36M/IN625 braze joints [21]. Palnicro-36m is a boron containing filler metal used to braze Ni-based superalloys making this work an excellent comparison for Ni30 and BNi-2 filler metals.

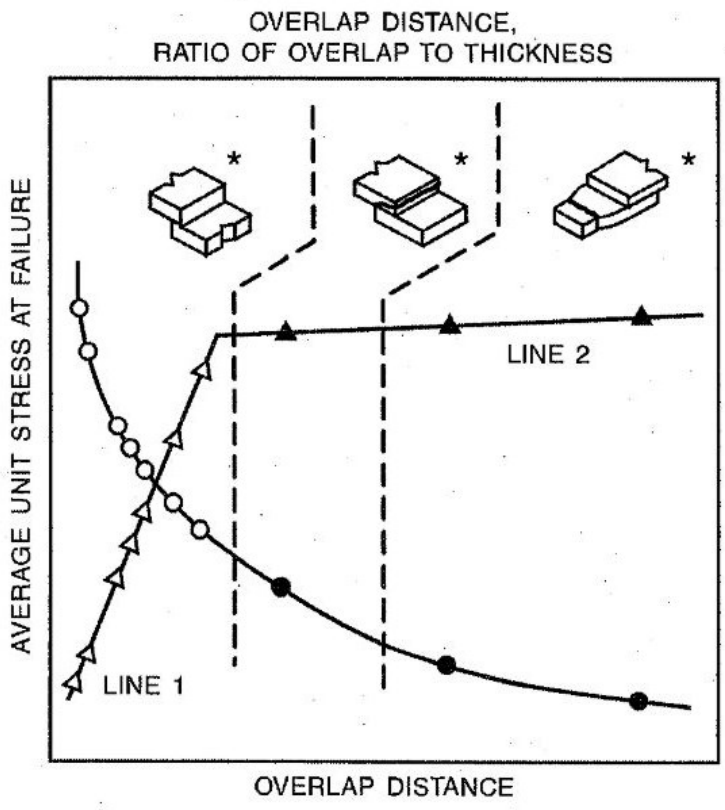

Note: Average shear stress (circles) and average tensile stress (triangles) as functions of overlap distance. Open symbols represent failure in the brazing filler metal; filled symbols represent failure in the base metal. Starred (*) illustrations show types of failures.

Figure 6.2 – Typical average stress vs overlap distance chart as described by AWS C3.2M [67].

The analysis shown in Figure 6.2 has been applied to many systems and summarized in AWS Brazing Handbook [7] which shows that between 1T and 2T the failure location generally transitions from the brazed filler metal to the base metal regardless of the filler metal-base metal alloy combination. While this trend is notable it may not apply to TLP bonded systems which, if processed correctly, should have a higher strength than a typical braze joint. Chen et al. [21] examined TLP bonded Palnicro-36M /IN625 single lap shear braze joints and found this transition to occur around 5T. Chen et al. examined overlap:thickness ratios of 1, 2, 5, 10, and 20.

Brazement design should ensure that any failure in service occurs in the base metal rather than the braze region. This can be easily accomplished in testing simply by increasing the overlap distance but, in industry, minimizing the overlap distance is preferred to avoid wasting filler metal [7].

Due to time constraints only one overlap ratio of the single lap shear joints was examined with the objective that the failure will be in the braze joint. The goal of TLPB is to create a braze joint with strength and mechanical properties similar to that of the base metal. Therefore, from a testing perspective a failure in the braze joint will allow for more information of the mechanical properties of the braze joint itself and could determine any detrimental phases in the Ni30/IN625 TLP braze joint. Based on Palnicro-36m/IN625 results by Chen et al., an overlap to thickness ratio of 3T was chosen for this work. The same overlap ratio was applied to both Ni30/IN625 and BNi-2/IN625 braze joints so that the failure strength, and failure modes could be compared.

The AWSC3.2M standard defines the average tensile strength (σ), and average shear strength (τ) as simply Equation 14 and 15 respectively:

$$\sigma_{avg} = \frac{P}{T \times W} \tag{14}$$

$$\tau_{avg} = \frac{P}{A \times W} \tag{15}$$

Where P is the fracture load, T is the plate thickness, W is the plate width, and A is the overlap distance. AWS standard assumes the braze joint experiences exclusively shear stress, and the base metal experiences exclusively tensile stress. In reality, both the base metal and braze joint experience a complex combination of tensile and shear stress distributed over the base metal and braze joint. Therefore, the calculated failure strengths proposed by AWS have theoretical, but not practical, significance. This is also true of

brazed products in service, the braze joint will not experience pure shear stress or pure tensile stress but a combination of both [7].

A significant contribution of tensile stress in the braze joint is the "twisting" or "bending" of the joint which is caused by the geometry of the single lap joint as illustrated by Bredzs and Miller [73] in Figure 6.3.

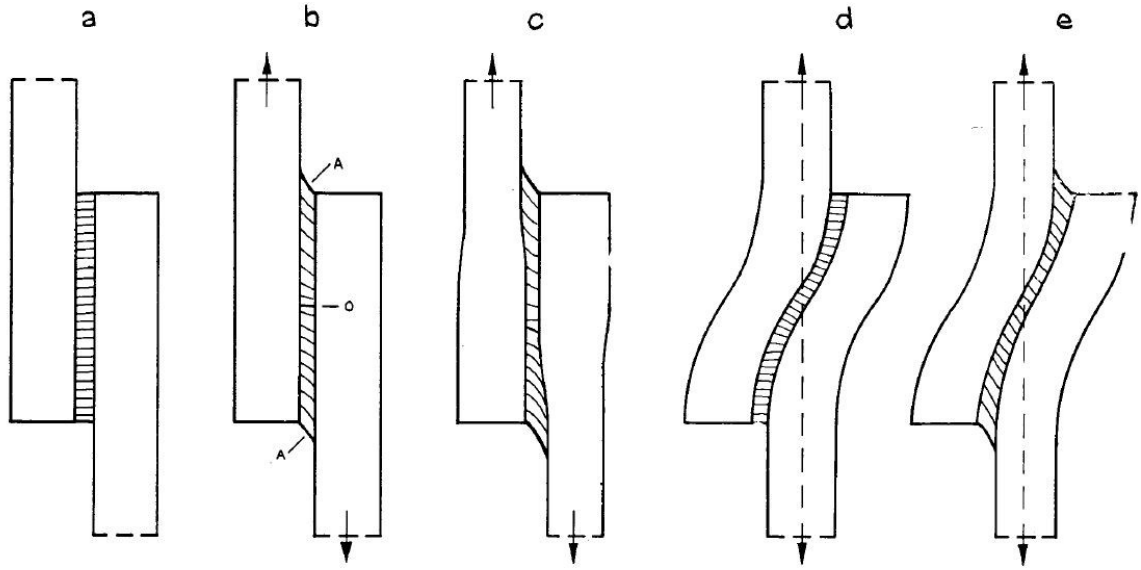

Figure 6.3 - Distortion of a brazed single lap joint during application of a tensile load in direction of arrows. a) Original configuration, no stress. B) Distortion due to elongation of base metal. C) Distortion due to base metal elongation and contraction. D) Distortion due to base metal realignment resulting in shear and tensile stress in braze joint. E) Distortion due combination of b), c), and d) as experienced in actual single lap shear specimen. [73]

Because the top and bottom base metal plates are offset from each other perpendicular to the plane of applied load, the base metal plates will realign once a tensile load is applied. This bending of the base metal causes distortion in the braze joint as well as adding a bending moment to the complex stress distribution within the base and braze metal. The AWS C3.2M standard does not consider this bending moment or any tensile contribution to the stress distribution in the braze joint. Bredzs and Miller [73] extensively examined the application of AWS C3.2M and characterized the bending

moment while using Equation 14 and 15 for analysis. Lugscheider et al. [74] examined the effect of the bending moment on the stress distribution within the braze joint, shown in Figure 6.4.

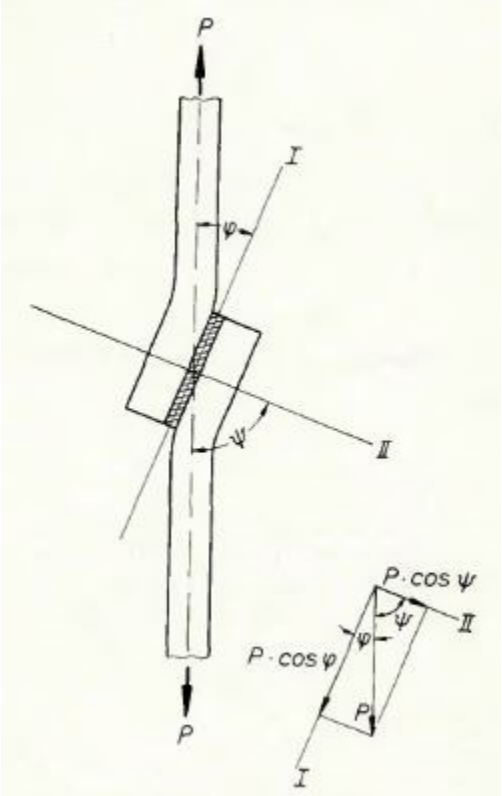

Figure 6.4 - Distribution of load within braze joint in single lap shear specimen after alignment of base metal [74].

Lugscheider et al. applied von Mises criterion to calculate an equivalent shear stress, σ_e. Equivalent shear stress is defined as below [74]:

$$\sigma_e^2 = \frac{1}{2}[(\sigma_I - \sigma_{III})^2 + (\sigma_{II} - \sigma_I)^2 + (\sigma_{III} - \sigma_{II})^2] \quad (16)$$

Where σ_I, σ_{II}, and σ_{III} are the principle tensile stresses according to Figure 6.4. Lugscheider sets $\sigma_{III}=0$, i.e. the principle stress in direction III (across width of the lap joint), assuming the deformation and stress in this direction is negligible. The remaining principle stresses can be described as below:

$$\sigma_I = p \cdot cos\varphi \tag{17}$$

$$\sigma_{II} = p \cdot sin\varphi = \sigma \tag{18}$$

Where φ is the bending angle of the base metal from the vertical. Using Equations 17 and 18, Equation 16 can be expressed as in [74], defining the ratio of equivalent stress (von Mises) to tensile stress as:

$$\frac{\sigma_e}{\sigma} = \sqrt{1 - sin\varphi \cdot cos\varphi} \tag{19}$$

Figure 6.5 compares the newly defined σ_e to average σ and τ. A larger bending angle (measured at 1T in this case) will decrease the actual stress in the filler metal with maximum von Mises stress at 45° bending angle.

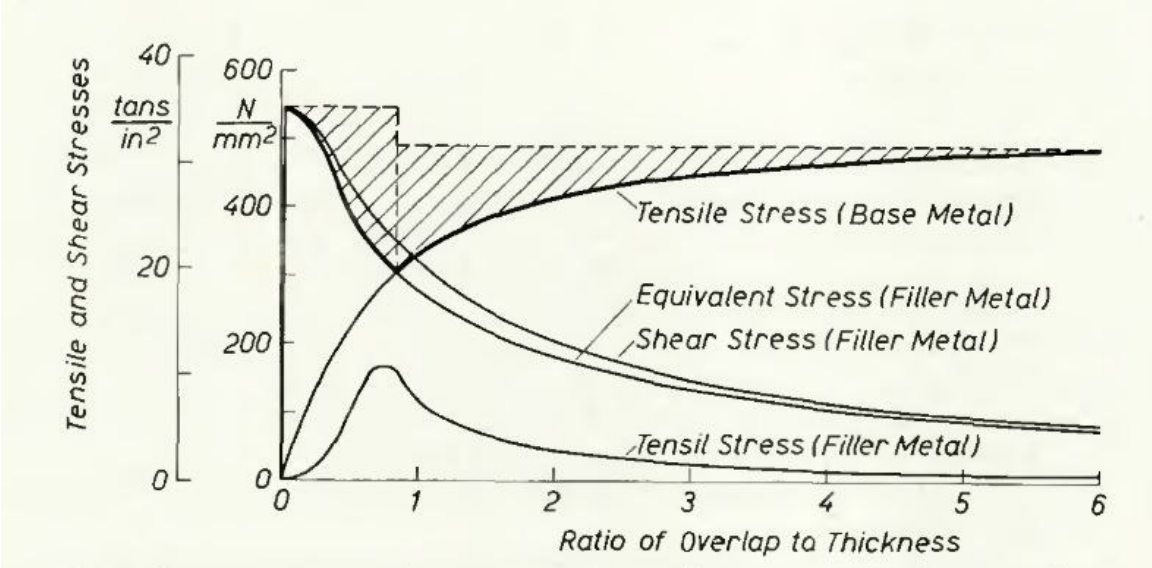

Figure 6.5 – Comparison of shear, tensile, and equivalent stress vs overlap to thickness ratio calculated for a 316SS/BNi-2 single lap joint [74].

Lugscheider's approach has been used as the basis of Flom and Wang's work [71], [72] on flaw tolerance in lap shear brazed joints. Flom and Wang used von Mises criterion to create a finite element analysis (FEA) model used to calculate the distribution of stress within the lap joint using base metal 347 stainless steel and pure silver filler metal. The FEA results in Figure 6.6 show that the von Mises stress at the openings of the

overlap is significantly higher than the centre of the joint. This is due to the peeling force caused by bending angle and the deformation of the base metal in this area. This stress distribution agrees well with work theorized by Bredzs and Miller [73] over three decades earlier without the use of FEA. Additionally, at a low overlap ratio the stress distribution is uniform along the joint due to the small angle of bending in low overlap single lap joints. The disparity between centre and edge stress becomes greater with increasing overlap ratio due to the large bending angle and peeling force. It should be noted that all braze joints in Figure 6.6 (0.5-5T overlap) failed in the filler metal [71].

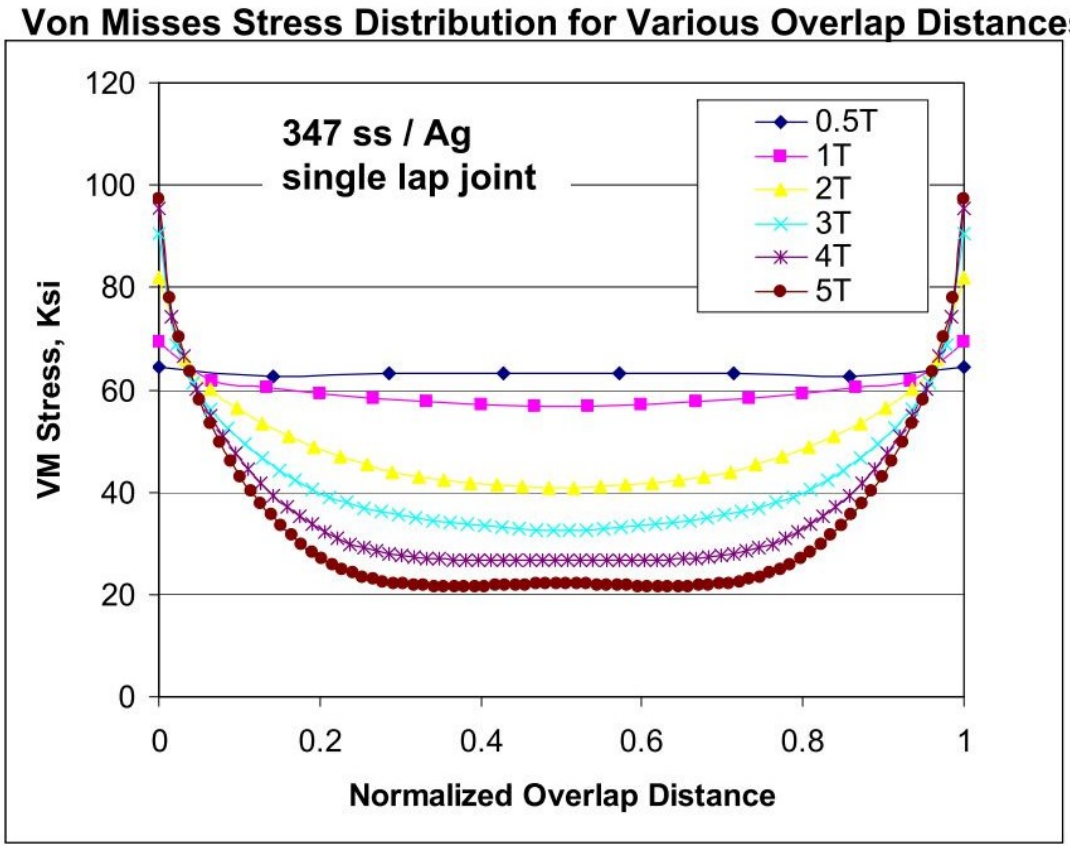

Figure 6.6 - Von Mises stress distribution of 347SS/Ag single lap joint calculated by FEA for shear testing. [72]

Riggs et al. [70] used digital image correlation (DIC) to experimentally validate this complex stress distribution along the joint in an single crystal Ni alloy CMSX-4 base

metal and BNi-2 filler metal. The DIC method uses high accuracy optical analysis of the lap joint surface to measure displacement of a randomized speckle pattern during the shear test [70]. A sample of DIC images comparing the strain distribution of 1T and 4T is shown in Figure 6.7. The high strain (and corresponding deformation and stress) at the overlap ends is visible as well as the strain distribution in the base metal surrounding the lap joint. This analysis confirmed the same stress distribution modelled by Flom and Wang [72] and theorized by Bredsz and Miller [73].

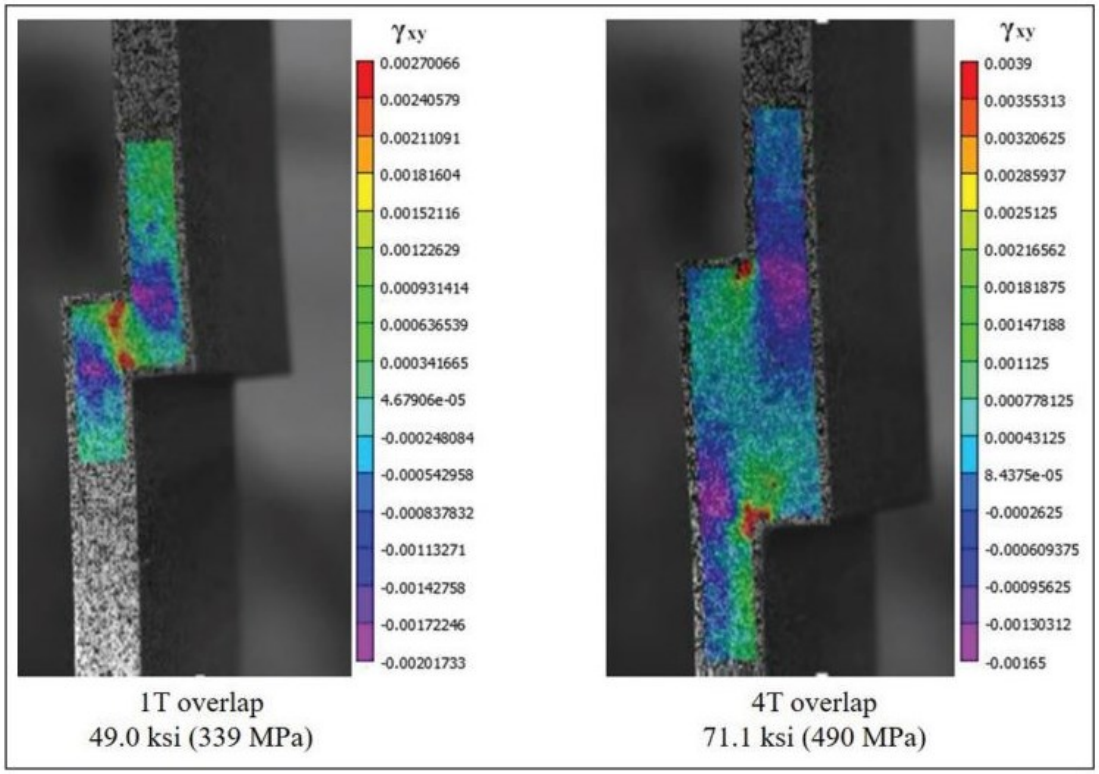

Figure 6.7 – 3D-DIC images of CMSX-4l/BNi-2 lap joints showing shear strain distribution in overlap region just before failure [70].

While FEA and DIC methods are outside the scope of this work, the findings of previously mentioned references (notably Figure 6.6 and Figure 6.7) will contribute to the understanding of the stress distribution within the braze joint. This will help to explain the failure in experimental IN625/Ni30 and IN625/BNi-2 single lap braze joints.

6.2 Experimental Methods

6.2.1 Materials

Three types of IN625 base metal were used: IN625 purchased from McMaster-Carr in both 1/24" (~1 mm) thick and 1/8" (3.2 mm) thick plates, and IN625 plate received from Pratt and Whitney Canada (Longueuil, QC) in 1.2 mm thick plate. The McMaster-Carr purchased IN625 plate was prepared according to HTTAL developed surface preparation standard (grind with 500 grit Si-C paper, ultrasonic clean, rinse in acetone). Both plates of Pratt and Whitney Canada IN625 were acid cleaned and Nicroblasted ® (typical surface preparation) prior to receiving at Dalhousie. The filler metals used were Ni30 (characterized earlier in this thesis), and BNi-2 powder. The spherical BNi-2 metallic powder (Ni-3.0Fe-7.0 Cr-4.5Si-3.2B) had a d_{50} 45 μm diameter and was purchased from Nickebraze.

Lap joint specimens were prepared according to AWS C3.2M standard by clamping a 50 μm stainless steel spacer between the surface prepared plates. While clamped, small (1/24" diameter) 316 stainless steel tacks were spot welded using a HotSpot II Thermocouple welder outfitted with a copper electrode. The steel tacks were welded to the front and back of the lap joint as shown in Figure 6.8. The tack welds were used to maintain the brazing gap (50 μm) and overlap distance (A) throughout the brazing process and were removed prior to mechanical testing. An example of tack welded braze joint is included in Figure 6.9 showing the overlap distance. The spacer was removed from the lap joint leaving a 50 μm gap between plates (full gap width). As part of process validation, the gap clearance and overlap distance were confirmed by microscopic analysis for each lap joint. During preliminary brazing it was found that

Ni30 and BNi-2 filler metals did partially wet the 316SS tacks but no significant interaction with the 316SS tacks was found.

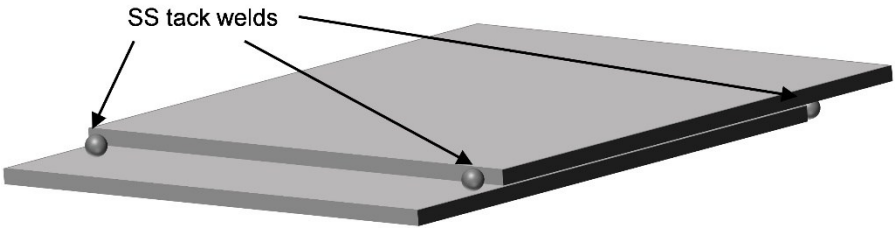

Figure 6.8 – Schematic of stainless steel tack weld locations on gap filling test specimens.

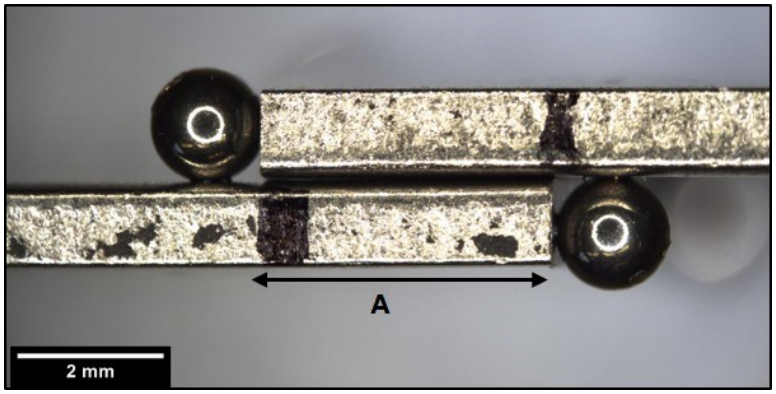

Figure 6.9 – Side view of single lap joint overlap region, A is the overlap distance.

Filler metal powder (BNi-2 or Ni30) was placed outside the gap clearance at the "front" of the joint as shown in Figure 6.10. The filler metal was mounded along the width of the IN625 plate as evenly as possible. In an effort to create a fillet at the front and back of the lap joint, Y_2O_3 "stop-off" was painted on the IN625 plate to encourage fillet formation and discourage spreading of filler metal.

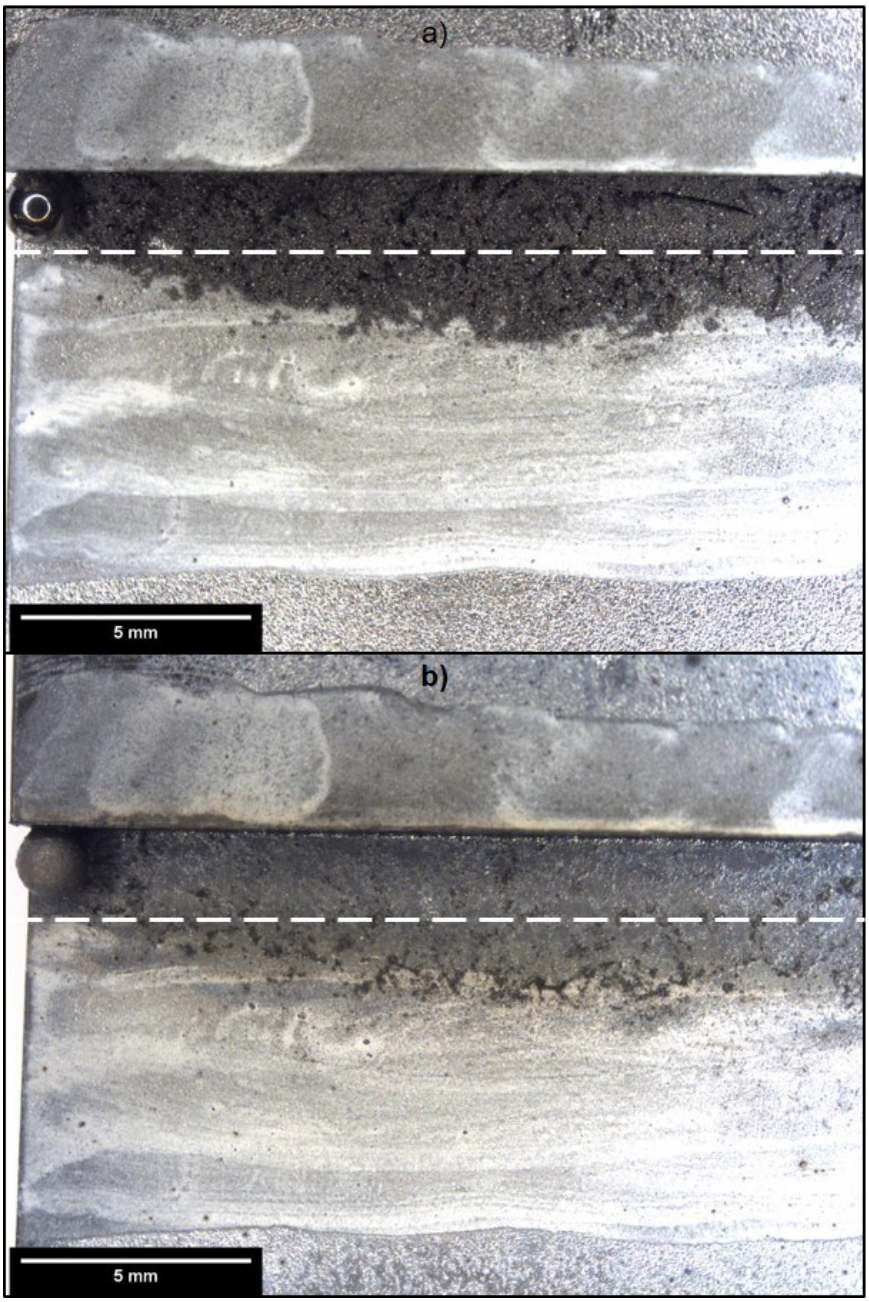

Figure 6.10 – Top view of single lap braze joint at the "front" of joint a) pre-brazing, and b) post brazing. Dashed line shows position of Y_2O_3 stop-off compound painted on base metal prior to Ni30 powder placement.

Prior to shear testing, three trials of lap joints were examined, a common goal through these trials was to determine the correct mass of filler metal which would create a fully filled joint with fillets at front and back of the joint. To determine this value, the ratio of filler metal mass (mg) to overlap distance (mm) was tracked. Trial 1 examined

the gap filling ability of Ni30 using a large overlap distance of 20 mm and 220 mg (11 mg/mm) of Ni30 filler metal powder. McMaster-Carr sourced IN625 1 mm thick plate was used for Trial 1. These samples were examined for gap filling ability, and SEM-EDS elemental analysis of the lap joint. Trial 2 examined the gap filling ability of lap joints using different sources of base metal, McMaster-Carr (1 mm thick) and P&WC (1.2 mm thick). These specimens had an overlap distance of ~3.2 mm, and 82 to 84 mg of Ni30 powder (~26 mg/mm). Trial 3 focussed on fillet creation using P&WC IN625 plates, increasing the overlap distance to 5 mm, and filler metal powder mass to 250 mg (50 mg/mm).

Shear testing specimens were created using 1.2 mm P&WC IN625 plate with a 3.6 mm overlap distance (3T), and 250 mg of filler metal powder (69 mg/mm). Once brazed, the single lap joint specimens were wire EDM machined into a dogbone shape. The EDM fluid used was composed of water, WD-40, and EDM V (a corrosion inhibitor produced by Commonwealth Oil [75]). A schematic of the machined lap joint specimen is shown in Figure 6.1a) and specifications are found in the Appendix, Figure C.2. The ratio of overlap to thickness ratio was chosen to be 3T for all single lap shear test specimens examined as explained in Section 6.1.2. Three shear testing specimens of each filler metal were tested.

IN625 monolithic single lap joints were wire electrical discharge machined (EDM) from McMaster-Carr 1/8” thick plate to simulate a single lap joint composed of solid IN625 (i.e. no braze joint). This specimen type was created to compare the mechanical properties of brazed single lap joints to IN625 with the same geometry. Dimensions of the monolithic specimens are included in the Appendix, Figure C.1. The

IN625 monolithic specimens were subjected to identical thermal profile as the brazed specimens prior to machining. Four IN625 monolithic samples were tested. Difficulties in machining caused vibration of the IN625 plate. As a result of this vibration, the plate thickness in the specimen gauge ranged from 1.15 to 1.32 mm

6.2.2 Brazing furnace set up

All lap joints, gap filling samples and single lap shear test specimens, were brazed in a Sentrotech high temperature tube furnace under high purity (99.999%) flowing argon gas at 5 L/min. The brazing furnace is equipped with a 34" length alumina tube with inner diameter of 3". Set up of braze joint specimens in the brazing furnace is shown in Figure 6.11.

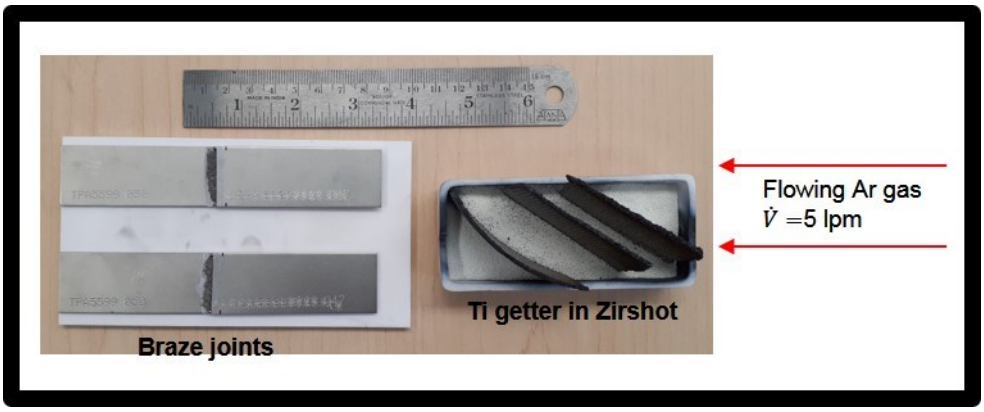

Figure 6.11 –Internal set up of Sentrotech brazing furnace.

The furnace was evacuated twice and back filled with high purity Ar gas prior to the furnace run. The O_2 level of the furnace was measured using an Alpha Omega O_2 sensor which analysed the outlet gas of the furnace. The O_2 content of the brazing furnace gas was measured to be <5 ppm when flowing 1.5 L/min of Ar (maximum flow of O_2 sensor) through the empty furnace over a period of 250 minutes. A graph of the measured O_2 content is included in the Appendix. The O_2 level of the brazing furnace under experimental conditions (5 L/min) was not able to be measured because of limitations in

the flow rate that the O_2 sensor could experience. Measuring the O_2 content at a lower flow rate and lower temperature represents a worse case scenario of the furnace. The higher temperature and higher Ar flow rate is assumed to decrease the O_2 content of the furnace. For this reason, the atmosphere of the Sentrotech furnace was deemed to be suitable for TLPB of Ni superalloys in this work. To further reduce the oxygen concentration in the furnace, a Ti getter was placed in the furnace between the Ar flow inlet and the brazing samples as shown in Figure 6.11.

All single lap specimens (Ni30/IN625, BNi-2/IN625, and monolithic IN625) were heated to 1050 °C and held for 30 minutes. The thermal profile is shown in Figure 6.12. The brazing furnace used has a maximum heating and cooling rate of 5 °C/min (kpm), significantly less than the heating rate used in DSC experiments (20 kpm). On cooling, the furnace maintains 5 °C/min cooling until approximately 620 °C at which point the cooling rate slows to furnace cooling decreasing from 5 to eventually 0.5 °C/min. DSC experiments have confirmed no relevant phase transformation occurs below 600 °C. Because of this, the thermal profile was determined to have no adverse effect on the brazing quality of the Ni30/IN625 or BNi-2/IN625 lap joints.

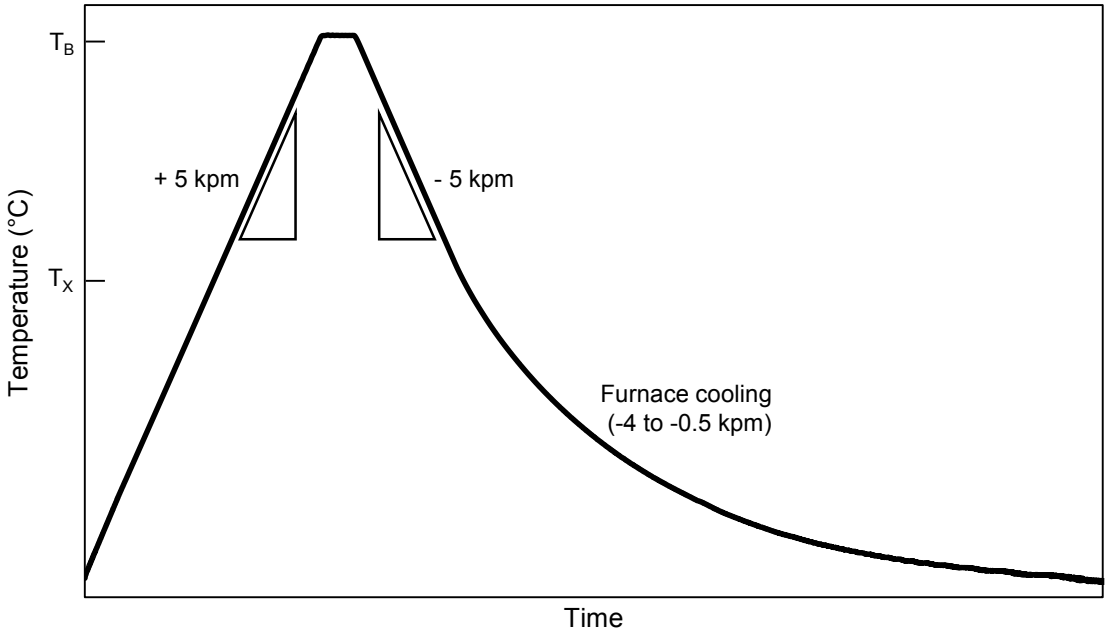

Figure 6.12 – Thermal profile of Sentrotech brazing furnace for lap joint specimens. T_B is the brazing temperature of 1050°C, T_X is ~620 °C, the temperature at which the cooling rate deviates from 5 kpm and furnace cooling occurs.

An important aspect of the thermal profile is the time above solidus which dictates the isothermal solidification of the filler metal in the braze joint. The solidus of Ni30 has been confirmed in prior work to be 900 °C which, in the lap joint thermal profile, translates to 64 minutes above solidus (liquid duration). The T_{sol} of BNi-2 is 870 °C translating 70 minutes above solidus (liquid duration). Work by Moreau and Corbin [56] defining the MBC relationship in IN625/BNi-2 indicates that 70 minute liquid duration (8.37 $min^{1/2}$) allows for a maximum brazing clearance ($2w_{ISZ}$) of 60-70 μm (greater than the gap clearance of 50 μm used in this work). In Figure 5.30 of Section 5.7.2, the MBC relationship of Ni30/IN625 braze joint indicates that at a liquid duration of 64 min (8.0 $min^{1/2}$) the width of ISZ was found to be 150 to 194 μm. Therefore, the thermal profile, Figure 6.12, used to braze lap joint specimens should allow for complete isothermal solidification of both BNi-2/IN625 and Ni30/IN625 braze joints.

6.2.3 DSC analysis of remelted lap joint

Lap joints prepared and brazed in Trial 1 (20 mm overlap distance) were sectioned into small DSC sized lap joints and heated in the DSC to determine the remelt temperature of the brazed region. Two small lap joint sections (3 x 3 mm and 2.2 mm in height) cut from section A and C (Figure 6.13) were examined.

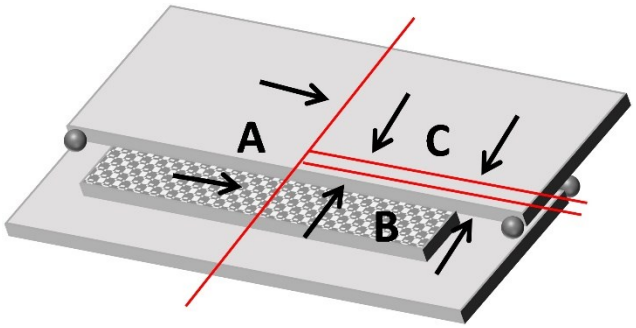

Figure 6.13 – Schematic of sectioning locations for metallographic preparation of single lap joints.

The sectioned lap joints were positioned in the alumina DSC crucible so the bottom IN625 plate was in contact with the bottom of the crucible as shown in Figure 6.14. Sections of the IN625 plate without FM interaction were cut to the same dimensions and heated in the DSC to be used as a correction file for the lap joint remelt traces.

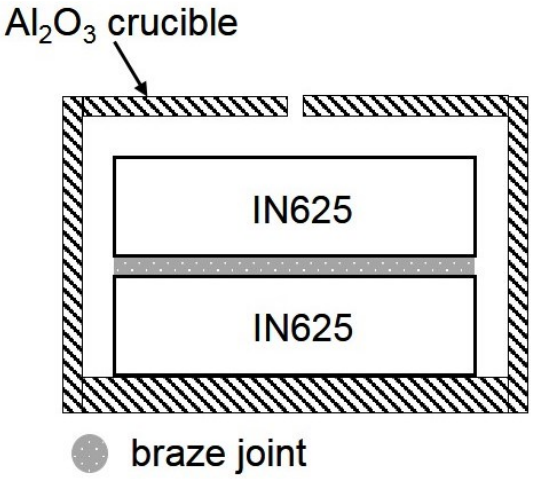

Figure 6.14 – Set up of DSC Al_2O_3 crucible for lap joint remelt tests.

6.2.4 Shear testing and fracture analysis

Shear testing was performed on three samples each of BNi-2 and Ni30 brazed single lap joint specimens and four samples of monolithic IN625 simulated single lap specimens. In this work shear samples brazed with BNi-2 will be referred to as B1, B2, B3, samples brazed with Ni30 will be N1, N2, N3 and monolithic IN625 samples will be M1, M2, M3, M4. Testing was conducted using an Instron® 5594-200HVL load frame with a 50 kN hydraulic load cell as shown in Figure 6.15. The Instron load frame was equipped with wedge type grips with serrated gripping area. The targeted strain rate for all testing was 5 MPa/s. An Epsilon technologies 3542 axial extensometer (gauge length 25 mm) was used to measure engineering strain.

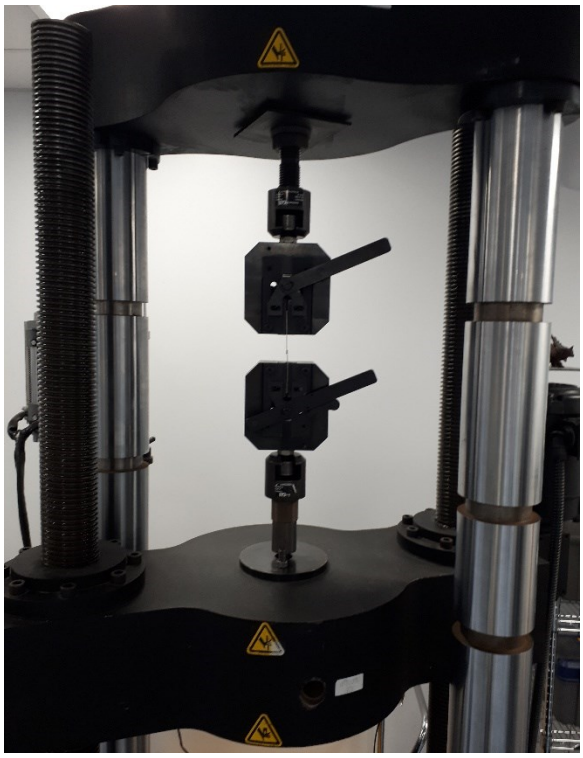

Figure 6.15 – Instron load frame used for shear testing of single lap test specimens.

Video of each shear test was recorded on a Samsung A5 2017 Android smartphone at a frame rate of 30 fps. Stills were extracted from the video and used for qualitative analysis.

Sample dimensions (width and thickness) were recorded at five points along the sample gauge length prior to and post testing to record any dimensional changes. Locations (a to e) shown in Figure 6.16 were chosen to analyse dimensional changes in the base metal and the overlapped region. Also shown in Figure 6.16 is the definition of side A1 and A2. Video of the shear testing was taken such that side A2 was visible.

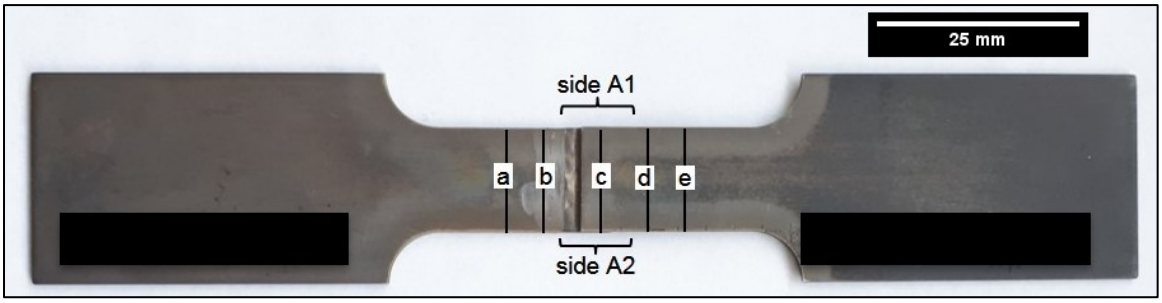

Figure 6.16 – Single lap shear test specimen prior to testing showing location of named features used later in the work.

Failure analysis was performed on fracture surfaces, and polished cross sections of fractured surfaces using optical microscopy and SEM.

6.3 Results and Discussion

6.3.1 Gap filling ability of Ni30/IN625

Preliminary gap filling tests using McMaster-Carr base metal (Trial 1) showed excellent filling of the 50 μm gap. Images of the lap joint specimens before and after brazing are shown in Figure 6.10. Joints examined macroscopically confirmed that the Ni30 filler metal fully melted, flowed into the gap, and filled the 50 μm gap to the back and both sides. The samples were sectioned according to Figure 6.13 to confirm that the

gap was fully filled and perform elemental EDS. The microstructure of the lap joint was consistent with those found in DSC HBJ samples with a noted segregated region (S), solid solution matrix, and narrow DAZ with small precipitates concentrated at the grain boundaries. Qualitatively, the volume fraction of the S phase (confirmed to be the ASZ in some samples) was noted to be significantly less than that found in DSC HBJ samples confirmed to have achieved full isothermal solidification.

Optical microscopy performed on samples located at Section A, B, and C were used to quantify the gap filling of Trial 1 lap joints. A joined gap indicates a joint with minor porosity, non-wetted gap indicates that both the top and bottom plates were wetted but a large portion of the gap is not filled, and non-wetted indicates that the plates were not-wetted by the filler metal. A total of 33.37 mm of Trial 1 lap joint was examined, with 75 % joined, 15% wetted, and 10% not wetted. The not wetted section was determined to be caused by insufficient mass of powder (11 mg/mm) and was thus increased in Trial 2 lap joint specimens.

Lap joints prepared for Trial 2 (A=3.2 mm) compared IN625 sourced through McMaster-Carr and P&WC. Lap joints were sectioned and examined by optical microscopy to determine level of wetting. With the increase of filler metal mass to overlap distance ratio to 25 mg/mm all regions examined were found to be joined or wetted. No regions of non-wetted plates were identified. Regions of porosity (wetted but not filled joints) were identified, and no fillets were created. For these reasons the ratio of filler metal powder to overlap distance was again increased in Trial 3 lap joints. Trial 3 lap joints used 45 to 50 mg/mm Ni30 powder and created fillets with a radius of ~1 mm at the front and back of the sample.

6.3.2 Isothermal solidification of lap joint specimens

Elemental analysis by EDS was performed to confirm that the specimen had undergone isothermal solidification. EDS line scans taken at section A (near the joint front) and section C (back of joint) are shown in Figure 6.17 with accompanying SEM micrographs showing location in Figure 6.18. Line scans were performed at two locations to determine if the proximity to the initial placement of the FM influences the composition of the braze joint. As shown in Figure 6.17, the composition of the brazed region in both locations is very similar indicating that proximity is not a factor in composition. The braze thickness at the line scan location was determined to be 52 µm, with a measured DAZ of approximately 15 to 20 µm. As found in HBJ samples, the Cr content in the braze joint is between 4 and 5 wt% indicating similar levels of BM dissolution into the braze region have occurred.

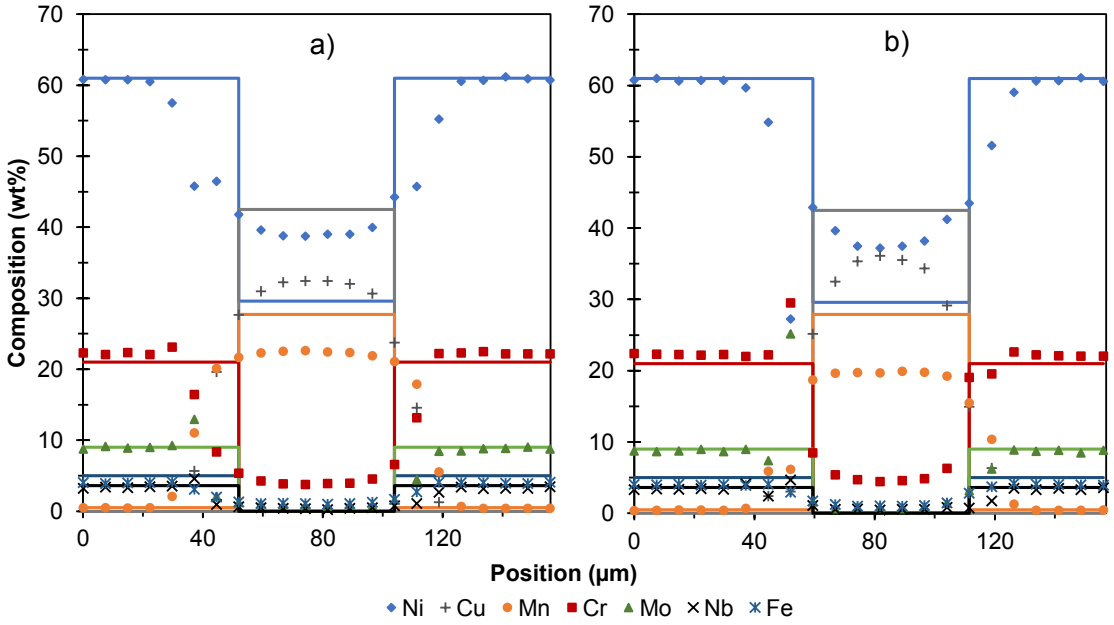

Figure 6.17 – Elemental composition measured by EDS across the Ni30/IN625 single lap joint of section a)A and b)C. Solid lines indicate initial composition of either Ni30 or IN625. SEM micrographs included in Figure 6.18.

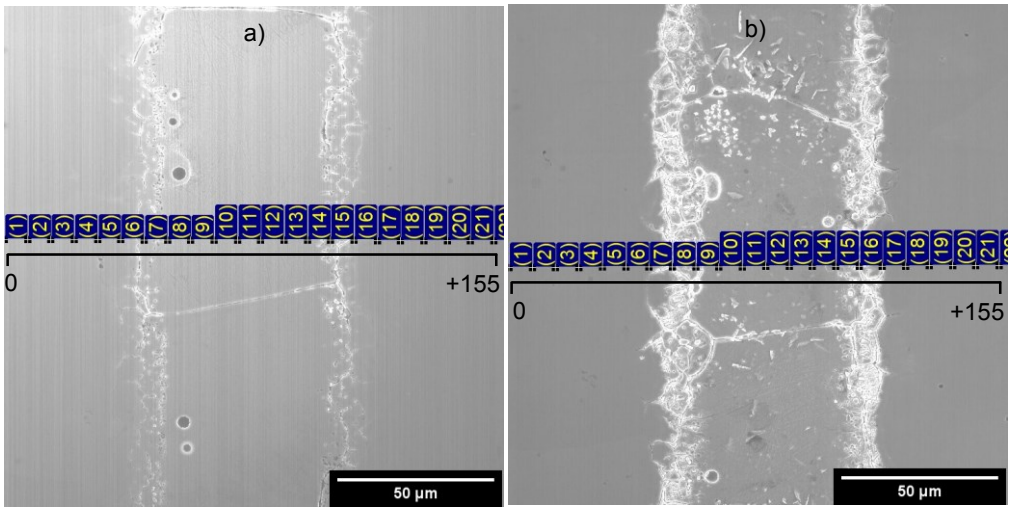

Figure 6.18 – SEM micrographs of Ni30/IN625 single lap joint specimen showing location of EDS point scans in Figure 6.17a) and b).

The T_{sol} of each location (A and C) was calculated using Thermo-Calc and is presented in Table 6.1. The calculated T_{sol} being above 1050 °C indicates that the braze joint has undergone complete IS.

Table 6.1 – Composition measured by EDS of lap joint features and melting range calculated using Thermo-Calc.

				Composition (wt%)						
Section and Feature		T_{sol} (°C)	T_{liq} (°C)	Cr	Mn	Fe	Ni	Cu	Nb	Mo
A	Braze (line of points)	1083.5	1122.6	4.1	22.4	1.1	39.3	31.8	0.4	0.9
	Fillet (box scan)	1037.6	1068.0	2.0	26.4	0.6	31.1	39.8	0.0	0.0
C	Braze (box scan)	1093.3	1135.5	4.9	19.6	1.1	38.2	34.9	0.5	0.8

Samples of the lap joints were subjected to remelting in DSC to determine the remelt temperature of the braze joint. The resulting DSC traces on heating to 1200 °C using a IN625 plate trace subtraction are shown in Figure 6.19. The T_{sol} of the remelted lap joint braze region was measured to be 1063.3 and 1065.3 °C and since this is greater than 1050 °C, it can be concluded that a Ni30 lap joint with 50 µm gap clearance does undergo full isothermal solidification with a 30 minute hold at 1050 °C (equivalent to a liquid duration of 64 minutes). This is consistent with the MBC predictions of Figure

5.30 where the gap size of 150 to 194 μm would have undergone complete IS in 64 minutes. As found in Section 5.1 Thermo-Calc calculated T_{sol} is slightly overestimated when compared with DSC remelt data and this overestimate is also seen from Table 6.1 data.

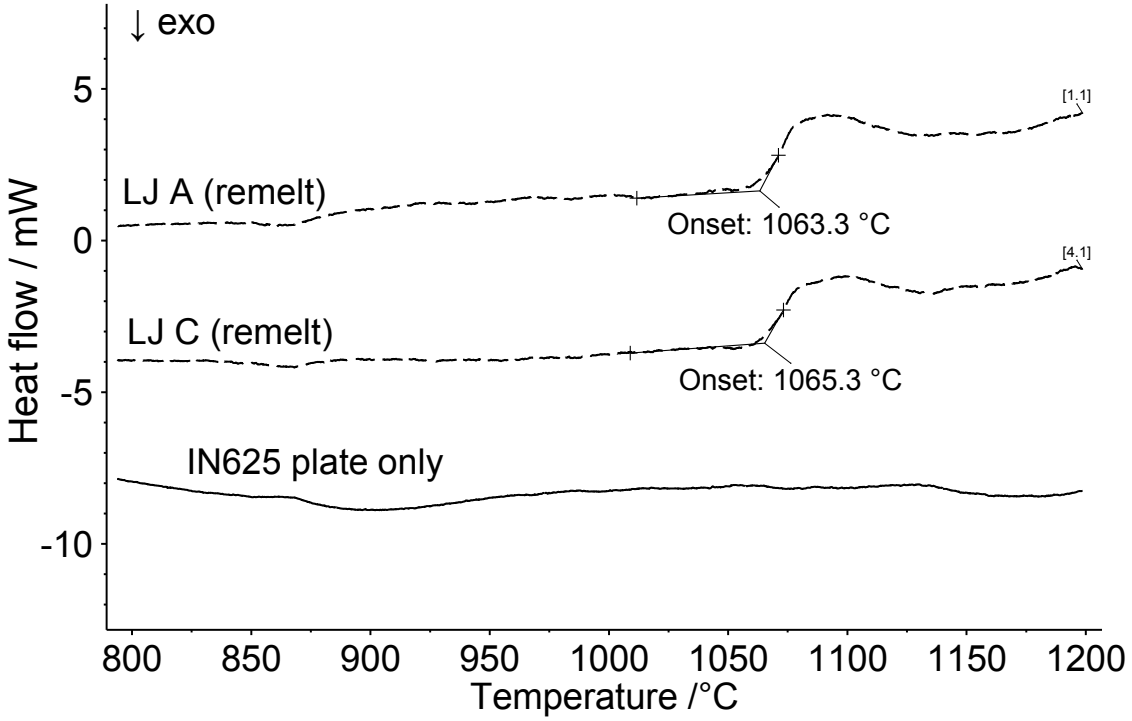

Figure 6.19 – DSC trace of single lap joint remelted after brazing. Lap joint (LJ) at section A, and C, using IN625 plate only DSC trace as subtraction. Heat flow units are in mW because IN625 correction file was used.

Optical analysis of the fillet region of Ni30/IN625, showed a much higher fraction of the S region. The elemental composition of this fillet as presented in Table 6.1, determined by EDS analysis of a large (300 μm) box scan of the region, resulted in a composition very similar to Ni30 indicating very little interaction with the base metal occurred. This is to be expected as the fillet region can be thought of as a Ni30/IN625 half braze joint of thickness ~200 μm, and full braze joint thickness of ~400 μm. As stated above, the MBC plot (Figure 5.30) indicate a maximum brazing clearance of 150

to 194 μm for 64 minute liquid duration, much smaller than 400 μm, resulting in a mostly liquid fillet region on cooling. The T_{sol} calculated by Thermo-Calc was 1037.6 °C, further confirming that the fillet region has not undergone isothermal solidification.

6.3.3 Microstructural analysis of single lap shear specimens

Figure 6.20 shows an example of Ni30/IN625 and BNi-2/IN625 lap joint shear specimens before and after brazing. The location of the filler metal powder is considered to be the "front" of the joint. In both cases, the filler metal filled the gap fully to the back of the joint where a small fillet was visible. Surface oxidation of IN625 base metal was identified on both samples (more prevalent on the BNi-2 brazed samples due to location in furnace). The joints were carefully examined macroscopically and determined that the oxidation did not have an effect on the gap filling ability of the filler metal.

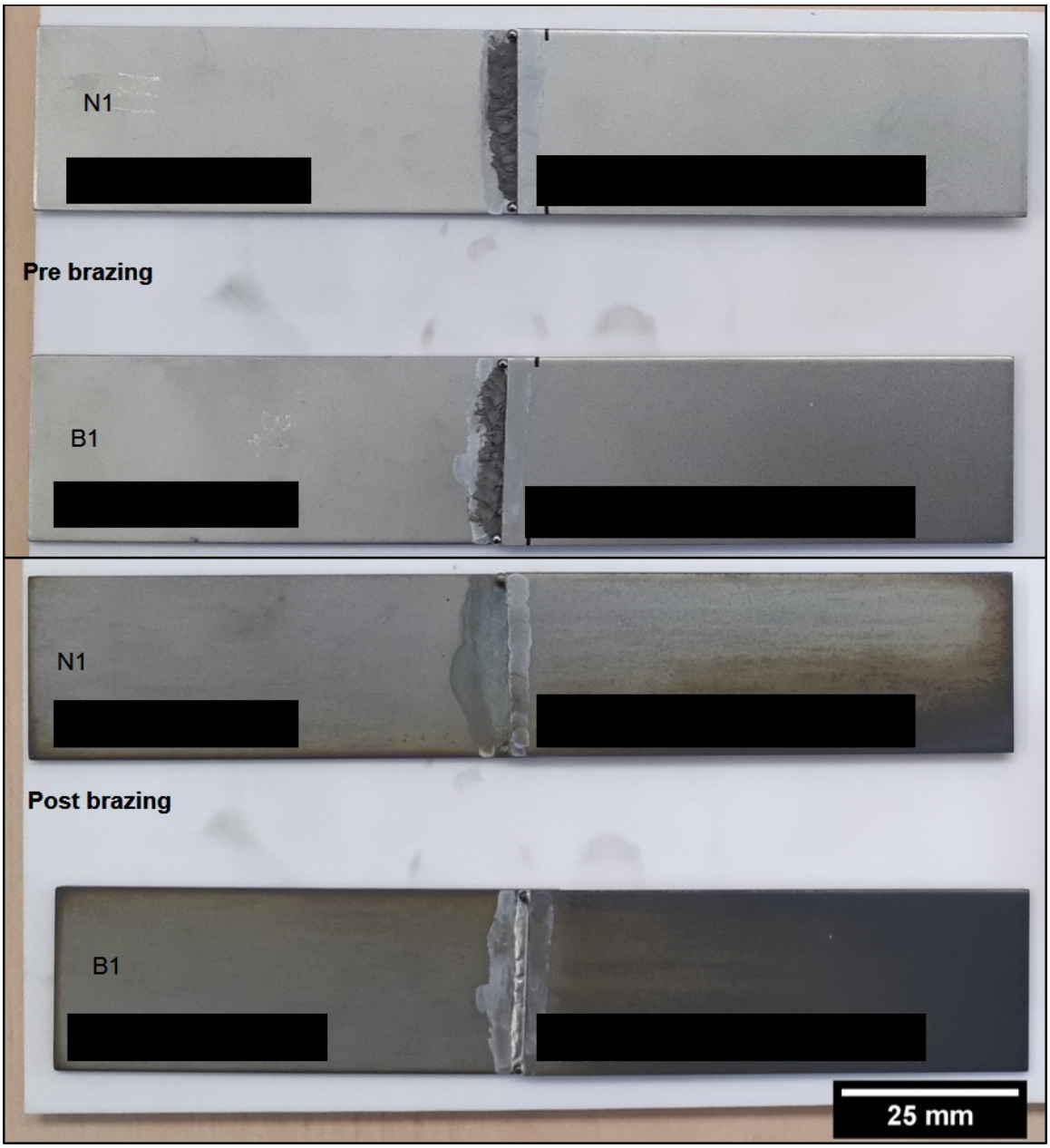

Figure 6.20 – Ni30/IN625 (N1) and BNi-2/IN625 (B1) single lap shear test specimens pre and post brazing. Some oxidation occurred during brazing process. Black bars cover Pratt and Whitney Canada identifying production codes.

Figure 6.21 shows the shear test specimens after machining to the dogbone shape (specified in the Appendix Figure C.2) by wire EDM.

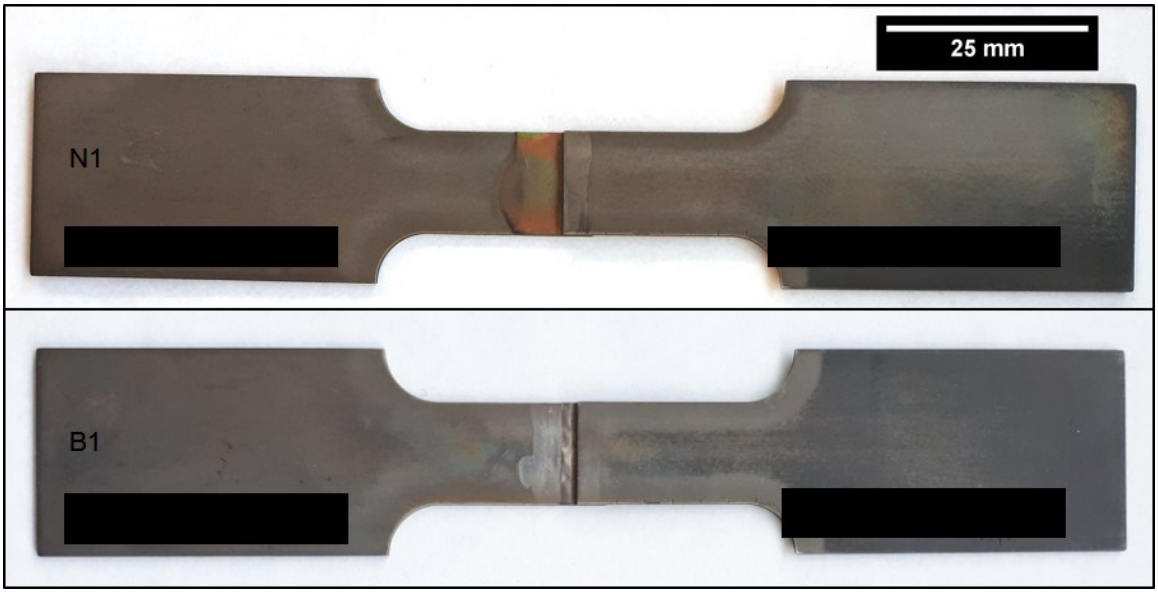

Figure 6.21 – Ni30/IN625 (N1) and BNi-2/IN625 (B1) single lap shear joints after machining by wire EDM according to specifications in Appendix Figure C.2. Black bars cover Pratt and Whitney Canada identifying production codes.

The scrap of the lap joint (sides removed by EDM) were polished for microstructural analysis. This allows for examination of the entire 3.6 mm overlap distance and direct comparison with the fractured samples as shown in Figure 6.22 for shear specimens N1 and B1. Small areas of porosity are noted in the Ni30/IN625 specimens (Figure 6.22C), concentrated around the middle of the overlap. In samples where porosity was present, the base metal was wetted in these locations indicating that the porosity was due to solidification of the braze metal, or insufficient volume of filler metal. Porosity was present to a lesser extent in the BNi-2/IN625 specimens, appearing as small circular pores within the overlap. Figure 6.22 d) and e) show the presence of ASZ phases in the fillet region of both Ni30 and BNi-2 brazed lap joints respectively. The ASZ is the microsegregated S region in Ni30 braze joint, Figure 6.22d), and ternary eutectic borides in the BNi-2 braze joint, Figure 6.22e).

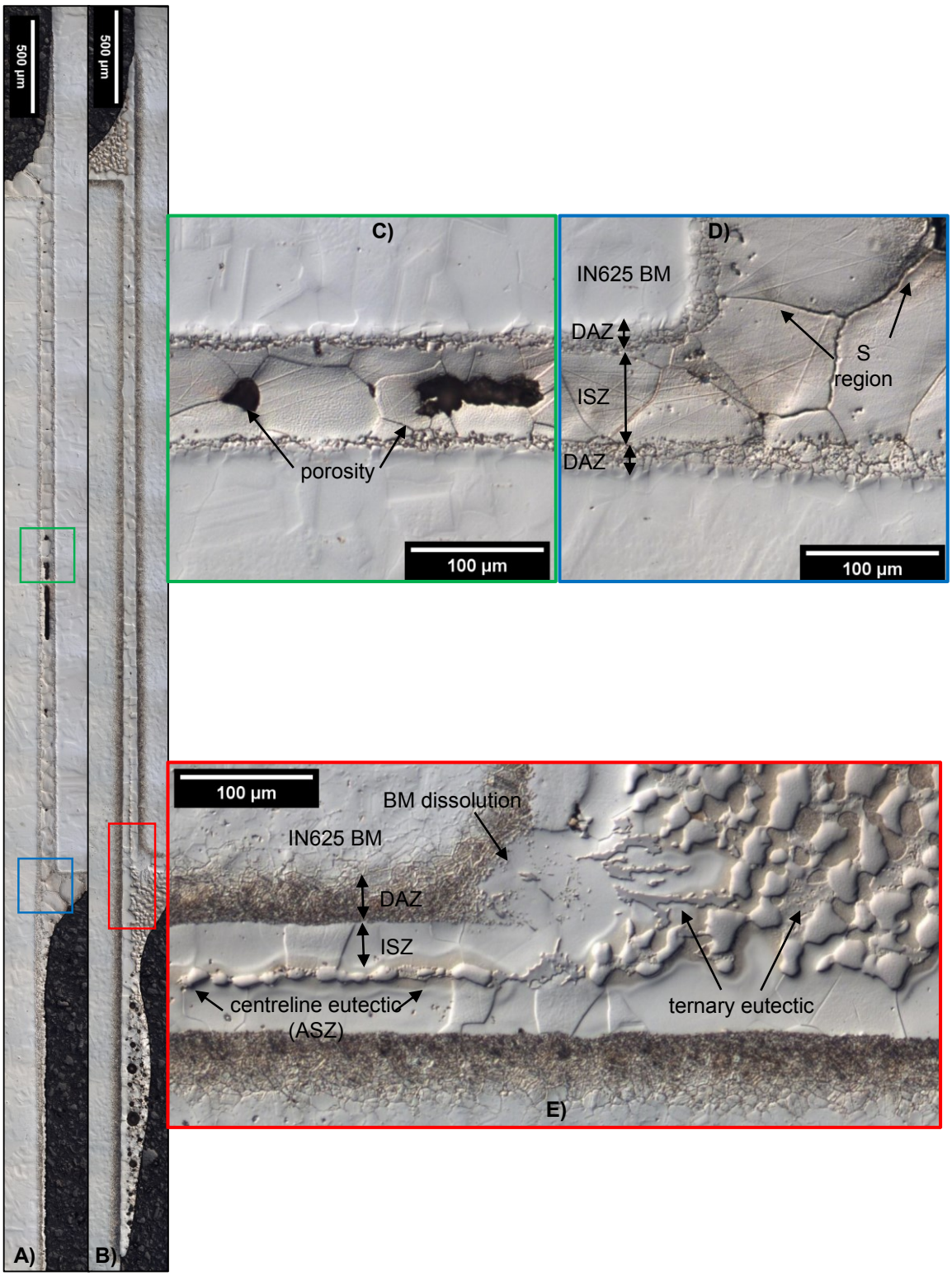

Figure 6.22 – Micrographs of single lap shear specimens showing entire 3.6 mm overlap. A) Ni30/IN625 b) BNi-2/IN625.

The braze thickness of all shear test specimens was measured at 15 points along each 3.6 mm overlap, average values are summarized in Table 6.2. Each sample has two data points, side A1 and A2, as indicated in Figure 6.16. The braze thickness achieved by the tack welding process was close to the goal of 50 µm. Measured braze thickness ranged from 50 to 70 µm the variation in braze thickness can be attributed to surface roughness caused by Nicroblasting the IN625 BM, small amount of dissolution, and human error during tack welding.

Table 6.2 – Measured braze thickness of single lap shear test specimens.

Sample	Side	Average braze thickness (µm)		Position of centreline eutectic from front of joint (µm)
N1	A1	54.5	± 4.8	n/a
	A2	67.0	± 7.6	n/a
N2	A1	59.7	± 8.1	n/a
	A2	61.5	± 7.2	n/a
N3	A1	55.9	± 10.8	n/a
	A2	55.1	± 11.2	n/a
B1	A1	54.2	± 7.5	283
	A2	65.1	± 7.9	1132
B2	A1	54.8	± 6.6	391
	A2	62.7	± 6.8	1097
B3	A1	49.6	± 6.2	none
	A2	52.3	± 7.1	197

Lap joints brazed with BNi-2 did show small amounts of centreline eutectic (shown in Figure 6.22E) in the braze joint in some samples, summarized in Table 6.2 indicating incomplete IS. The centreline eutectic was found only near the "front" of the lap joint where the FM powder was initially located. The presence of eutectic has a direct correlation with the thickness of the braze, it was found that centreline eutectic is present when the braze thickness is above 65 µm. Lap joints B1 and B2 had eutectic present up to 1 mm from the front of the joint. Sample B3 was found to have the lowest braze thickness (50 to 59 µm) and had eutectic present only up to 197 µm from the front of the joint (the

lowest of all samples). All BNi-2/IN625 shear specimens showed an increased level of dissolution at the front of the joint as shown in Figure 6.22.

BNi-2 braze lap joint shear specimens also had a large volume of ternary eutectic phase present in the front and back fillets. This feature has the same origins as discussed above for the Ni30 joints. The fillets represent an effective gap size much larger than the maximum brazing clearance. For the BNi-2/IN625 joint, Table 6.2 indicates that the MBC is very close to 50 μm, much smaller than the fillet dimensions. Unlike the Ni30/IN625 where solidification leads primarily to a microsegregated, single phase solid solution, BNi-2 fillet solidification produced metal boride secondary phases. Work by Chen et al. [21], [22] also identified these large regions of ternary eutectic borides in the fillet region which was attributed to initial fracture propagation and final failure of the material.

6.3.4 Shear testing of single lap joint specimens

The load vs strain curves of shear testing single lap shear joint specimens are presented in Figure 6.23. Because all samples are the same dimensions (width, overlap distance, plate thickness) comparing the failure load of the samples is a general way to examine the fracture conditions of the samples. The strain in Figure 6.23 is calculated using the extensometer gauge length (25 mm) less the overlap distance (~3.6 mm) because the overlap region does not experience elongation as in the base metal plate as such:

$$\varepsilon = \frac{\Delta L}{(25 - A)} \tag{20}$$

The overlap distance, A, was measured for each individual sample.

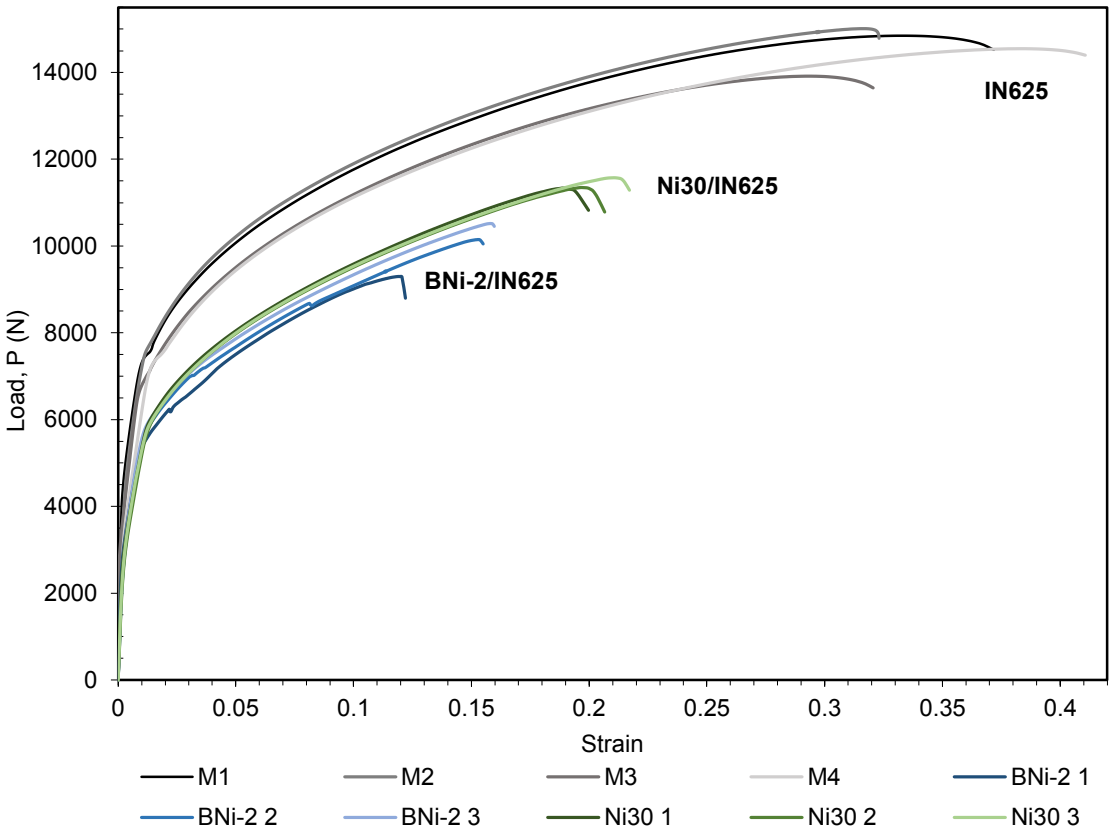

Figure 6.23 – Load versus strain curve for IN625 (single lap simulated), and single lap brazed specimens using Ni30 and BNi-2 filler metals. Strain is calculated less the overlap distance.

It should be noted that samples were tested until complete failure which is defined for this report as the point at which the test specimen separates into two parts. All samples achieved complete failure except sample B1 (IN625/BNi-2). This sample prematurely tripped the elongation safety limit of the extensometer and stopped the test. For this reason, it will not be included in following analysis calculations, but the fracture mode will be included in discussion.

As expected, the monolithic IN625 specimens (M1 to M4) failed at both a higher load and elongation than all brazed test specimens, failing in the base metal region away from the overlapped region. Within the braze joint specimens, Ni30/IN625 failed at a higher load and higher elongation than BNi-2/IN625. All brazed single lap shear test

specimens follow a very similar curve indicating that prior to failure they have similar stress-strain response properties. Ni30/IN625 specimens failed in brazed region, and BNi-2/IN625 specimens failed in the base metal. Images of all six braze lap shear specimens after shear testing are shown in Figure 6.24.

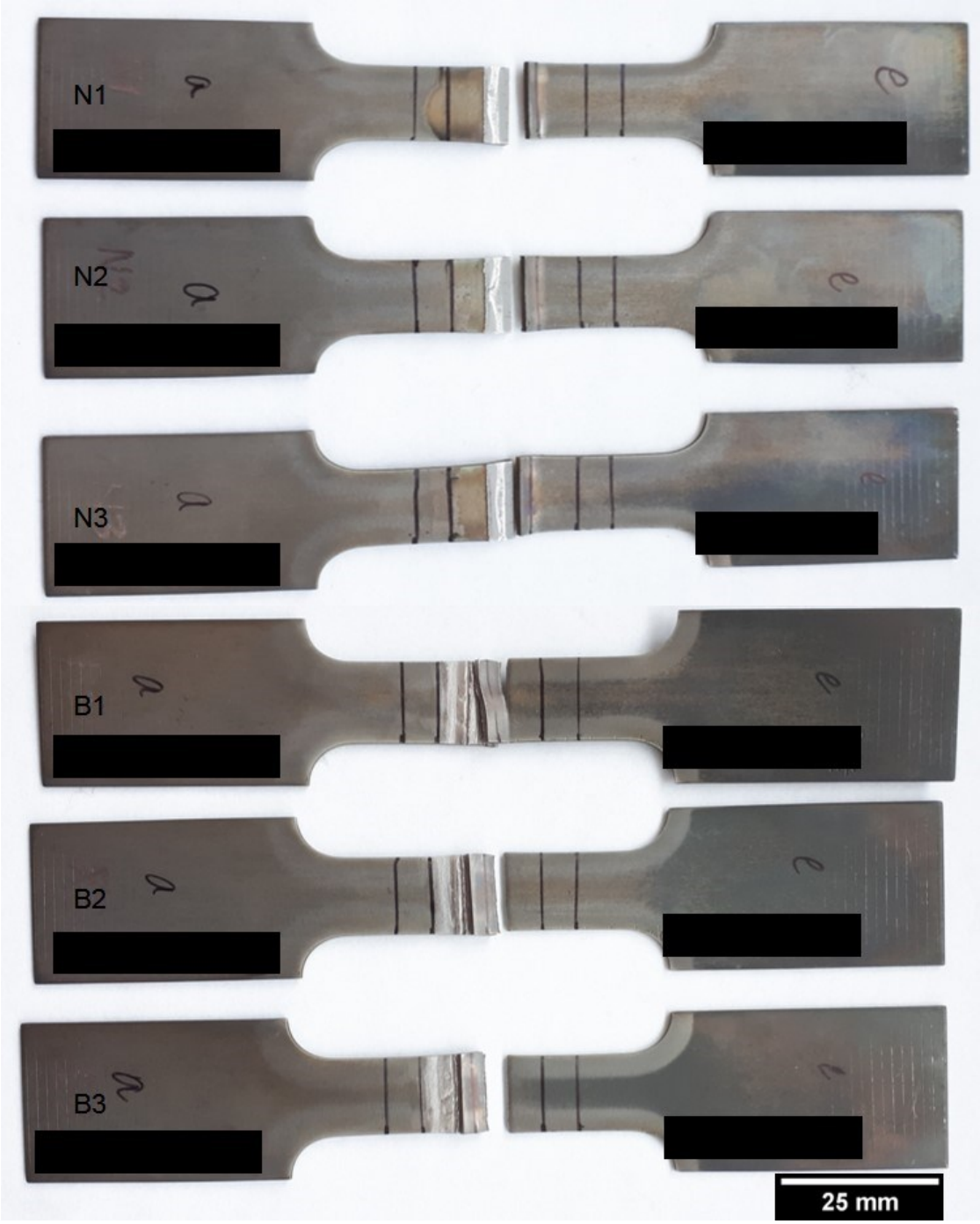

Figure 6.24 – Brazed single lap joint shear test specimens post testing showing failure locations. Specimens from top: BNi-2 3, BNi-2 2, BNi-2 1, Ni30 3, Ni30 2, Ni30 1.

Table 6.3 summarizes the calculated average shear and tensile fracture strengths according to AWS C3.2M [67] (Equation 14 and Equation 15), and the von Mises shear stress in the base metal calculated according to Equation 19. The average

tensile stress in the base metal was higher in the shear specimens brazed with Ni30 compared to BNi-2. The shear specimens brazed with Ni30 showed a slightly larger bending angle than the BNi-2 brazed shear specimens. The bending angle was measured from micrographs of the overlap region using FIJI [55] image analysis software.

Table 6.3 – Summary of lap shear test results for Ni30/IN625 (N), BNi-2/IN625 (B) braze joints, and monolithic IN625 (M) specimens.

	Avg. BM tensile stress (MPa)	Avg. FM shear stress (MPa)	Bending angle (φ)	$\frac{\sigma_e}{\sigma}$	σ_e at fracture (MPa)
N1	743.8	240.2	23	0.804	193.0
N2	744.6	234.4	21	0.815	191.1
N3	759.4	237.2	23	0.797	189.0
B2	665.9	206.3	20	0.821	169.3
B3	690.2	229.0	16	0.859	196.8
M1	974.1	324.7	12	0.893	277.8
M2	971.7	328.3	12	0.893	293.3
M3	913.0	304.3	10	0.913	289.8
M4	954.5	318.2	9	0.922	293.0

The average tensile stress at fracture in the base metal of IN625 monolithic specimens was found to be very close to literature value of 930 MPa for IN625 wrought material [76]. Suggesting that the brazing thermal profile does not have a significant effect on mechanical properties of IN625 base metal. Macroscopic failure analysis of shear test specimens

Images of the brazed single lap shear specimens post shear testing are shown in Figure 6.24 and a summary of failure locations is shown in Figure 6.25. The primary fracture in all Ni30/IN625 lap shear specimens began at each fillet, continued along the interface between the BM and DAZ, until reaching the centre of the overlap where the braze joint fractured in a shear manner. Secondary fractures were noted in fillet region in

areas of highest bending. BNi-2 brazed samples all ultimately failed in the fillet/base metal region (except for B1) with secondary failures in the braze joint. Specimen B1 did not fully fail but fractured through the braze joint through the entire overlap on side A1, but side A2 did not fail through the braze. Specimen B2 failed through the base metal between location c/d and showed secondary fractures through the braze joint on Side A1 (~0.2 mm) and side A2 (~1.4 mm). Specimen B3 failed through the base metal between location c/d and showed very small (<0.2 mm) secondary fractures through the braze joint on Side A1 and A2.

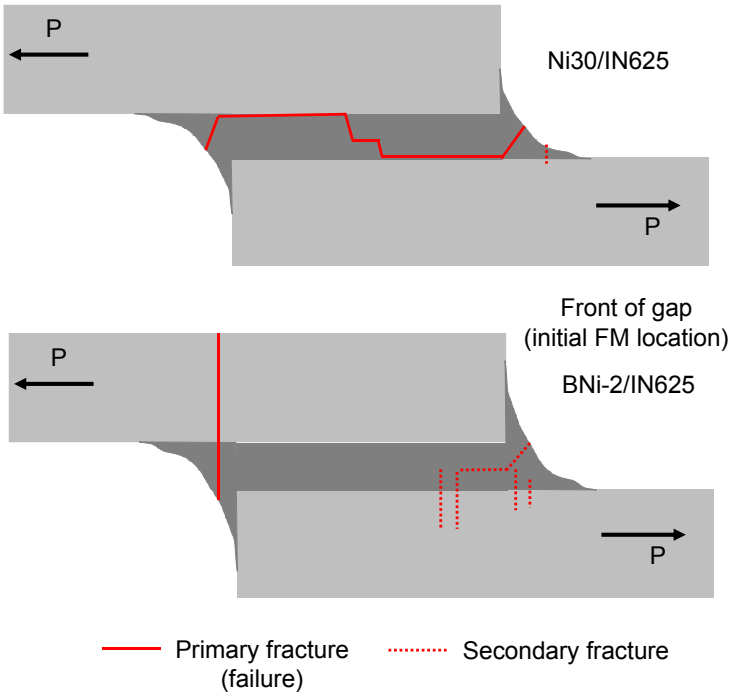

Figure 6.25 – Summary of failure location found in Ni30/IN625, and BNi-2/IN625 brazed single lap shear joints.

The length and location (side A1 or A2) of secondary fractures through the braze joint in BNi-2 braze test specimens correlates well with the noted presence of centreline eutectic, summarized in Table 6.2. This is to be expected, as this brittle phase is well

known in literature to be detrimental to the strength of a braze joint. The eutectic phase will be examined in more detail in Section 6.3.5.2.

In-situ video of the tests proved to be very valuable in failure analysis. Stills extracted from the video are presented in Figure 6.26 and Figure 6.27. Comparing images a) and b) for both Ni30 and BNi-2 brazed lap specimens, the bending of the base metal due to realignment of the offset plates is visible. In image c) (taken immediately before final failure) fractures are visible in both samples showing the initiation points. These video stills, Figure 6.26, prove that in the Ni30/IN625 brazed specimens, the fracture does initiate in both the front and back fillet and each fracture propagates through the braze region where the fractures meet and ultimate failure occurs. The fracture propagation happens very quickly, after fillet fractures are visible.

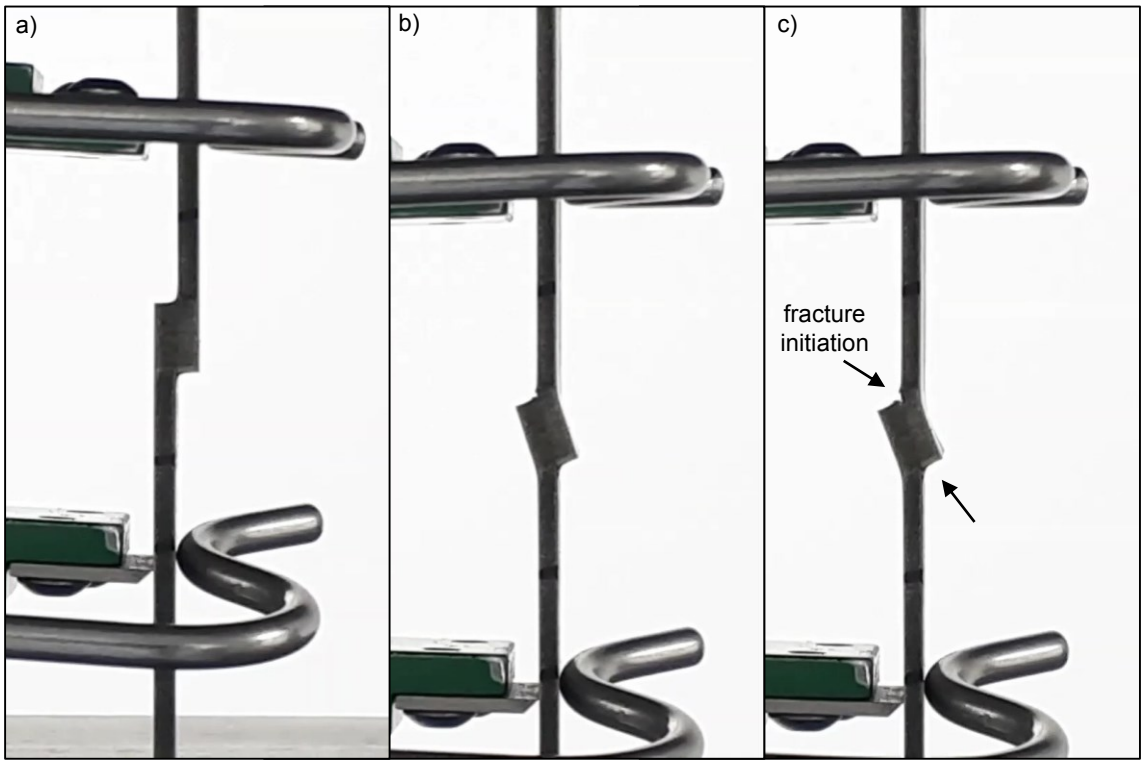

Figure 6.26 – Progression of Ni30/IN625 single lap joint shear test. a) Initial configuration, no stress applied. b) maximum bending, distortion of base metal by realignment and contraction. c) immediately before fracture, initiation of fracture in

fillets visible due to tearing force in braze joint. Images extracted from video footage of test.

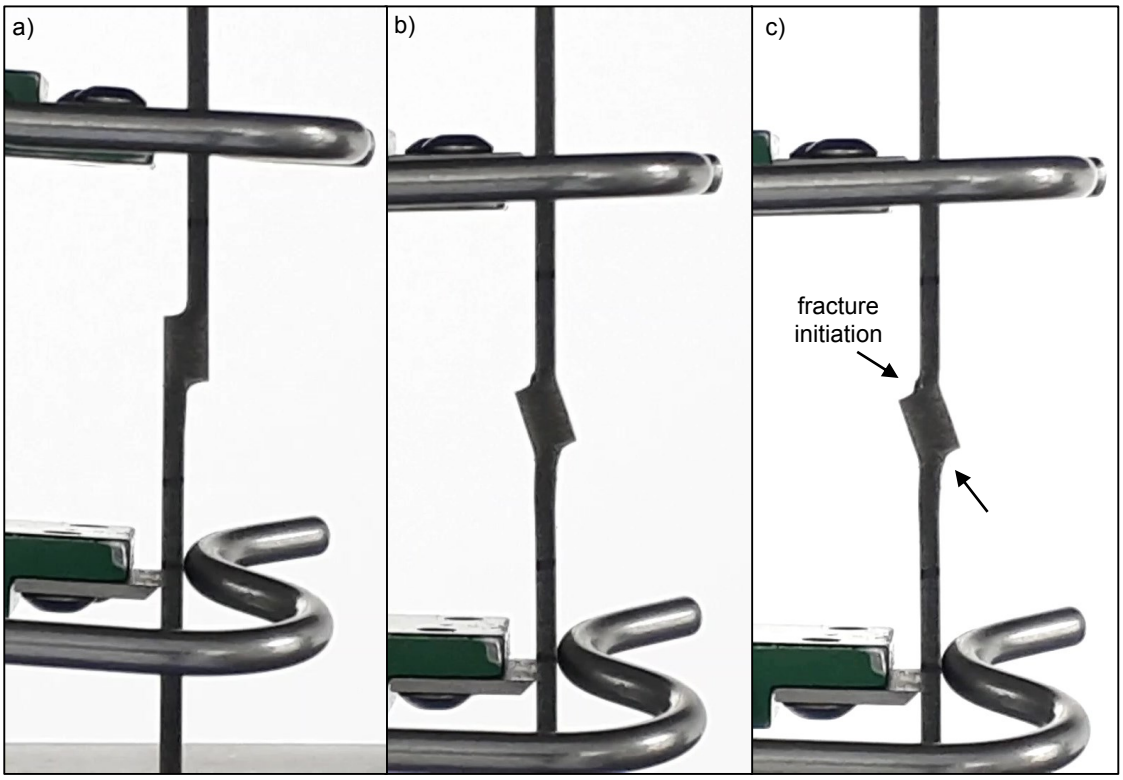

Figure 6.27 – Progression of BNi-2/IN625 single lap joint shear test. a) Initial configuration, no stress applied. b) maximum bending, distortion of base metal by realignment and contraction. c) immediately before fracture, initiation of fracture in fillets visible due to tearing force in braze joint. Images extracted from video footage of test.

In the BNi-2/IN625 brazed specimens, Figure 6.27, the video stills show that, in a similar manner to Ni30 specimens, fractures initiate in both fillets. In specimens B1 and B2, which both contain centreline eutectic, the fillet fracture propagates minimally through the braze joint along the centreline eutectic, but this was not visible through video analysis. Instead, final failure occurred by the propagation of the crack initiated in the fillet, through the DAZ and base metal perpendicular to the loading direction. In Figure 6.27c), the contraction of the base metal just outside the overlap is visible. This is the point where final fracture occurs. More detailed microscopic analysis will be covered in the following section.

6.3.5 Microstructural failure analysis of shear test specimens

Macroscopic analysis gave a general view of fracture propagation and ultimate failure. With the addition of microstructural analysis, a more complete view of the failure modes can be developed.

6.3.5.1 Ni30/IN625 fracture surface analysis

Fractured samples were metallographically prepared to examine the cross section of the failed samples and prepared for SEM analysis of the fracture surface. Optical micrographs of Ni30/IN625 are shown in Figure 6.28. Secondary fractures were located in the front fillet (Figure 6.28a)) which propagated through the DAZ but stopped once they reached the unaffected IN625. In each fillet, the fracture closest to the gap opening did eventually propagate in through the DAZ matrix or along the DAZ/BM interface (Figure 6.28 d) and e)). As stated previously, the fracture was found to propagate through the braze very quickly as visible in the recorded video. The effects of this is shown in Figure 6.28a) and b) where the failed overlapped region is relatively flat. The inflection point of the base metal is at the front and back of the overlap meaning that the overlap region remained intact for much of the test. If the fracture did propagate slowly through the braze region the inflection point would be within the braze and the base metal would be significantly more curved. This also means that the peeling force was minimal in these samples.

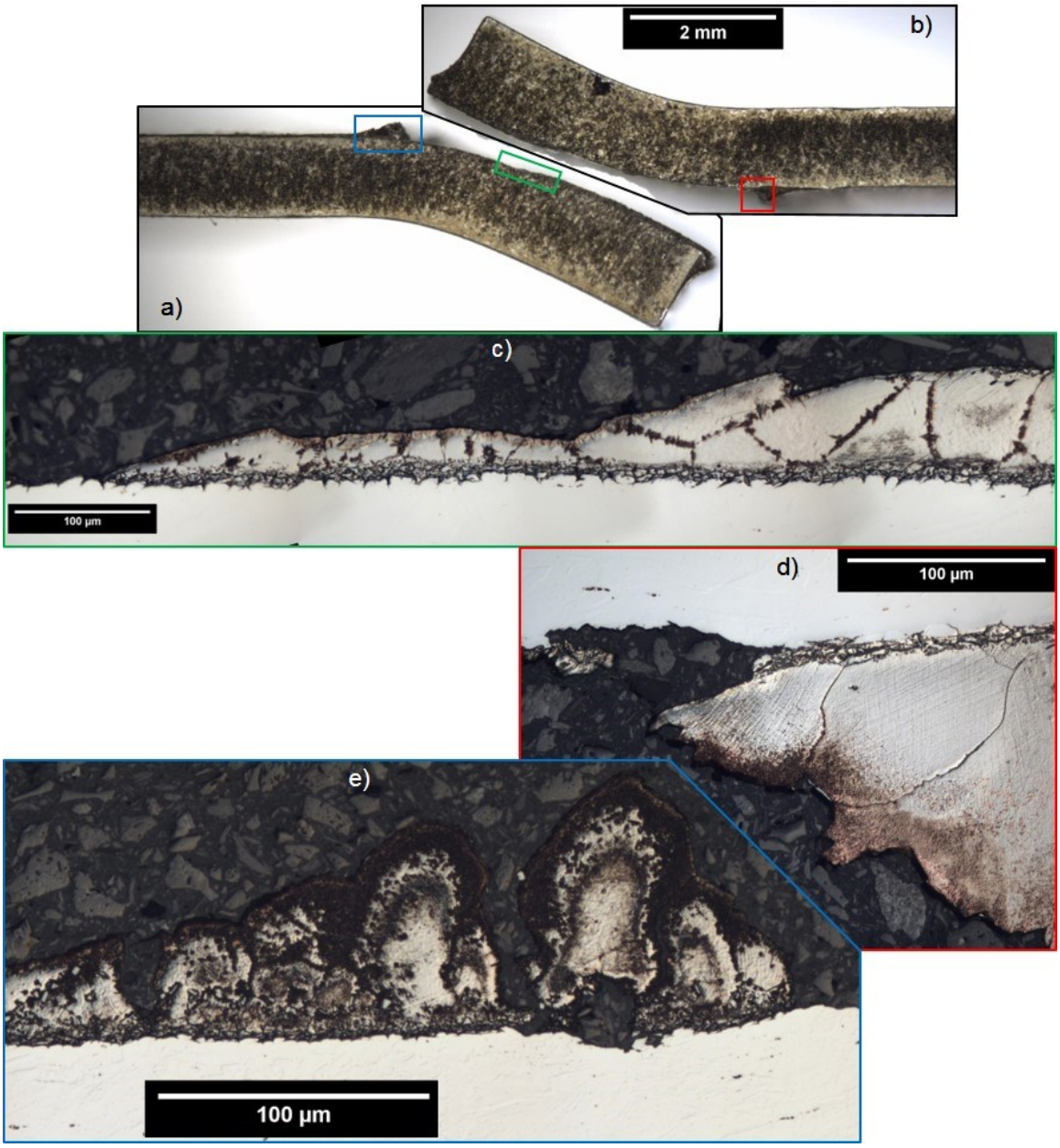

Figure 6.28 – Micrographs of Ni30/IN625 (N3) post shear specimen. a) bottom IN625 plate, b) top IN625 plate, c) shear fracture through braze d) and e) fracture through fillets.

In Ni30/IN625 HBJ and lap joints (Figure 6.17), it was found that the composition of the DAZ matrix was similar to IN625 with decreased concentration of Cr and Mo. Cr and Mo in this region was found to be concentrated in the DAZ precipitates (possibly M_6C or $M_{23}C$ carbides) with only 7 to 16 wt% Cr and 0.8 to 3 wt% Mo. Cr and Mo are potent solid solution strengtheners in Ni alloys, and the most important in IN625. A

decreased concentration of solid solution strengtheners would decrease the strength of the matrix around the precipitates. This region of decreased strength, and the added stress caused by base metal bending could cause the fracture to propagate along DAZ matrix.

Figure 6.28c) shows the region of the overlap where fracture propagates through the Ni30 braze. In this region the fracture is intergranular. Because the S region is concentrated around the grain boundaries, it is unclear if this caused fracture propagation. Though, the increased Cu content of the S region would suggest a lower strength region of the braze joint. According to FEA results by Flom and Wang [72], the middle of the overlap region would have the lowest stress of the braze joint overlap during testing.

The fracture surface of the Ni30/IN625 shear specimen has three regions: BM/DAZ interface, shear fracture through braze joint, and between the braze joint/DAZ interface. Through fracture analysis it was found that the fracture mainly propagated through the BM/DAZ interface with small regions where the fracture propagated through the braze joint/DAZ interface. SEM micrographs of the regions are shown in Figure 6.29, and schematic of these regions is shown in Figure 6.25. Figure 6.29a) shows the fracture surface of the base metal and DAZ. In this region, some small intact DAZ precipitates are identified on the fracture surface of the BM. The dimpled fracture surface indicates a ductile fracture. Due to the bending of the plates, it is known that some peeling also occurred. Figure 6.29b) is the fracture surface through the braze joint and DAZ, showing the topography of the DAZ. This fracture surface features secondary fractures through the DAZ. Figure 6.29c) shows the fracture surface in the middle of the overlap where shear fracture through the braze joint was identified. This region is largely smooth with some elongated dimples indicating a shear fracture through the braze joint.

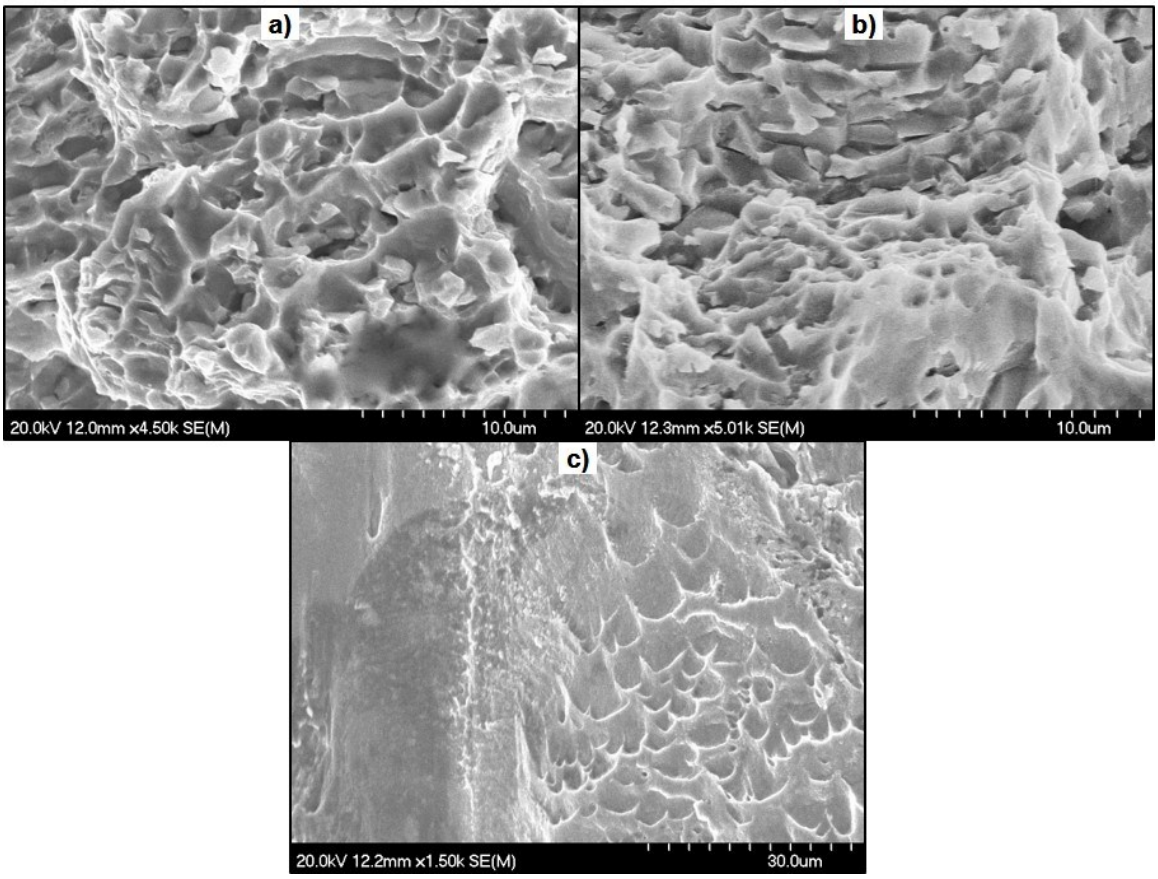

Figure 6.29 – SEM micrographs of Ni30/IN625 (N2) shear fracture surface of bottom plate. Fracture surface of a) BM/DAZ interface b) DAZ/braze joint, and c) braze joint in shear region.

Because the fracture propagated primarily through the DAZ/BM interface it can be determined that the braze region is of relatively high strength and high ductility. It is probable that the decreased concentration of solid solution strengtheners (Cr and Mo) in the DAZ and the relatively large size and of DAZ precipitates decreased the strength of this region causing fracture propagation.

6.3.5.2 BNi-2/IN625 fracture surface analysis

Figure 6.30 presents micrographs of BNi-2/IN625 brazed specimen (B2) after shear testing. This sample did have centreline eutectic present as indicated in Table 6.2. Macroscopic analysis showed that all specimens failed through the base metal adjacent to

the fillet region. Specimens with significant amount of centreline eutectic (B1 ad B2) had secondary fractures through the braze joint. In Figure 6.30c), the fracture can be seen to propagate through the centreline eutectic phase and stop when this phase becomes discontinuous. This fracture is shown to be very straight indicating a brittle fracture. The discontinuous portion of the centreline eutectic is also fractured in some locations but the strong and ductile ISZ of the braze joint is not fractured in these locations. Figure 6.30d) shows the location of failure, where the fracture began in the ternary eutectic of the fillet, and propagated through the DAZ and the unaffected IN625 BM. In the fillet the fracture is intragranular, and very straight, indicating a failure directly through the brittle ternary eutectic phase. In the DAZ and BM, the fracture is intergranular following chain of borides in the DAZ grain boundaries, and through the BM.

Figure 6.30 - Micrographs of BNi-2/IN625 (B2) post shear specimen. a) overlap region, b) IN625 plate, c) to f) notable fractures and features.

A high magnification SEM micrograph of fracture through the DAZ is presented in Figure 6.31. The fracture propagates through the evenly distributed small borides (< 1 µm) nearest to the braze joint, and along the continuous chain of script-like borides along

grain boundaries, as shown in Figure 6.32. Fractures were identified in borides away from the main fracture highlighting the extent of brittleness of DAZ borides. Figure 6.31 shows the diversity of boride size and shape within the DAZ which will lead to differences in the fracture surface.

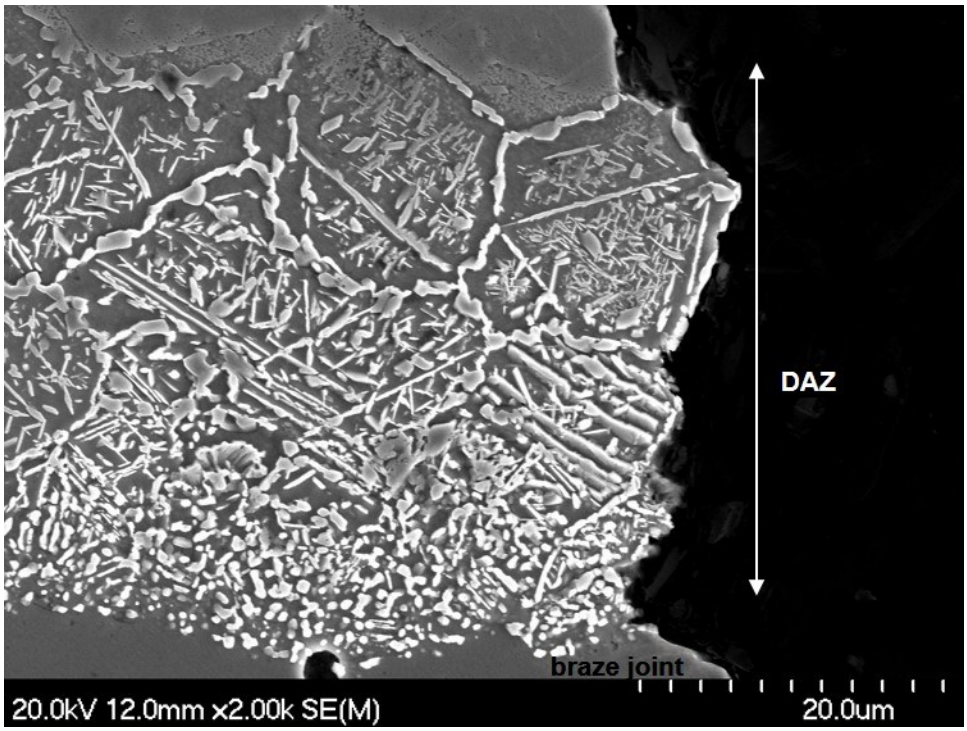

Figure 6.31 – SEM micrograph of BNi-2/IN625 (B2) fracture through the DAZ of IN625 base metal.

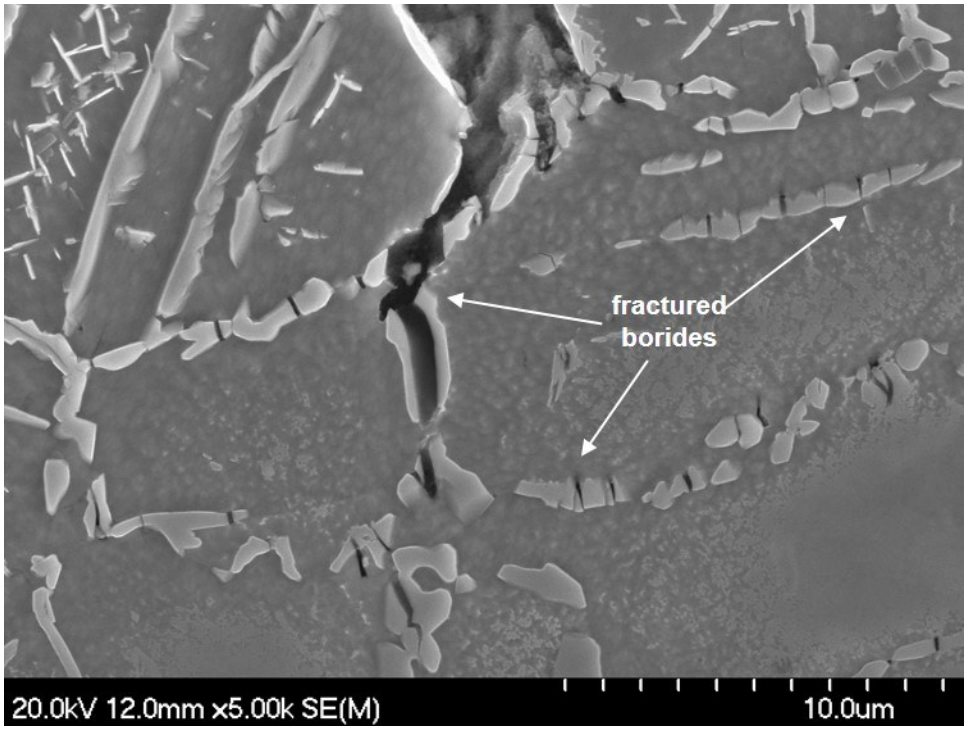

Figure 6.32 - High magnification SEM micrograph of BNi-2/IN625 (B2) fracture through DAZ.

The fracture surface (perpendicular to Figure 6.31) presented in Figure 6.33a) shows the difference between the DAZ near the braze joint (small borides, evenly distributed), and through the continuous chain of borides along grain boundaries. Near the braze joint, the small borides cause a micro-dimpled fracture surface. Approximately 20 μm away from the braze joint interface, the fracture surface features larger dimples with flat cleavage planes indicating fracture through the brittle borides. Figure 6.33b) presents the fracture through the IN625 base metal away from the braze joint such that this region is not diffusionally affected. This fracture surface features a larger dimpled surface indicating a ductile fracture. The dimples are slightly elongated indicating distortion of the base metal. Figure 6.33c) presents the fracture surface through the back fillet, perpendicular to the fracture shown in Figure 6.30f). This fracture surface features large (20-30 μm) cleavage facets indicating a brittle fracture. This is to be expected as the

fracture through the fillet was observed to travel through the larger brittle ternary borides present in the fillets.

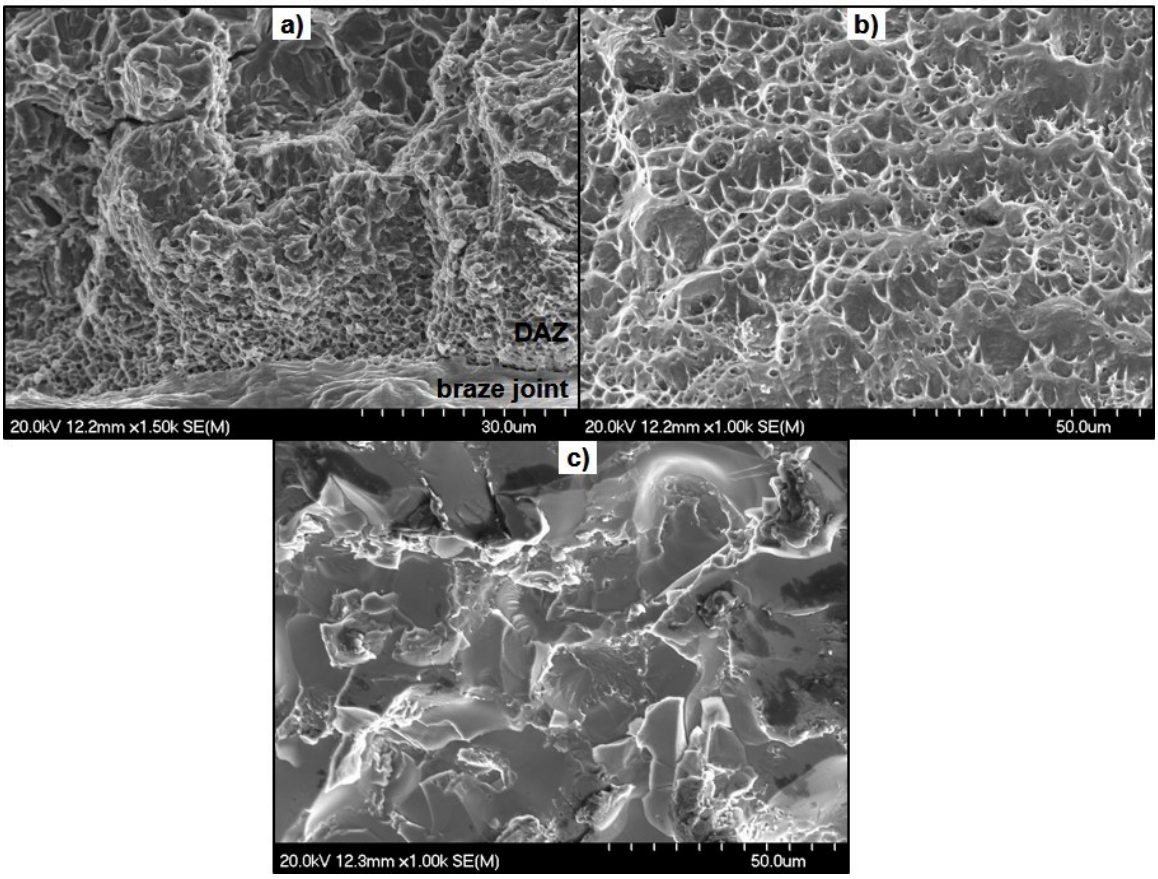

Figure 6.33 – SEM micrographs of BNi-2/IN625 (B3) shear specimen fracture surface. Fracture surface of a) braze joint and DAZ of IN625 b) IN625 (unaffected by braze joint), and c) back fillet of joint.

It is important to note that in the BNi-2 specimens, failure through the base metal occurred at the back of the joint (as shown in Figure 6.25), where no centreline eutectic was found. The weak and brittle ternary eutectic did initiate the fracture in the fillet, but ultimate failure was caused by the propagation of this crack through the DAZ and into the BM, at a significantly lower stress than monolithic IN625 samples. The influence of the DAZ in both phase make up, and distribution of borides is important to the failure

analysis. Significant distortion in the base metal indicates that the BM retained ductile properties, but the strength was decreased by the DAZ.

The early fracture through the DAZ, created a crack in the IN625 BM causing a stress concentration around the crack tip. The crack tip increases the complexity of the stress distribution in this region. Stress is now a combination of bending moment due to realignment of top/bottom plates, tensile and shear stress, and stress at crack tip. The crack initiating in the DAZ will propagate through the BM when the stress at the crack tip opening reaches a critical stress.

6.3.5.3 Monolithic IN625 fracture surface analysis

IN625 monolithic samples failed in the base metal approximately 6 to 16 mm away from the gap opening. As explained in the experimental procedure, this is due to inconsistencies in EDM machining of the gauge region of IN625 monolithic samples. Because of these inconsistencies, the fracture occurred at the point where BM thickness was at a minimum (1.15 mm). Despite this error, the fracture surface can still be examined and compared to the BM fracture in BNi-2/IN625 brazed lap shear specimens. Figure 6.34 shows the fracture surface of sample M4 featuring an elongated dimpled structure indicating a ductile fracture with distortion of the base metal. This is consistent with a ductile failure of a typical tensile specimen. Comparing Figure 6.34 to the BM fracture surface of BNi-2/IN625 away from the braze joint (Figure 6.33b) the fracture surfaces are very similar, both exhibiting a dimpled fracture surface.

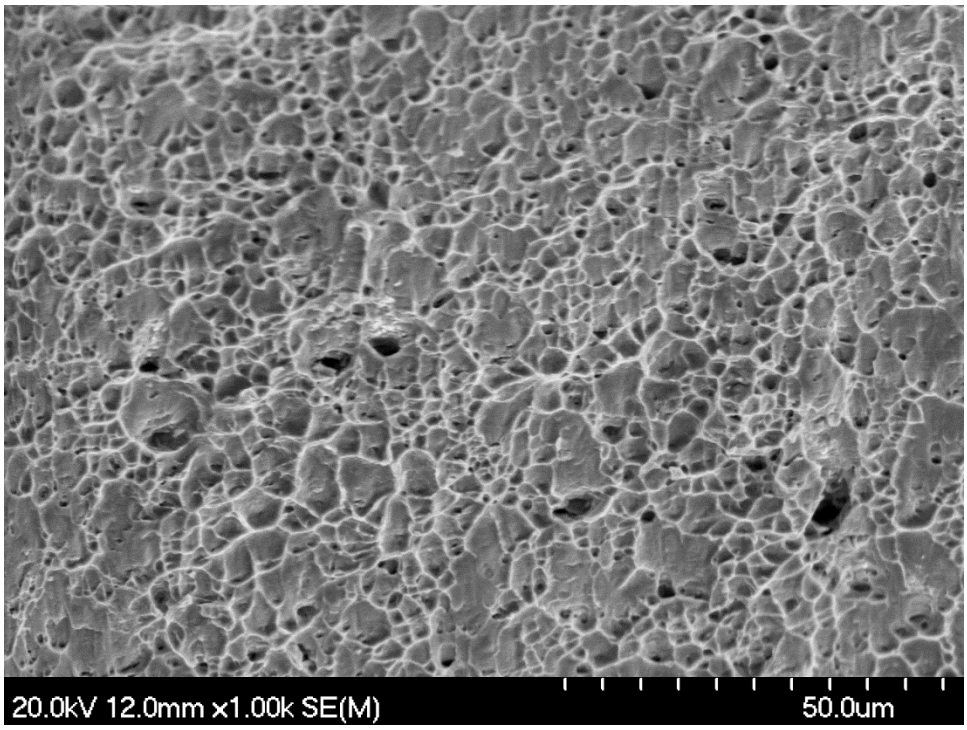

Figure 6.34 – SEM micrograph of IN625 monolithic (M4) shear specimen fracture surface

6.3.6 Conclusions

As expected, monolithic IN625 had the highest fracture load, strength, and ductility. The bending angle measured in monolithic samples was less than that of braze lap joint specimens. This is probably due to initial fractures in the fillets of brazed lap joints which increased the possibility of bending in the overlap region.

Comparing the brazed samples, BNi-2/IN625 lap joints experienced the lowest load at fracture and consequently the lowest fracture strength. In both the Ni30/IN625 and BNi-2/IN625 fracture initiated in the fillet regions. The primary difference between the two joints was based on the final fracture path. Ni30/IN625 samples failed through the braze joint and parallel to the loading direction, primarily through the DAZ matrix which is weakened by decreased concentration of Cr and Mo, and increased concentration of DAZ precipitates at the grain boundaries. Fractures were initiated in the

athermally solidified fillet region. In BNi-2/IN625, cracks initiated in the brittle ternary eutectic phase of the fillet and propagated through brittle borides in the DAZ and base metal, perpendicular to the loading direction. DAZ formations in both joints prove to be sites for crack propagation but had a lesser negative impact on strength of the boron free Ni30/IN625 joints.

Chapter 7 Conclusion

7.1 Summary

This research focussed on developing a novel boron free filler metal (FM) using Cu and Mn as alternative melting point depressants (MPDs) to avoid the formation of brittle boride phases which have limited the application of TLP bonded Ni base superalloys. The brazing temperature of 1050 °C was respected in this work to allow for close comparison with relevant boron containing FM alloys. The NiCuMn system is a solid solution at all temperatures and compositions examined therefore avoiding the possibility that any brittle intermetallic phases will form in the braze joint.

Three NiCuMn powder alloy mixtures (Ni10, Ni20, and Ni30, where 10, 20, 30 refers to the Ni content with a fixed Mn:Cu ratio) were examined to determine the melting range and resulting microstructure of the FM without effects of the base metal. DSC trials examining their melting properties showed that Ni10 powder particles caused an initial endothermic peak at ~900 °C, with Ni20 and Ni30 exhibiting a second endothermic in the range of 920 to 980 °C, and 970 and 1040 °C respectively. Ni30 FM alloy was chosen for further work because of the higher liquidus temperature and increased Ni content.

Microstructural analysis of Ni30 FM alloy showed that at 900 °C interdiffusion between NiCuMan37(i.e. Ni10) and Ni powder particles enriched NiCuMan37 MA particles up to 18.5 wt% Ni. On heating to temperatures up to 1025 °C increased densification was noted due to the increased fraction of liquid formation and particle rearrangement. At 1050 °C, the Ni30 alloy completely melted and densified producing a solid solution γ-Ni joint enriched with base metal elements and a copper rich segregated

region (S region). Molybdenum rich precipitates were identified in the DAZ as discontinuous chains along grain boundaries.

Dense and void free IN625 based metal (BM) braze half joints were produced using Ni30 FM 1050 °C. Narrow gap (full width ~110 μm) and wide gap (~380 μm) conditions were examined and kinetics were quantified. It was determined by single point equilibrium calculations using Thermo-Calc software that the S region has a lower T_{sol} than the joint matrix. Longer hold times at 1050 °C allowed for increased diffusion of Cu and Mn into the BM thus increasing the calculated T_{sol} of the S region. When the calculated T_{sol} of both the S region and matrix were above 1050 °C, the goal of isothermal solidification (IS) was achieved.

Maximum Brazing Clearance (MBC) plots were prepared by measuring the enthalpy on melting after increasing hold time at 1050 °C in the DSC. The enthalpy of melting was found to decrease with increasing hold time indicating the progression of IS. Complete IS, defined as the hold time at which no remelting endotherm was detected, and the calculated T_{sol} of the S region was above 1050 °C, was confirmed in narrow gap conditions after 80 minutes, and in wide gap conditions after 1320 minutes. Linear regression of MBC plots determined the rate of ISZ growth to be 7.04-7.19 μm $min^{-1/2}$ for wide gap conditions and 6.17-6.13 μm $min^{-1/2}$ for narrow gap conditions. These rates are comparable to the IS rate of boron containing FM cited in literature to be between 3.5 to 8.5 μm $min^{-1/2}$. Some disagreement between calculated MBC graphs of wide and narrow gap was noted. This was primarily due to less experimental work completed and inconsistent wetting of the base metal in narrow gap samples. Additionally, short hold times (< 60 min) were not examined in wide gap condition.

Application of a model to determine the time of IS using literature diffusivity values of Cu and Mn in Ni predicted significantly faster ISZ growth rates than found experimentally. The experimentally determined IS rate was used to calculate a diffusivity value of Ni30 into IN625. The experimental diffusivity value was determined to be similar to interdiffusion of Cu and Ni. This suggests that the IS rate is primarily controlled by the slower diffusing Cu into IN625.

IN625 lap joints were prepared using Ni30 and BNi-2 as filler metals to asses the gap filling ability, strength, and failure mode of the filler metals. Ni30 successfully melted and filled the 50 μm gap where it underwent complete IS. Shear testing of brazed single lap test specimens had a decreased strength compared to wrought IN625, but lap joints brazed with Ni30 had a higher failure strength than BNi-2 braze joints. Lap joints brazed with both filler metals had initial fractures form in the fillet region where the joint did not undergo complete IS. Ni30/IN625 samples failed through the braze joint and parallel to the loading direction, primarily through the DAZ matrix, and BNi-2/IN625 samples failed through the base metal propagating through brittle borides in the DAZ and base metal, perpendicular to the loading direction. DAZ precipitates in both joints prove to be sites for fracture propagation but had a lesser negative impact on strength of the boron free Ni30/IN625 joints.

In summary, the Ni30 FM described in this work shows excellent promise in replacing boron containing FM alloys used in TLP bonding. The alloy has a liquidus temperature just below the brazing temperature of 1050 °C, forms a solid solution braze joint absent of intermetallic phases, and reaches complete IS in a similar time period compared to common boron containing FM alloys. DAZ precipitates were identified and

did propagate fracture during shear testing of lap joints but the strength of the joint was higher than that of boron containing FM alloys.

7.2 Recommendations of future work

The following points are recommended as possible areas of future work to further assess the potential of Ni30 as a FM:

- Investigate the compatibility of Ni30 with simpler Ni base metals (Ni200, IN600) to examine the formation of the DAZ and DAZ precipitates.
- Perform further Ni30/IN625 wide gap HBJ tests focussing on short hold times (<60 minutes). This could help clear up disagreement between narrow and wide gap MBC plots.
- Perform x-ray diffraction on samples to determine phases present in DAZ. This could help further identify the DAZ precipitates.
- Perform shear testing on lap joints with a wide range of overlap lengths to further characterize the strength and failure modes of both Ni30 and BNi-2 with IN625 base metal.

References

[1] S. Kerr and J. Mandyck, “Greening Aviation From The Ground Up,” 2017.

[2] M. Cervenka, “The Rolls Royce Trent Engine.” Rolls Royce, p. 40, 2000.

[3] M. J. Donachie and S. J. Donachie, *Superalloys: A Technical Guide*, Second Edi. ASM International, 2002.

[4] “CES EduPack.” Granta Design Limited, Cambridge, UK, 2017.

[5] W. F. Smith, “Structure and Properties of Engineering Alloys,” *2nd ed. New York McGraw-Hill.*, 1993.

[6] C. L. English, S. K. Tewari, and D. H. Abbott, “An overview of ni base additive fabrication technologies for aerospace applications,” in *7th International Symposium on Superalloy 718 and Derivatives*, 2010, vol. 1, pp. 399–412.

[7] AWS, *Brazing Handbook*, Fifth Edit. Miami, Florida: American Welding Society, 2007.

[8] ASM Handbook Committee, *Welding, Brazing, and Soldering*, Second., vol. 6. Materials Park, Ohio: ASM International, 1993.

[9] D. F. Paulonis, D. S. Duvall, and W. A. Owczarski, “Diffusion Bonding Utilizing Transient Liquid Phase,” 3,678,570, 1972.

[10] G. O. Cook and C. D. Sorensen, “Overview of transient liquid phase and partial transient liquid phase bonding,” *J. Mater. Sci.*, vol. 46, no. 16, pp. 5305–5323, 2011.

[11] W. F. Gale and D. A. Butts, “Transient liquid phase bonding,” *Sci. Technol. Weld. Join.*, vol. 9, no. 4, pp. 283–300, 2004.

[12] W. D. MacDonald and T. W. Eagar, “Transient Liquid Phase Bonding,” *Annu. Rev. Mater. Sci.*, vol. 9, no. 4, pp. 23–46, 1992.

[13] D. S. Duvall, W. A. Owczarski, and D. F. Paulonis, “TLP* Bonding: a New Method for Joining Heat Resistant Alloys,” *Weld. J.*, vol. 53, no. 4, pp. 203–214, 1974.

[14] A. Rabinkin, “High temperature brazing: filler metals and processing,” in *Advances in Brazing*, 1st ed., D. P. Sekulić, Ed. Cambridge, UK: Woodhead Publishing, 2013, pp. 121–157.

[15] M. Pouranvari, A. Ekrami, and A. H. Kokabi, “Microstructure-properties relationship of TLP-bonded GTD-111 nickel-base superalloy,” *Mater. Sci. Eng. A*, vol. 490, no. 1–2, pp. 229–234, 2008.

[16] M. Weinstein, R. L. Peaslee, and F. M. Miller, “How to Choose Nickel-Based Filler metals for Vacuum Brazing,” *Weld. J.*, vol. 88, no. 4, pp. 59–61, 2009.

[17] W. D. Callister and D. G. Rethwisch, *Materials Science and Engineering: An Introduction*, 8th ed. Hoboken, NJ: Wiley and Sons, Inc, 2010.

[18] V. F. Khorunov and S. V. Maksymova, “Brazing of superalloys and the intermetallic alloy (γ -TiAl),” in *Advances in Brazing*, D. P. Sekulić, Ed. Cambridge, UK: Woodhead Publishing, 2013, pp. 85–117.

[19] T. Henhoeffer, X. Huang, S. Yandt, and P. Au, “Fatigue Properties of Narrow and Wide Gap Braze Repaired Joints,” *J. Eng. Gas Turbines Power*, vol. 133, no. 9, p. 092101, 2011.

[20] T. Henhoeffer, X. Huang, S. Yand, P. Au, and D. Nagy, “Microstructure and high temperature tensile properties of wide gap brazed cobalt based superalloy X-40,” *Mater. Sci. Technol.*, vol. 25, no. 7, pp. 840–850, 2009.

[21] J. Chen, V. Demers, E.-L. Cadotte, D. Turner, and P. Bocher, “Structural Performance of Inconel 625 Superalloy Brazed Joints,” *J. Mater. Eng. Perform.*, vol. 26, no. 2, pp. 547–553, 2017.

[22] J. Chen, V. Demers, D. P. Turner, and P. Bocher, “Experimental Investigation on High-Cycle Fatigue of Inconel 625 Superalloy Brazed Joints,” *Metall. Mater. Trans. A Phys. Metall. Mater. Sci.*, vol. 49, no. 4, pp. 1244–1253, 2018.

[23] M. L. Kuntz, S. F. Corbin, and Y. Zhou, “Quantifying metallurgical interactions in solid/liquid diffusion couples using differential scanning calorimetry,” *Acta Mater.*, vol. 53, no. 10, pp. 3071–3082, 2005.

[24] E. Lugscheider and K.-D. Partz, “High-Temperature Brazing of Stainless Steel with Nickel-Base Filler Metals BNi-2, BNi-5 and BNi-7,” *Weld. J.*, vol. 62, pp. 160–165, 1983.

[25] M. E. Brown, *Introduction to Thermal Analysis: Techniques and Applications*, 1st ed., vol. 1. New York, NY: Kluwer Academic Publishers, 2001.

[26] W. J. Boettinger, U. R. Kattner, K.-W. Moon, and J. H. Perepezko, “DTA and

Heat-flux DSC Measurements of Alloy Melting and Freezing," 2006.

[27] Netzsch, "Differential Scanning Calorimetry - DSC 404 F1/F3 Pegasus - Method, Technique, Applications." NETZSCH-Geratebau GmbH, pp. 1–24, 2016.

[28] S. F. Corbin and P. Lucier, "Thermal analysis of isothermal solidification kinetics during transient liquid-phase sintering," *Metall. Mater. Trans. A*, vol. 32, no. April, pp. 971–978, 2001.

[29] S. F. Corbin and D. J. McIsaac, "Differential scanning calorimetry of the stages of transient liquid phase sintering," *Mater. Sci. Eng. A*, vol. 346, no. 1–2, pp. 132–140, 2003.

[30] M. L. Kuntz, "Quantifying Isothermal Solidification Kinetics during Transient Liquid Phase Bonding using Differential Scanning Calorimetry," University of Waterloo, 2006.

[31] D. C. Murray and S. F. Corbin, "Determining the kinetics of transient liquid phase bonding (TLPB) of inconel 625/BNi-2 couples using differential scanning calorimetry," *J. Mater. Process. Technol.*, vol. 248, no. December 2016, pp. 92–102, 2017.

[32] S. F. Corbin, S. Winkler, D. R. Turriff, and M. Kozdras, "Analysis of Fluxless, Reactive Brazing of Al Alloys Using Differential Scanning Calorimetry," *Metall. Mater. Trans. A*, vol. 45, no. 9, pp. 3907–3915, 2014.

[33] E. Lugscheider, O. Knotek, and K. Klohn, "Development of Nickel-Chromium-Silicon Base Filler Metals," *Weld. Res. Suppl.*, pp. 319–324, 1978.

[34] F. Jalilian, M. Jahazi, and R. A. L. Drew, "Microstructure Evolution During Transient Liquid Phase Bonding of Alloy 617," *Metallogr. Microstruct. Anal.*, vol. 2, no. 3, pp. 170–182, 2013.

[35] I. Buschke and E. Lugscheider, "New Approaches for Joining High-Temperature Materials," in *Materials Conference 1998 on Joining of Advanced and Specialty Materials*, 1998, pp. 51–55.

[36] X. Huang, "Brazing of CMSX-4 with a Boron - and Silicon-Free Ni-Co-Zr-Hf-Cr-Ti-Al Brazing Alloy," *Weld. J.*, no. July, pp. 233–243, 2014.

[37] R. Zhongci, W. Shuncai, and Z. Yunrong, "Microstructure and bonding behavior of a new Hf-bearing interlayer alloy for single crystal nickel-base superalloy," *Scr.*

Mater., vol. 34, no. 1, pp. 163–168, 1996.

[38] P. Heinz *et al.*, "Diffusion Brazing of Single Crystalline Nickel Base Superalloys Using Boron Free Nickel Base Braze Alloys," *Defect Diffus. Forum*, vol. 273–276, pp. 294–299, 2008.

[39] M. K. Dinkel *et al.*, "New boron and silicon free single crystal-diffusion brazing alloys," *Proc. Int. Symp. Superalloys*, pp. 211–220, 2008.

[40] Y. Zheng, L. Zhao, and K. Tangri, "Microstructure of Ni-10Co-8Cr-4W-13Zr alloy and its bonding behaviour for single-crystal nickel-base superalloy," *J. Mater. Sci.*, vol. 28, no. 3, pp. 823–829, 1993.

[41] B. Laux and J. Rösler, "Development of Ni – Mn-based alloys for the fast epitaxial braze-repair of single-crystalline nickel-based superalloys," *Int. J. Mater. Res.*, vol. 101, no. 5, pp. 614–622, 2010.

[42] W. Miglietti and M. Du Toit, "High Strength, Ductile Braze Repairs for Stationary Gas Turbine Components—Part I," *J. Eng. Gas Turbines Power*, vol. 132, no. 8, pp. 1–12, 2010.

[43] W. Miglietti and M. Du Toit, "High Strength, Ductile Braze Repairs for Stationary Gas Turbine Components—Part II," *J. Eng. Gas Turbines Power*, vol. 132, no. 8, pp. 1–10, 2010.

[44] E. N. Dorofeeva, A. A. Rossoshinskii, G. V. D'Yachek, and V. V. Antoshin, "Formation of the Structure of Joints Brazed with Brazing Alloys of the Cu-Mn-Ni System," *Weld. Prod.*, vol. 31, no. 4, pp. 38–39, 1984.

[45] J. O. Andersson, T. Helander, L. Höglund, P. F. SHi, and B. Sundman, "Thermo-calc and DICTRA, computational tools for materials science." Calphad, pp. 273–312, 2002.

[46] R. K. Roy, A. K. Panda, S. K. Das, Govind, and A. Mitra, "Development of a copper-based filler alloy for brazing stainless steels," *Mater. Sci. Eng. A*, vol. 523, no. 1–2, pp. 312–315, 2009.

[47] W. Sun *et al.*, "Experimental investigation and thermodynamic modeling of the Cu-Mn-Ni system," *Calphad Comput. Coupling Phase Diagrams Thermochem.*, vol. 33, no. 4, pp. 642–649, 2009.

[48] V. E. Bazhenov, "Phase Diagram of the Cu-Ni-Mn System," *Russ. J. Non-Ferrous*

Met., vol. 54, no. 2, pp. 171–177, 2013.

[49] B. Laux, S. Piegert, and J. Rösler, "Braze alloy development for fast epitaxial high-temperature brazing of single-crystalline nickel-based superalloys," *Metall. Mater. Trans. A Phys. Metall. Mater. Sci.*, vol. 40, no. 1, pp. 138–149, 2009.

[50] B. Laux, S. Piegert, and J. Rosler, "Advanced Braze Alloys for Fast Epitaxial High-Temperature Brazing of Single-Crystalline Nickel-Base Superalloys," *J. Eng. Gas Turbines Power*, vol. 132, no. 3, pp. 1–7, 2010.

[51] A. Ghasemi and M. Pouranvari, "Fast Isothermal Solidification During Transient Liquid Phase Bonding of a Nickel Alloy Using Pure Copper Filler Metal: Solubility vs Diffusivity," *Metall. Mater. Trans. A Phys. Metall. Mater. Sci.*, vol. 50, no. 5, pp. 2235–2245, 2019.

[52] M. Pouranvari, A. Ekrami, and A. H. Kokabi, "Microstructure evolution mechanism during post-bond heat treatment of transient liquid phase bonded wrought IN718 superalloy: An approach to fabricate boride-free joints," *J. Alloys Compd.*, vol. 723, pp. 84–91, 2017.

[53] K. Wieczerzak, P. Bała, G. Cios, T. Tokarski, K. Górecki, and Frocisz, "Experimental study of phase transformation in non-equilibrium hypoeutectic alloy from the Fe–Cr–Ni–Mo–C system," *J. Therm. Anal. Calorim.*, vol. 127, no. 1, pp. 449–455, 2017.

[54] S. Preibisch, S. Saalfeld, and P. Tomancak, "Globally optimal stitching of tiled 3D microscopic image acquisitions," *Bioinformatics*, vol. 25, no. 11, pp. 1463–1465, 2009.

[55] J. Schindelin *et al.*, "Fiji: an open-source platform for biological-image analysis," *Nat. Methods*, vol. 9, no. 7, pp. 671–675, 2012.

[56] E. D. Moreau and S. F. Corbin, "Initial Boron Uptake and Kinetics of Transient Liquid Phase Bonding in Ni- based Superalloys," *Submitt. to Metall. Mater. Trans. A*, Pending, 2019.

[57] C. A. Tadgell, "Examining the Mechanisms and Kinetics of Transient Liquid Phase Bonding of Titanium Alloys Using Copper and Nickel Filler Metals," Dalhousie University, 2019.

[58] Y. Zhou, W. F. Gale, and T. H. North, "Modelling of transient liquid phase

bonding," *Int. Mater. Rev.*, vol. 40, no. 5, pp. 181–196, 1995.

[59] M. A. Arafin, M. Medraj, D. P. Turner, and P. Bocher, "Transient liquid phase bonding of Inconel 718 and Inconel 625 with BNi-2: Modeling and experimental investigations," *Mater. Sci. Eng. A*, vol. 447, no. 1–2, pp. 125–133, 2007.

[60] O. A. Ojo, N. L. Richards, and M. C. Chaturvedi, "Effect of gap size and process parameters on diffusion brazing of Inconel 738," *Sci. Technol. Weld. Join.*, vol. 9, no. 3, pp. 209–220, 2004.

[61] J. Crank, *The Mathematics of Diffusion*, Second. London: Oxford University Press, 1975.

[62] D. A. Porter, K. E. Easterling, and M. Y. Sherif, *Phase Transformations in Metals and Alloys*, 3rd Editio. Boca Raton, Fl: Taylor & Francis Group, 2016.

[63] N. Zhu, X. Xu, X. G. Lu, Y. He, J. Zhang, and H. Jiang, "Experimental and computational study of diffusion mobilities for fcc Ni–Cu–Mn alloys," *Calphad Comput. Coupling Phase Diagrams Thermochem.*, vol. 54, pp. 97–106, 2016.

[64] J. Wang, H. S. Liu, L. B. Liu, and Z. P. Jin, "Assessment of diffusion mobilities in FCC Cu-Ni alloys," *Calphad Comput. Coupling Phase Diagrams Thermochem.*, vol. 32, no. 1, pp. 94–100, 2008.

[65] W. Zhang, Y. Du, L. Zhang, H. Xu, S. Liu, and L. Chen, "Atomic mobility, diffusivity and diffusion growth simulation for fcc CuMnNi alloys," *Calphad Comput. Coupling Phase Diagrams Thermochem.*, vol. 35, no. 3, pp. 367–375, 2011.

[66] Thermocalc, "Diffusion Module (DICTRA)," *Thermo-Calc Software*, 2019. [Online]. Available: https://www.thermocalc.com/products-services/software/diffusion-module-(dictra)/. [Accessed: 17-Jun-2019].

[67] American Welding Society, "AWS C3.2M/C3.2: 2008 Standard Method for Evaluating the Strength of Brazed Joints." American Welding Society, p. 29, 2008.

[68] S. D. Nelson, S. Liu, S. Kottilingam, and J. C. Madeni, "Spreading and solidification behavior of nickel wide-gap brazes: The characterization of braze alloys containing boron and silicon for the repair of nickel-based superalloy turbine components," *Weld. World*, vol. 58, no. 4, pp. 593–600, 2014.

[69] Y. Flom, L. Wang, M. M. Powell, M. A. Soffa, and M. L. Rommel, "Evaluating

Margins of Safety in Brazed Joints," *Weld. J.*, no. 10, pp. 31–37, 2009.

[70] B. Riggs, A. Benatar, B. T. Alexandrov, and R. Xu, "Experimental Validation of Damage Zone Models for Lap - Shear Brazed Joints Using DIC," *Weld. J. WRS*, no. November, pp. 421-428s, 2017.

[71] Y. Flom and L. Wang, "Flaw Tolerance in Lap Shear Brazed Joints - Part 2," in *International Brazing and Soldering Conference*, 2003, pp. 1–9.

[72] Y. Flom and L. Wang, "Flaw Tolerance in Lap Shear Brazed Joints - Part 1," *Weld. J.*, no. January, pp. 32-38-S, 2004.

[73] N. Bredzs and F. M. Miller, "Use of the AWS Standard shear Test Method for Evaluating Brazing Parameters," *Weld. J.*, vol. 47, no. 11, pp. 481s-496s, 1968.

[74] E. Lugscheider, H. Reimann, and O. Knotek, "Calculation of Strength of Single-Lap Shear Specimen," in *Seventh International AWS Brazing Conference*, 1976, pp. 189–192.

[75] Commonwealth Oil, "EDM V(TM) Wire Corrosion Inhibitor." Commonwealth Oil, p. 2, 2015.

[76] V. 2 ASM International Handbook, "Properties and selection: Nonferrous alloys and special-purpose materials," *ASM Met. Handb.*, vol. 2, p. 1300, 1990.

Appendix A Calculated solidus and liquidus temperatures

Table A.1 – Melting range temperatures of major regions in Ni30/IN625 narrow gap braze joints. Solidus and liquidus temperature values calculated using single point equilibrium in Thermo-Calc software.

Region	Hold time at T_B (min)	T_{sol} (°C)	T_{liq} (°C)
S	0	1027.64	1059.00
	30	1057.82	1092.85
	80	1079.86	1116.78
M	0	1046.14	1077.00
	30	1073.31	1109.64
	80	1070.28	1106.59

Table A.2 – Melting range temperatures of major regions in Ni30/IN625 wide gap braze joints. Solidus and liquidus temperature values calculated using single point equilibrium in Thermo-Calc software.

Region	Hold time at T_B (min)	T_{sol} (°C)	T_{liq} (°C)
S	30	1015.33	1056.62
	240	1015.78	1052.19
	720	1033.84	1068.66
	1320	1052.81	1093.01
M	30	1048.21	1080.74
	240	1055.65	1089.33
	720	1078.95	1116.61
	1320	1080.90	1118.38

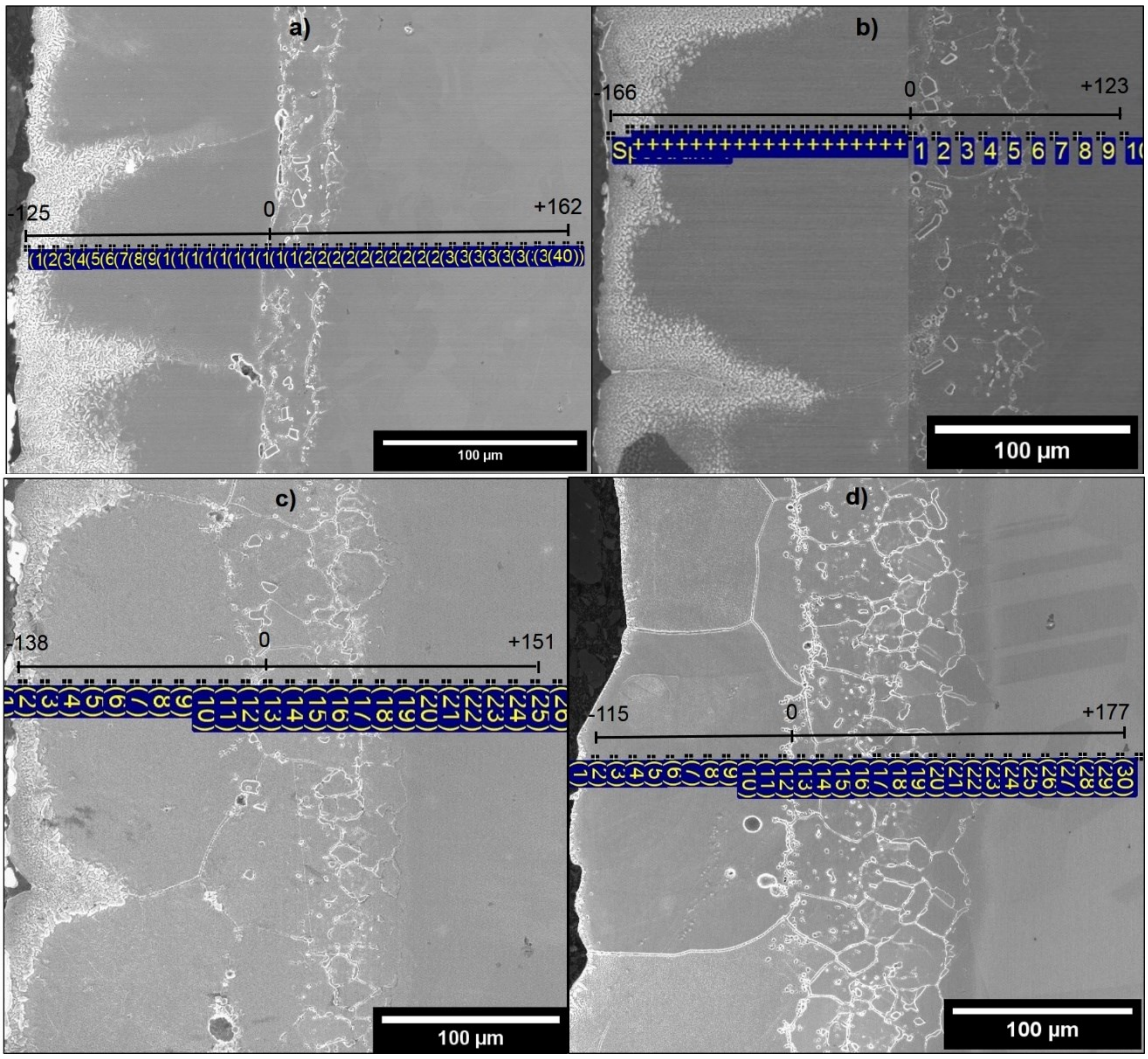

Figure A.1 – SEM micrographs of Ni30/IN625 HBJ samples held at 1050 °C for a) 30 min b) 240 min c)720 min d) 1320 min showing locations of EDS point scans. Micrographs correspond to EDS elemental composition graphs in Figure 5.23.

Appendix B Examination of O_2 content in tube furnace

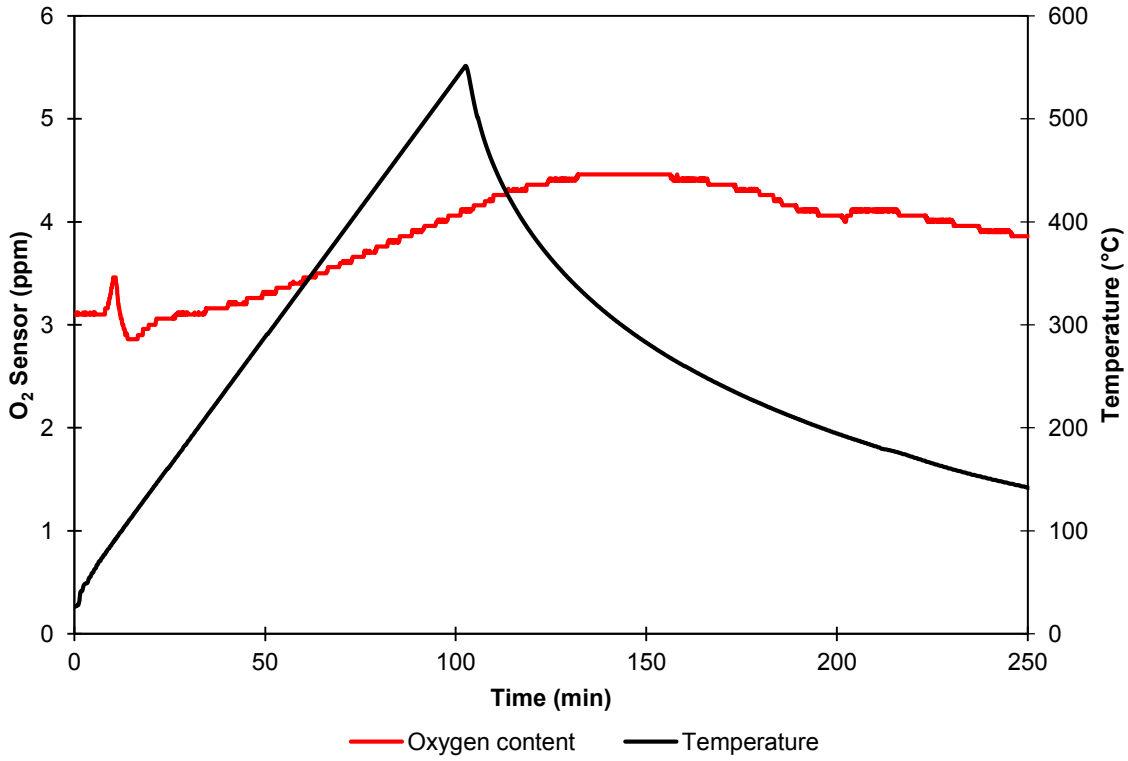

Figure B.1 – Measured O_2 content in Sentrotech high temperature brazing tube furnace.

Appendix C Dimensions of Single Lap Joint Test Specimens

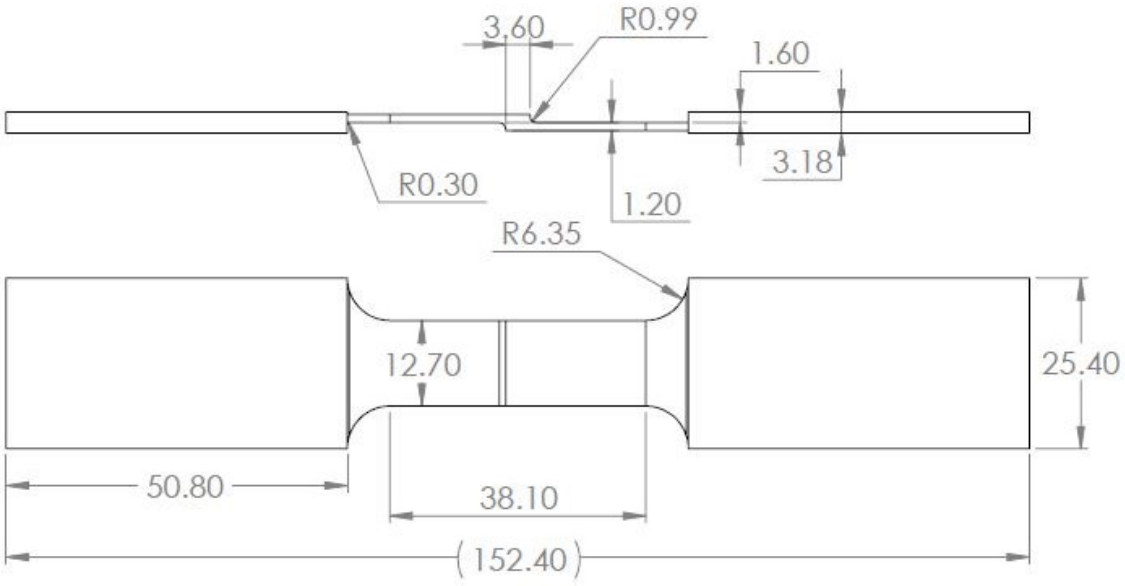

Figure C.1 – Dimensioned drawing of IN625 monolithic simulated single lap joint specimen. Specimen cut by wire EDM.

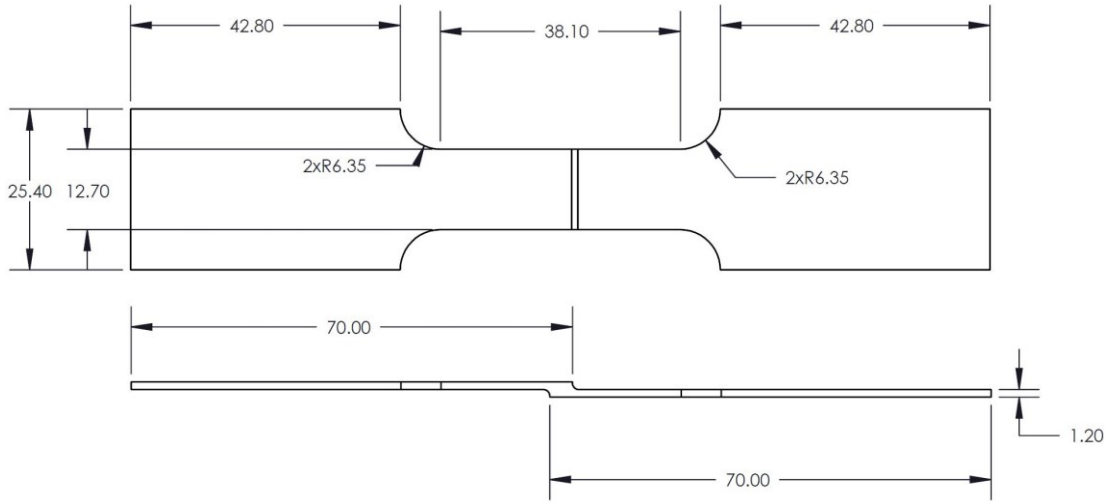

Figure C.2 - Dimensioned drawing of IN625 single lap joint specimen. Filler metal BNi-2 or Ni30. Specimen cut by wire EDM.

Table C.1 – Summary of dimensional changes in single lap shear test specimens for width (w) and thickness (t).

		e	d	c	b	a
Initial	w			12.70 ± 0.01		
	t	1.20 ± 0.03		2.48 ± 0.02	1.20 ± 0.03	
Ni30	w	-0.82 ± 0.04	-0.78 ± 0.02	-0.25 ± 0.04	-0.76 ± 0.04	-0.83 ± 0.04
	t	-0.12 ± 0.02	-0.13 ± 0.02	n/a	-0.14 ± 0.01	-0.12 ± 0.02
BNi-2	w	-0.60 ± 0.05	-0.59 ± 0.07	-0.08 ± 0.01	-0.56 ± 0.06	-0.62 ± 0.03
	t	-0.09 ± 0.00	-0.09 ± 0.01	-0.04 ± 0.01	-0.09 ± 0.01	-0.08 ± 0.01
IN625	w	-1.53 ± 0.38	-1.58 ± 0.75	-0.26 ± 0.05	-1.98 ± 0.54	-1.91 ± 0.33
	t	-0.20 ± 0.04	-0.18 ± 0.09	-0.08 ± 0.03	-0.25 ± 0.04	-0.23 ± 0.01